PRIMARY AFFERENT ENCODING OF WHISKER SELF-MOTION AND ACTIVE TOUCH

By

Kyle Severson

A dissertation submitted to Johns Hopkins University in conformity with the requirements for the degree of Doctor of Philosophy

Baltimore, Maryland

October 2018

Abstract

Purpose: This dissertation aims to (1) define the mechanics that underlie primary afferent encoding of active touch and self-motion during whisking and (2) characterize how much information is encoded by cutaneous mechanoreceptors in the face during whisking.

Methods: Simultaneous high-speed videography and electrophysiological recordings from primary afferents allowed us to identify the mechanical quantities that correlate with activity encoded during active sensation in mice. Optogenetic tagging enabled genetic labeling of Merkel afferents.

Results: Merkel afferents were sensitive to touch and self-motion. During active touch, Merkel afferent spiking arose from whisker bending moment and its rate of change. During whisking, afferent responses depended on external stresses related to whisker inertia and internal stresses related to activation of specific muscles. Whisker afferents encoded the most information about whisking kinematics when compared to other mechanoreceptors in the face.

Conclusions: Touch and proprioceptive signals are multiplexed by primary afferents in the whisker system via mechanical sensitivity. Several cutaneous sources, including Merkel afferents in whisker follicles, send significant self-motion information to the brain that could be used for proprioception.

Keywords: somatosensation, touch, proprioception, mechanics, viscoelastic, vibrissa, whisking, trigeminal, Merkel cells

Advisor: Daniel O'Connor

Readers: Daniel O'Connor and Xinzhong Dong

Committee members: Xinzhong Dong, Jeremiah Cohen, and Jeremy Nathans

Preface

For my family, Brian, Nancy, Philip, and Quinn, who supported me through this journey,

and for Steve Hsiao, who introduced me to the world of touch.

I would like to acknowledge:

the contribution of Dan O'Connor, whose mentorship, support, and hard work

made the conception and completion of this project possible,

the contribution of Ling Bai and David Ginty, whose genetic tools were invaluable,

the contribution of Duo (Many) Xu, whose computational skill, work ethic, and creativity

helped propel this work,

the support of labmates Hongdian Yang, Sam Kwon, Genki Minamisawa,

Erik Finkel, and Yi-Ting Chang,

the hard work of undergraduates Meg Van de Loo and Andrew Russo,

and the contribution of graduate students Emily Han and Isis Wyche

Table of Contents

List of Tables

List of Figures

Introduction

Imagine you are sitting in front of a computer, eyes fixed on the words and pictures on the screen. Fingers tap the keys of the qwerty keyboard. The rapid typing pauses briefly as you reach over, wrap your fingers around the smooth, curved handle of the coffee mug on the table and bring the glazed ceramic to your lips, all without moving your eyes away from the monitor. Precisely executing these seemingly mundane motor actions requires complex integration of tactile and movement information. In fact, interactions with the world often involve active sensation, whereby our sensory organs are poised purposefully to extract information from the world around us. Our eyes dart and focus to capture visual information, our heads crane and turn to hear sounds, and our hands enclose and palpate to sense the physical properties of objects. At any time, we sense only a tiny fraction of the world, as if we are gazing through a pinhole. Even so, we do not sense the outside world directly. Rather, what we sense is the sensory epithelium's interaction with the outside world. Orientation, movement, and efferent control of the sensory organs drastically affect the nature of sensation. Thus, to understand how sensory processing occurs, it is of critical importance to reveal the peripheral mechanisms underlying sensation in active contexts.

Despite the pervasiveness of active sensation, our understanding of the peripheral mechanisms underlying active sensing is limited. The physical and neural bases at the peripheral encoding stage have been studied in active contexts using somatosensation as a model system. Somatosensation is divided into several submodalities, including mechanosensation, thermosensation, pruriception (itch), and nociception (pain) (Lai et al., 2016). Mechanosensation can be further divided into two types of sensation. Touch is the sense of mechanical stresses exerted on the body, and proprioception is the sense of mechanical stresses exerted by the body.

Touch and proprioception begin with activation of mechanoreceptors. Discriminative touch is mediated by low threshold mechanoreceptors (LTMRs). LTMRs are divided into several subtypes, defined by the morphology of the mechanosensory endings. The unique morphology and mechanical properties of each subtype are thought to relate to specialized functions, such as shape or texture coding (Abraira and Ginty, 2013). While efference copy of motor commands is known to be important (for review, see: Crapse and Sommer, 2008), the nervous system also relies on proprioceptive feedback from the periphery for motor learning. Proprioceptive feedback is thought to originate primarily from muscle spindles embedded in muscles and Golgi tendon organs (GTOs) embedded in the tendons near joints. However, recent studies have identified another important source of feedback about movement. Cutaneous LTMRs sensitive to touch and movement have the potential to play a pivotal role in both touch and proprioception. This is the basis of a phenomenon called cutaneous proprioception, whereby mechanoreceptors in the skin encode aspects of body kinematics. In this introduction, I will review observations regarding cutaneous proprioception in human limbs, orofacial regions of multiple species, and whisker follicles of rodents.

Out on a limb: discovery of cutaneous proprioceptors in the hand and leg

Proprioceptive signals from cutaneous afferents innervating the limbs have been reported by several studies. Information from these afferents may be complimentary to proprioceptive signals from muscle receptors in the limbs. The activity of cutaneous proprioceptors was first recorded by Hulliger et al. (1979) in the glabrous (non-hairy) skin of the human hand. The authors discovered glabrous skin afferents, recorded using microneurography in the medial nerve, responded as subjects produced ramp-and-hold and oscillatory finger movements. LTMRs in the glabrous skin are classically divided into four main types: slowly adapting type I Merkel's disks (SA-I), slowly adapting type II Ruffini endings (SA-II), rapidly adapting type I Meissner's corpuscles (RA-I), and Pacinian corpuscles (PC) (Abraira and Ginty, 2013). A subset of units from each of the four types responded during voluntary movements. Units tended to fire during the dynamic phases of the movement, although a fraction of SA-II units responded weakly during the static phase of ramp-and-hold movements. Firing rates during voluntary movement were similar to rates evoked by stimulation with von Frey filaments at five times mechanical threshold. These findings suggest that movement-related responses of glabrous skin afferents are perceptible and could be functionally relevant for proprioception and motor control.

Edin and Abbs (1991) revisited cutaneous proprioception in the human hand during voluntary finger movements, but they analyzed recordings from afferents innervating the dorsal hairy skin of the hand. Less in known about the identity of mechanoreceptors in the hairy skin compared to the glabrous skin in humans. Afferents were classified based on classical physiological properties, such as mechanical adaptation and inter-spike interval distribution. The authors found a large number of SA-I and RA-I afferents that responded during finger movements. Qualitatively, responses were consistent with deformations of their receptive fields induced by the finger and hand movements. SA-I afferents tended to respond directionally, preferring to fire during the flexion rather than the extension phase of movements. RA-I afferents responded bidirectionally during movement. Edin and Abbs found the locations of RA-I receptive fields were concentrated near joints, many of which were responsive during hand movement. Because the dorsal skin is less involved in haptic exploration compared to the glabrous skin, it may be specialized to sense skin stretch during movement. Movement responses have been observed not only in cutaneous afferents innervating the hands but also in those innervating the legs, suggesting that cutaneous proprioception may be a ubiquitous process across the body.

Edin (2001) later pioneered microneurography recordings from afferents innervating the human thigh during imposed knee movements. Again, it was found that a subset of cutaneous afferents was responsive during joint movements, even when the receptive field was distal to the knee joint. SA units signaled static position and dynamic movements with high fidelity. These findings suggest that cutaneous proprioception is present in the legs and may be involved in motor control from large joints. Aimonetti et al. (2007) collected recordings from afferents innervating skin on the ankle region. Whereas the finger and knee flexion studied previously were restricted to one-dimensional movements, ankle movements in this study were two-dimensional. Many cutaneous afferents responded during ankle movements, including a majority of SA-II and RA-II afferents with large receptive fields. Units with receptive fields on the anterior side of the lower leg responded preferentially during plantar flexion, as the toes point downward. Conversely, units with receptive fields on the lateral side of the lower leg responded preferentially during eversion, as the outside of the foot moves upward. Thus, the population vectors from afferents on the anterior and lateral regions represented the direction of movement. Responses of cutaneous afferents mirrored those in underlying muscle receptors (Bergenheim et al., 2000), suggesting that proprioception could involve co-processing of movement-related feedback from both cutaneous and muscle sources.

Studies of cutaneous proprioceptors in the hand and leg suggest these afferents can provide to the central nervous system a signal that conveys information about movement. Whether the brain actually uses this information remains an open question. One psychophysical study by Collins et al. (2005) addressed this question via a clever perturbation. Vibration of muscles and tendons has long been known to cause illusory sensations of position and movement (Goodwin et al., 1972). In this experiment, subjects were instructed to match the perceived angle of the finger, elbow, or knee joint as the experimenter applied vibration, skin stretch, or combined vibration and skin stretch to the contralateral joint. Addition of skin stretch significantly affected the perception of joint angle at the elbow, knee, and proximal interphalangeal finger joints compared to vibration alone. Skin stretch alone produced a smaller perceived change in joint angle than vibration alone. These results suggest that in the limbs, stimulation of cutaneous and muscle afferents contribute to perception of joint angle.

Feeling your face: evidence of cutaneous proprioception in facial regions

The presence of cutaneous proprioceptors in facial regions would add significant evidence for this theory due to the curious fact that muscle spindles and GTOs are absent from most facial muscles (Goodmurphy and Ovalle, 1999; Stal et al., 1987, 1990). Thus, for many facial motions, cutaneous LTMRs are the only known sources of afferent feedback. This section reviews behavioral and electrophysiological evidence from facial regions that supports the notion that cutaneous proprioception provides important feedback for motor control.

Abbs and Gracco (1984) assessed the role of cutaneous proprioception in human subjects during speech. During randomly interleaved trials, the authors added a load to the lower lip and observed corrective lower lip movements. Interestingly, both lower and upper lip muscles were co-activated following the loading perturbation, suggesting parallel sensorimotor mechanisms. Compensatory responses occurred at latencies ranging from 22-75 ms, longer than the expected latency for brainstem reflexes. Ito and Ostry (2010) performed a similar perturbation during speech. Lip protrusion increased following brief stretch of the cheek skin. Motor learning persisted, as lip movement remained changed in trials without perturbation. Again, compensatory responses were observed in muscle activity at moderate latencies of approximately 50 ms following skin stretch. These findings suggest that ascending input from cutaneous afferents are used by the nervous system for moment-to-moment corrections during speech.

Speech requires complex motor coordination to produce the correct mouth movements which depends on afferent feedback. Cutaneous afferents could be sensitive to aspects of mouth opening, oral closure, build up and release of air pressure, and associated strain patterns in the face during speech. Johansson et al. (1988) recorded from afferents in the infraorbital nerve using microneurography in humans during speech and other oral movements. A handful of recordings were conducted as subjects produced different syllables. Remarkably, units with receptive fields on or near the lips and on other parts of the face responded in preparation for and during production of syllabic speech (see also: Trulsson and Johansson, 2002). This study provides the first evidence of cutaneous proprioceptor activity in the human face and suggests that these afferents can encode information about facial kinematics during speech.

While human studies of facial proprioception primarily focused on speech, studies in other mammals must necessarily focus on other facial behaviors. Appenteng et al. (1982) reported activity from cutaneous afferents in the mandibular branch of the trigeminal ganglion in rabbit during chewing movements. Afferent receptive field and jaw movement direction selectivity properties were manually classified and related to firing patterns during active jaw movements. A majority of hair follicle afferents were active during passive jaw displacements and during chewing movements. Units on hair follicles were not selective to any particular direction of jaw movement but were linearly correlated with the magnitude of velocity in any direction. Skin afferents were much less sensitive to imposed jaw movements, and spiking correlations with velocity were sublinear. However, skin afferents close to the corner of the mouth tended to fire during the jaw closing phase. These results provide confirmation that cutaneous afferents exist in other species and can encode facial movements. Cutaneous afferents are not the sole source of proprioceptive information during jaw movements, as muscle spindles innervate the masseter muscle (Moore et al., 2015) and encode jaw kinematics (Masuda et al., 1997; Morimoto et al., 1989). However, similar activity has been found in afferents innervating hairy skin that are active during another stereotyped facial movement. Whisking is an excellent model for studying cutaneous proprioception during facial movement, as muscle spindles are absent from the muscles that drive whisking (Moore et al., 2015).

In a recent study, Severson et al. (2018) conducted a comprehensive comparative analysis of facial mechanoreceptor activity in the mouse during whisking behavior (see Chapter 3). The authors compared mutual information between whisking kinematic variables and mechanoreceptor spiking from afferents with either whisker, facial hairy skin, non-whisker vibrissae, or masseter muscle proprioceptors. Afferents on whiskers, whisker pad hairy skin, and the supraorbital vibrissa encoded high amounts of information about whisk phase. Movements of facial skin and vibrissa outside of the whisker pad were phase-locked to and strongly correlated with whisker motion. The authors also reported the presence of mechanoreceptors with receptive fields on hairy skin that were sensitive to facial movement during whisking. Similar to the mandibular hair follicle afferents reported in rabbit, self-motion responsive hairy skin afferents in mouse had receptive fields on fur, adapted rapidly, lacked direction selectivity, and responded in a velocity-dependent manner. These hairy skin afferents could encode whisking kinematics independent of active touch. This study establishes that in the context of all facial mechanoreceptors, whisker afferents are a robust source of self-motion information.

Whiskers make sense: lessons learned from the whisker system

We next turn our attention to the whisker system, which has been influential for our understanding of active sensation. The whisker system offers several advantages for studying cutaneous proprioception. First, the system is easily accessible. Barrel cortex is positioned on the dorsal surface of the brain and its somatotopic organization can be easily mapped. Primary afferents are located in the trigeminal ganglion at the base of cranium and are accessible for in vivo electrophysiological recordings. Second, whisker kinematics and mechanics are relatively easy to model and quantify. Third, the mouse offers a suite of genetic tools that allow identification of cell types and dissection of these circuits. Finally, cutaneous proprioception could be especially important in whisking rodents because conventional proprioceptors are absent from the whisking muscles (Arvidsson and Rice, 1991; Moore et al., 2015). Thus, the whisker system can only receive self-motion information from efference copy and cutaneous afferents. This section reviews findings pertaining to cutaneous proprioception leveraged from the whisker system.

Curtis and Kleinfeld (2009) demonstrated that phase is an important coordinate system for representing self-motion and touch in barrel cortex. Several studies provide strong evidence that self-motion activity in barrel cortex indeed arises from cutaneous sources. Fee et al. (1997) recorded single unit activity in barrel cortex as rats whisked in air. They found clear phase- and amplitude-tuned activity. The authors performed a critical experiment, in which whisking on the contralateral pad was blocked by lidocaine injection in the facial nerve. Phase-tuned activity disappeared following the nerve block, providing strong evidence that the oscillatory activity in barrel cortex is encoded via ascending sensory sources rather than via corollary discharge signals from motor areas. Poulet and Petersen, (2008) recorded neurons in layer 2/3 of barrel cortex using in vivo whole cell patching. Membrane voltage was strongly modulated during whisking, resembling the whisker position. However, after abolishing sensory input from the whiskers by infraorbital nerve cut, this whisking modulation disappeared. Hill et al. (2011) tested the effect of infraorbital nerve cut on encoding of whisking kinematics in motor cortex. Surprisingly, they found qualitatively similar encoding of slow (amplitude and midpoint) and fast (phase) variables in motor cortex in animals with intact or cut infraorbital nerve. Slow variables were represented by a large fraction of neurons, whereas phase was weakly encoded by a small fraction of neurons. Unlike in barrel cortex, the representation of whisking kinematics was not as affected by blockage of afferent feedback in motor cortex. Together, these studies provide consistent evidence that cutaneous afferent input is incorporated in generating the representation of whisking kinematics in barrel cortex. How do cutaneous afferents encode whisking kinematics?

The whisker follicle is densely innervated by several types of mechanoreceptors (Ebara et al., 2002). Recent studies have conducted recordings from these mechanosensitive whisker afferents during active whisker motion. Szwed et al. (2003) recorded responses of neurons in the trigeminal ganglion using an artificial whisking paradigm in rats. In this setup, the rat is anesthetized, and whisking is generated by electrical stimulation of the facial nerve. They discovered cells that were sensitive to touch only, whisking and touch, or whisking only. Whisking responses occurred at various phases, and the population tiled phase space. A large majority of units preferred protraction phases, which could be an artifact of electrical stimulation of the protractor muscles. The authors propose that this phase information could be used to compute the horizontal location of an object. Using a novel closed-loop artificial whisking setup, Wallach et al. (2016) demonstrate that phase coding is amplitude- and frequency-invariant and is "computed" from a combination of kinematic variables. While findings from artificial whisking have advanced our understanding of whisking-related activity, mechanics in awake rodents could be quite different.

Several studies have recorded whisker afferent responses in awake rodents. Khatri et al. (2009) recorded whisker afferent activity in awake, head-fixed rats during "whisking in air." In a subset of afferents, responses were amplitude- and velocity-dependent. Their findings suggested that whisker afferent responses in awake rodents were phase-locked, rather than time-locked to the onset of the whisk cycle. What mechanics underlie this phase sensitivity during whisking in air? Quist et al. (2014) modeled forces and moments at the base of the whisker during contact and whisking in the absence of contact. They proposed that the major source of mechanical stress at the whisker base arises from inertial moment, which is correlated with angular acceleration. Campagner et al. (2016) recorded whisker afferent responses in actively whisking head-fixed mice. They found whisking responses were often correlated with angular acceleration, suggesting that whisker afferents could indeed be sensitive to inertial stresses.

In mouse, genetic tools have been developed to allow identification and functional characterization of mechanoreceptor cell types (for review, see: Takatoh et al., 2018). Severson et al. (2017) utilized a mouse line (Bai et al., 2015) to specifically label Merkel afferents (See Chapters 1 and 2). Merkel afferents were slowly adapting, and a subset was sensitive to both active touch and whisking in air. Similar to previous findings, whisking in air responses were often correlated with angular acceleration. Inertial stress is proportional to the product of the object's angular acceleration and moment of inertia. In a causal test of whether inertial stresses underlie whisking responses, Severson et al. recorded whisking responses before and after manipulating moment of inertia via whisker cutting. For many afferents, firing rates during whisking decreased as the whisker was progressively cut. These findings provide additional support to a mechanical framework for modeling active whisker sensation. Furthermore, moment of inertia manipulations could provide a powerful tool to assess the contribution of cutaneous proprioceptors to the whisker system. With any luck, findings leveraged from this model system will generalize to other facets of somatosensation, including sensation of orofacial regions and the limbs.

Chapter 1: Mechanical Encoding of Active Touch[1]

The stimulus sensitivities of multiple types of low-threshold mechanoreceptors have been described in several mammalian systems, including in the glabrous skin of the primate fingertip and mouse hairy skin (Abraira and Ginty, 2013; Johnson et al., 2000). In the fingertip and hairy skin, decades of work have characterized responses of slowly adapting (SA) type 1 afferents, which correspond to large-diameter nerve fibers that associate with Merkel cells in the skin (Iggo and Muir, 1969; Woodbury and Koerber, 2007). Recent work has shown that mechanical activation of Piezo channels drives spiking in both Merkel cells and their afferents (Ikeda et al., 2014; Maksimovic et al., 2014; Ranade et al., 2014; Woo et al., 2014), and that Merkel cells synaptically excite their afferents (Chang et al., 2016; Maksimovic et al., 2014).

Merkel cell-associated afferents ("Merkel afferents") are thought to play a crucial role in perception of spatial form due to their small, densely packed receptive fields and their high-fidelity responses to the surface properties of touched objects (Johnson and Hsiao, 1992; Johnson et al., 2000). However, Merkel afferent activity has been studied almost entirely with passively applied stimuli. Touch is an active sense and typically occurs in the context of self-generated motions, where mechanics that govern interactions with the world can be quite different. The role of Merkel afferents in active touch is unknown.

While humans explore the tactile environment largely through hand movements, mice seek out tactile information by sweeping their whiskers through the space surrounding their heads. The

---

[1] Sections of this chapter are adapted from Severson et al., 2017.

rodent whisker system is a powerful model for sensory-motor integration (Diamond and Arabzadeh, 2013; Diamond et al., 2008; Hill et al., 2011; Maravall and Diamond, 2014), due to well-mapped neural circuitry, ease of controlling sensory input, and genetic accessibility. Remarkably, despite these advantages, no recordings have been made from genetically identified whisker primary afferents during active touch.

Here, we developed a preparation to simultaneously record from, and quantify mechanical input to, identified Merkel and unidentified slowly adapting ("SA") and rapidly adapting ("RA") afferents during active touch. We define that mechanical sensitivity to moment and its rate of change allows our sample of Merkel and other afferents to encode the properties of actively touched objects.

Recording from Merkel and unidentified afferents during whisking and active touch

We obtained electrophysiological recordings from Merkel afferents that innervate the whisker follicle (Ebara et al., 2002; Rice et al., 1986). An optogenetic tagging approach allowed us to record spikes from single genetically identified Merkel afferents during behavior (Figures 1.1 and 1.2). Mice whisked freely in air and against a pole presented at multiple locations as they ran on a treadmill (Figure 1.1A,B), generating mechanical signals at the whisker base (Figure 1.3). We collected an initial dataset (n = 33 afferents) comprised of identified Merkel afferents (n = 14), as well as unidentified SA (n = 12, likely including Merkel) and RA (n = 7) afferents.

Whisker afferents are located in the trigeminal ganglion (TG) and have receptive fields containing a single whisker (Zucker and Welker, 1969). High-speed (500 Hz) video of this whisker allowed us to estimate mechanical variables expected to cause spiking (Figure 1.3), by integrating post hoc measurements of whisker shape into models of whiskers as tapered beams (Birdwell et al., 2007; Pammer et al., 2013). We aligned spike times from single afferents with mechanical time series including the angular position (*θ*), velocity (*ω*), acceleration (*a*) and jerk (ζ, the rate of change of *a*) of the whisker, and the magnitudes of the two forces (F_{ax}, axial force pushing the whisker into the follicle, and F_{lat}, lateral force pushing the whisker along the face), and one bending moment (M_0, acting to bend the whisker at its base) resulting from whisker-object interactions in the plane of video imaging (Figure 1.3A,B; Methods). We also quantified rates of change for the two contact forces (F'_{ax} and F'_{lat}) and bending moment (M'_0).

For our initial dataset (of 33 afferents), we obtained 54,647,500 frames of high-speed video with simultaneous single neuron recordings for analysis, corresponding to 823 minutes total for identified Merkel afferents, and 999 minutes for unidentified afferents. We assigned each video frame into one of three behavioral categories: (1) not whisking and not in contact with the pole; (2) whisking in air with no contact; and (3) whisking against the pole. To avoid ambiguous periods in which a nearly motionless whisker swayed in and out of light contact with the pole, we excluded from further analysis periods of contact without whisking.

During non-whisking periods, most Merkel and unidentified afferents spiked at low rates (Figure 1.3C; baseline rate 0.0 ± 0.2 Hz, median ± interquartile range (IQR) , n = 33, including 14 Merkels, 12 SA and 7 RA). All afferents responded with increased spike rates during touch (whisker-pole contact; 48.0 ± 96.3 Hz, median ± IQR, n = 33). During whisking in air, most afferents responded with increased spike rates (denoted "WT" afferents to indicate both whisking and touch responsiveness, following terminology of (Szwed et al., 2003; Yu et al., 2006); Figure 1.3C and Table 1). For a subset of WT afferents, spike rates during whisking in air were especially pronounced (Figure 1.3C, asterisks; 19.1 ± 58.2 Hz, median ± IQR; 13 of 33 afferents total, including 5 Merkel, 7 SA and 1 RA; we denote this subset of WT afferents as “WT*”; See Glossary in Appendix).

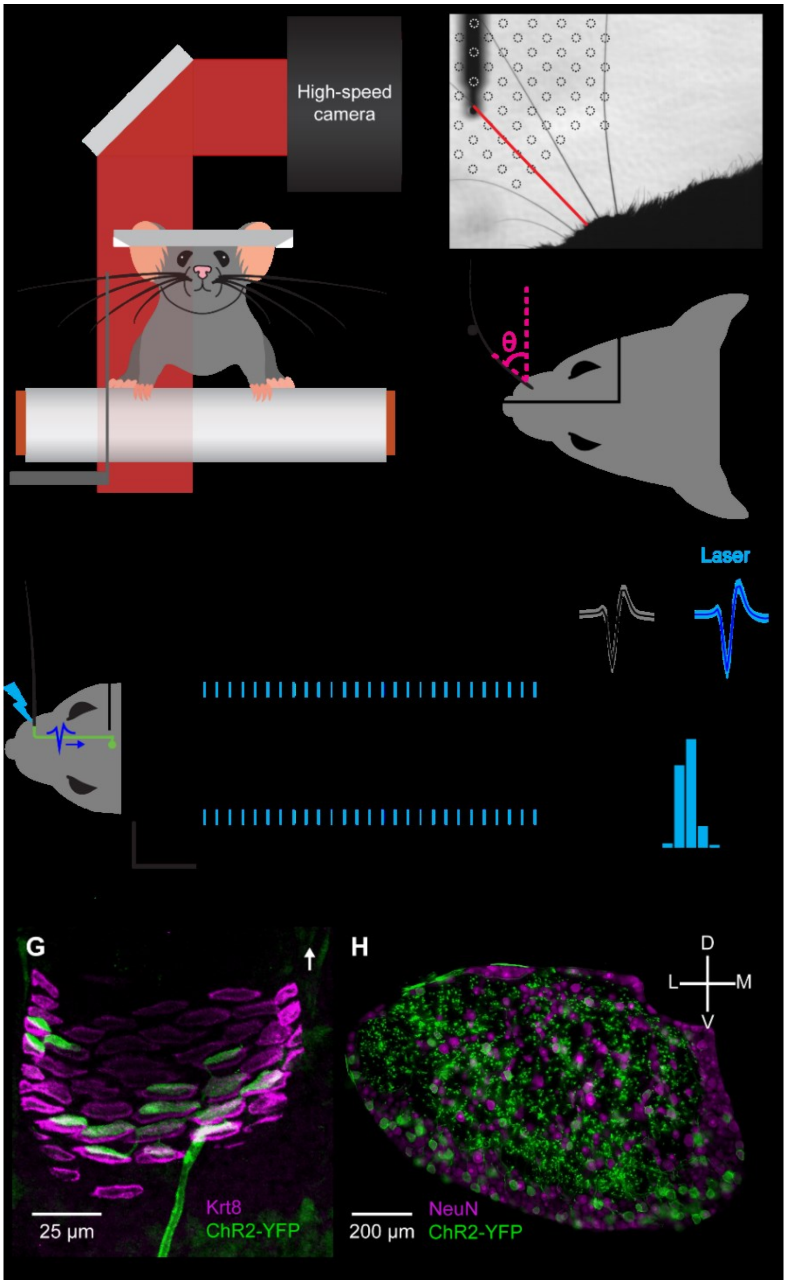

Figure 1.1 Recording spikes from Merkel afferents during active touch.

(**A**) Schematic of experimental setup. A mouse whisked against a small vertical pole while head-fixed and running on a treadmill. High-speed video (500 Hz) of whiskers were obtained at the same time as electrophysiological recordings from primary afferents in the trigeminal ganglion. (**B**) Image from high-speed video overlaid with example grid showing the set of pole locations used during one afferent recording. The shadow from part of the mouse face and the pole in one location (and its holder) are evident. One row of whiskers was left intact. A whisker in contact with the pole is highlighted in red. Whisker position (θ) was measured as angular displacement from the medial-lateral axis. (**C**) Schematic of in vivo identification of Merkel-associated afferents by optogenetic tagging. The whisker pad was illuminated with blue light (bolt) while a recording was made from a whisker-responsive neuron in the trigeminal ganglion. Action potentials triggered by photostimulation (blue waveform) of the peripheral axon propagated to the cell body where they were recorded. (**D**) Example electrophysiology traces showing spikes of a primary afferent responsive to stimulation of the B3 whisker (top) and to photostimulation targeted to the B3 whisker follicle (middle), but not to photostimulation of the nearby C1 whisker follicle (bottom). Vertical blue ticks: 2 ms light pulse. (**E**) Spike waveforms (mean ± SD) in response to touch (black) and light (blue) were nearly identical (shading: SD). (**F**) Histogram of latencies from light onset to time of spike (peak or trough) recorded in TG, for neuron shown in (D). Spikes occurred with short latency (mean: 3.6 ms) and low jitter (SD: 0.3 ms). (**G**) Projection through a confocal z-stack of a single whisker follicle (region of the ring sinus) showing a single channelrhodopsin-2 (ChR2)-expressing afferent (green), associating with Merkel cells (magenta). Merkel cells are labeled by keratin 8 (Krt8, TROMA-I) staining. White arrow: direction of skin surface. (**H**) Coronal section through the trigeminal ganglion of a $TrkC^{CreER}$;$Rosa^{Ai32}$ mouse showing ChR2 expression (green) in both cell bodies and processes. Cell bodies are labeled by NeuN staining (magenta).

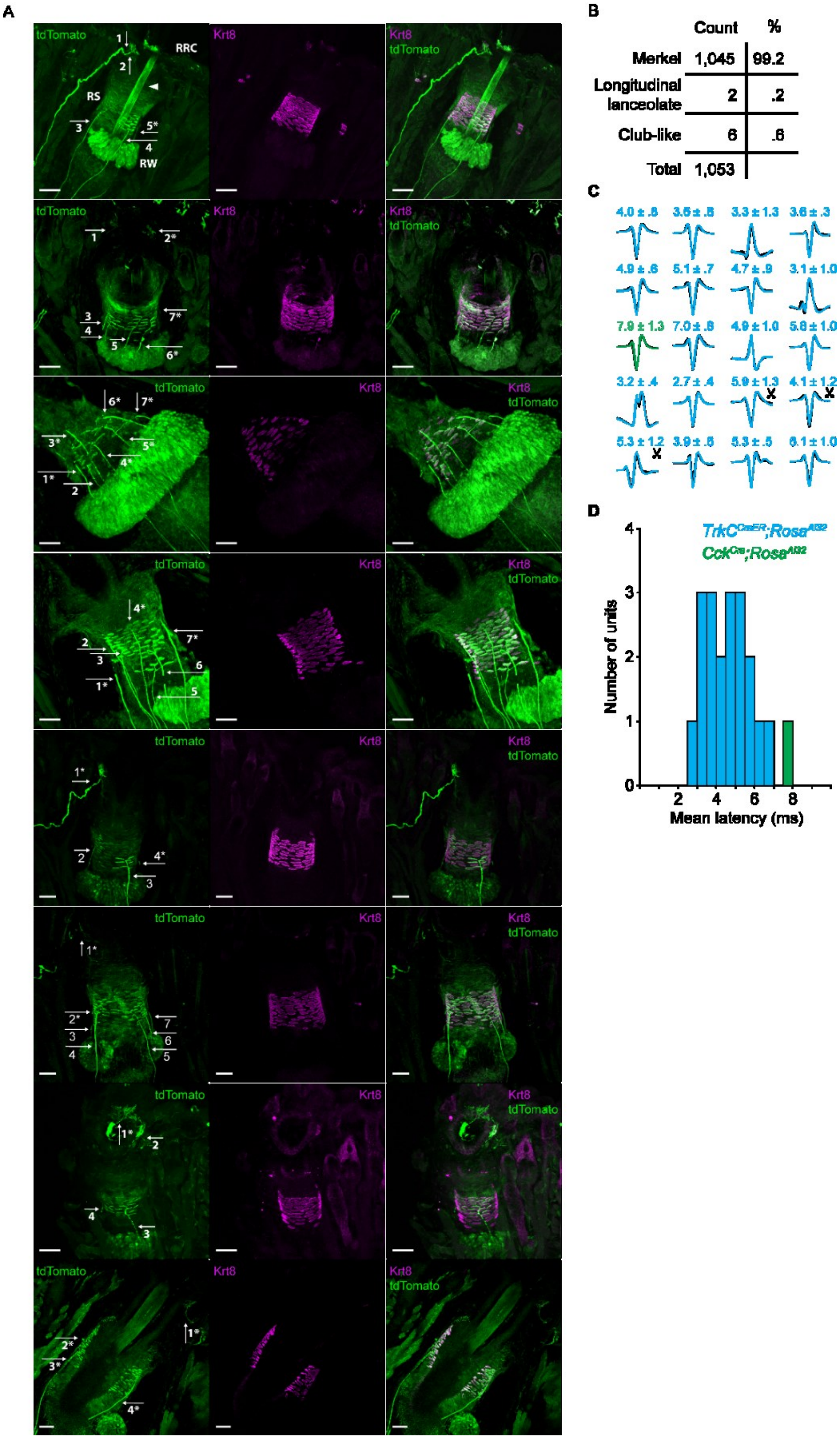

Figure 1.2 Specific labeling of Merkel afferents in TrkC$^{\mathrm{CreER}}$ mouse.

(**A**) Confocal stack projections of whisker follicles from two *TrkC^{CreER};Rosa^{Ai9}* mice (Mouse 1: top 4 rows; Mouse 2, bottom 4 rows). Green channel (left column, tdTomato) shows labeled afferent processes selected for classification of ending type (arrows). Endings that could not be identified by their morphology as a known whisker follicle ending type were "unclassified" (indicated by asterisks). In top left image, anatomical regions of the whisker are labeled: whisker shaft (arrowhead), ringwulst (RW), ring sinus (RS), and rete ridge collar (RRC). Merkel cells (middle column, magenta) were stained with anti-cytokeratin 8 (Krt8). Merged images (right column) were used to determine association of afferent endings with Merkel cells. All images are oriented with skin surface at the top. (**B**) Merkel cell-associated afferents are specifically labeled in whisker follicles of *TrkC*^{CreER};*Rosa*^{Ai9} mice (counts included all tdTomato^{+} afferents in 3 whisker pads from 3 mice). Of classified Merkel afferents, the vast majority (994 of 1,045) were located in the Merkel dense region rather than the rete ridge collar. (**C**) Mean spike waveforms evoked by light (blue: *TrKC*^{CreER};*Rosa*^{Ai32} mice; green: *Cck*^{Cre};*Rosa*^{Ai32}) shown superimposed on those evoked by mechanical stimulation (black). Spike latency is indicated above each waveform (mean ± SD from time of light onset to spike peak or trough, in ms). All identified Merkel afferents are shown (n = 19 from *TrKC*^{CreER};*Rosa*^{Ai32} in blue, and n = 1 from *Cck*^{Cre};*Rosa*^{Ai32}in green). Three putative WT* afferents obtained after whisker cutting are indicated with scissors icons. To help characterize our optogenetic tagging method, also shown are 3 afferents (bottom row, right-most) for which lack of rostral-caudal direction selectivity or whisker tracking errors prevented inclusion in other figures or analyses. Spike waveforms presumably vary in part to electrode position with respect to the cell body and axon of these pseudounipolar neurons. (**D**) Histogram of mean spike latencies for the neurons in (C).

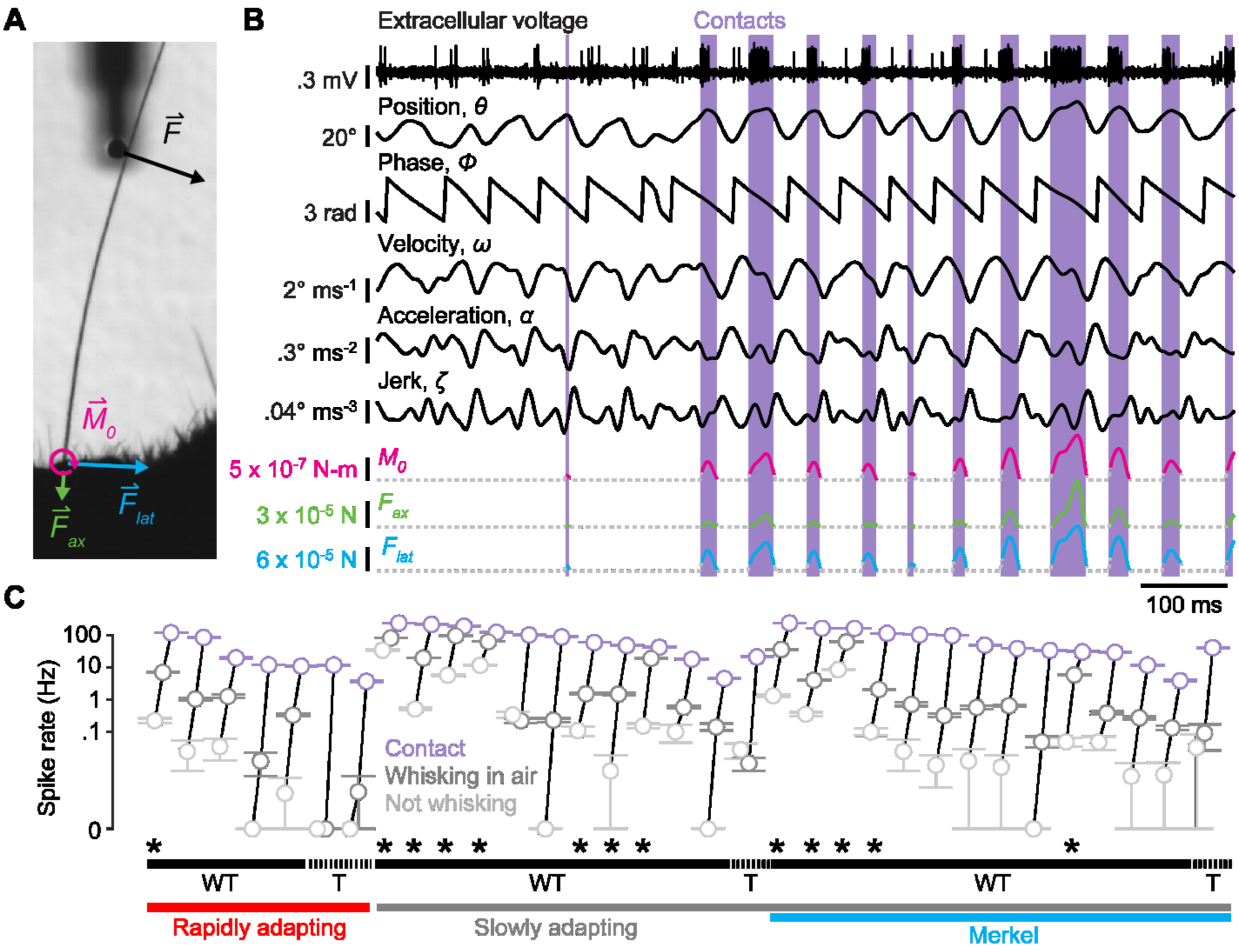

Figure 1.3 Merkel and unidentified afferents respond to both active touch and self-motion.

(**A**) Zoomed region of a high-speed video frame showing a whisker in contact with the pole. Whisker-pole contact force ($\vec{F}$) can be decomposed into the force components acting along the axis of the whisker ($\overrightarrow{F_{ax}}$) and lateral to the face ($\overrightarrow{F_{lat}}$). Magnitudes of these forces and of the bending moment ($\overrightarrow{M_0}$) induced by $\vec{F}$ were estimated for each video frame. (**B**) Example time series for a Merkel afferent. One second of electrophysiological recording (top trace) is shown with mechanical variables estimated from the high-speed video, including whisker angular position (θ), phase of θ within the whisk cycle (Φ), whisker angular velocity (ω), whisker angular acceleration (α), whisker angular jerk (ζ), and magnitude of contact-induced moment (M_0), axial force (F_{ax}) and lateral force (F_{lat}). Periods of whisker-pole contact are indicated by lavender shading. (**C**) Mean spike rates of neurons during periods when the mouse was not whisking (light gray symbols), during whisking in free air (dark gray), and during whisker-pole contact (lavender). Error bars indicate 95% bootstrap confidence intervals of the means. Data points for each neuron are connected by black lines. Neurons are sorted along the horizontal axis by rapidly adapting (lower red bar) or slowly adapting (lower black bar) properties, positive Merkel afferent identification (lower blue bar), and sensitivity to touch (T, upper dashed bars) or to both whisking and touch (WT, upper solid bars). A subset of afferents especially sensitive to whisking in air (referred to as "WT*" in the text) are indicated with asterisks.

Active touch is encoded via sensitivity to moment and its rate of change

To investigate coding during touch, we analyzed periods of whisker-pole contact. Merkel and SA afferents responded to contact by spiking in a slowly adapting and dramatically direction-selective manner, responding far more strongly to contacts in either the protraction or retraction direction (Figure 1.4A). Mice whisked freely against a pole presented at different locations, producing highly variable spike rates that reflected both whisking behavior and the tuning properties of each afferent (Figure 1.4B). What mechanics underlie spiking during active touch?

We fitted statistical models for each afferent to predict spike rate as a function of mechanical variables, based on single (2 ms) video frames during touch (Generalized Additive Models, GAMs; Methods). We quantified model performance using the Pearson correlation between time series of predicted and actual spike rate, after smoothing with a Gaussian kernel (σ = 4 ms). A "full" model (GAM fitted to M_0, F_{ax}, F_{lat}, M_0', F_{ax}', F_{lat}', θ, ω, a and ζ) allowed excellent recapitulation of the mean spike rate for touches at different pole locations (Figure 1.4B,C) and strongly predicted ongoing spike rate (r = 0.71 ± 0.16, mean ± SD, n = 33; Figure 1.4D). Comparison of statistical models revealed that individual Merkel and unidentified afferents responded to several mechanical variables (Figure 1.5A-D). Models fitted to moment or its rate of change alone explained spiking relatively poorly (r =

0.45 ± 0.19 and 0.42 ± 0.21, respectively; mean ± SD, n = 33; Figure 1.4D). However, M_0 and M_0' together explained spiking (r = 0.63 ± 0.20, n = 33) better than any other pair of variables, and better than a more complex model fitted to M_0, F_{ax}, and F_{lat} (r = 0.48 ± 0.19, n = 33; Figures 1.4D and 1.5C). Thus, although afferents responded to multiple mechanical variables, spiking during touch was parsimoniously accounted for by M_0 and M_0'.

To visualize the sensitivity of each afferent to M_0 and M_0', we constructed joint tuning surfaces (Figures 1.4E,F and 1.5E). These surfaces show the mean spike rate evoked by combinations of M_0 and M_0'. Individual touches corresponded to stereotypic trajectories through two of the four quadrants (Figure 1.4E,F; protraction touches: $M_0 > 0$; retraction touches: $M_0 < 0$). Tuning surfaces revealed consistent motifs across afferents (Figures 1.4H,I and 1.5E).

Moment at the base of the whisker and its rate of change were critical drivers of Merkel and SA afferent spiking during touch. Whisker bending moment causes strain in the follicle (Bagdasarian et al., 2013; Whiteley et al., 2015), which can presumably lead to Piezo channel activation and subsequent spiking. Why is rate of change of moment critical? The whisker is coupled to mechanically activated channels via viscoelastic tissues (Fraser et al., 2006; Mitchinson et al., 2004). Stress in viscoelastic materials depends on both strain and its rate of change. We therefore hypothesized that sensitivity to both M_0 and M_0' arose from tissue viscoelasticity (cf. Fraser et al., 2006; Williams et al., 2010).

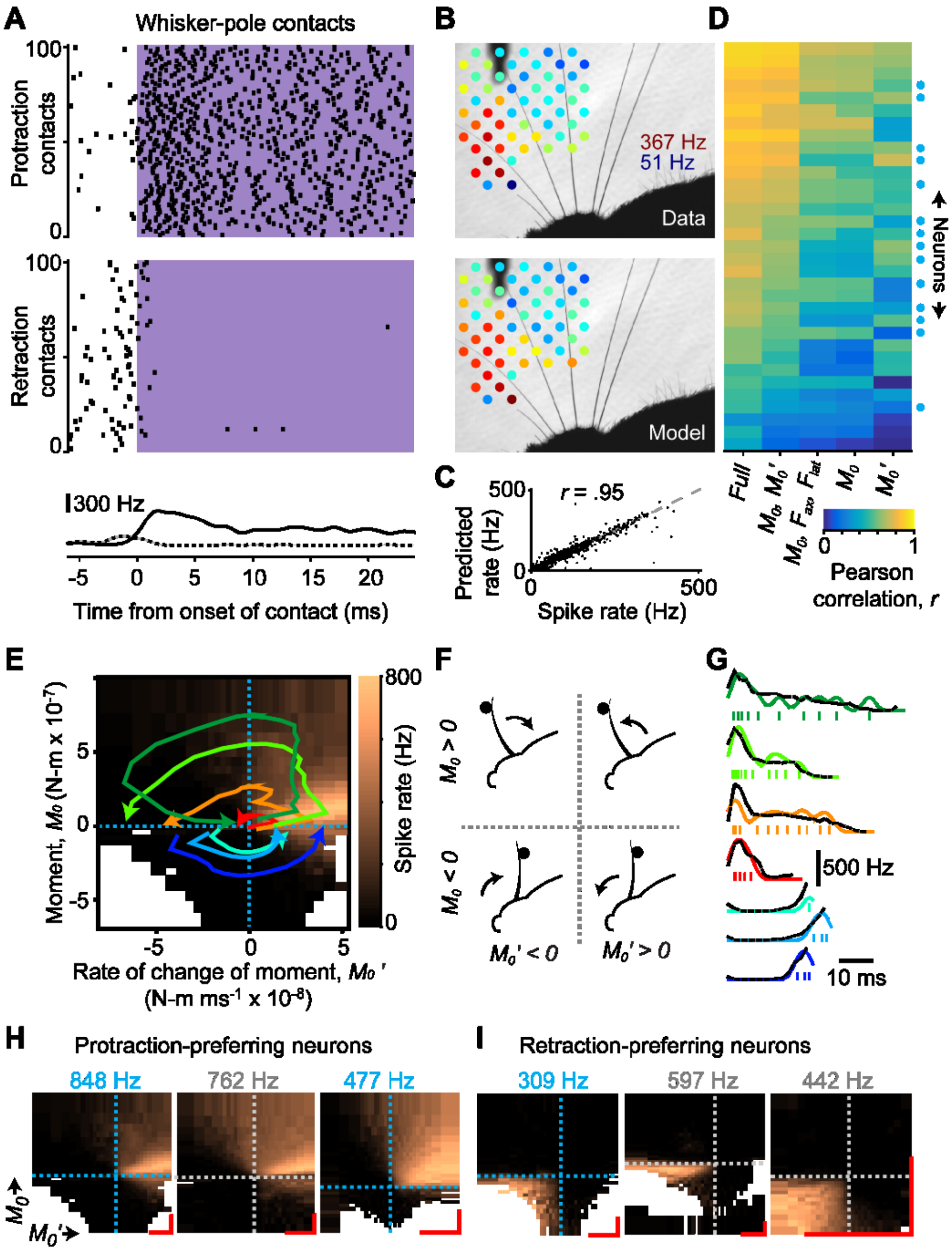

Figure 1.4 Active touch encoding via sensitivity to bending moment and its rate of change.

(**A**) Example rasters showing spiking of a Merkel afferent for 100 randomly selected protraction (top raster) and retraction (bottom raster) contacts. Lavender shading indicates contact (2 ms resolution). Shown at bottom are mean spike rates aligned to contact onset for all protraction (solid, ± SEM, n = 4,392 total) and retraction (dashed ± SEM; n = 1,556 total) contacts. Spike rate differences prior to contact in the two rasters are due to differences in tuning to protraction and retraction self-motion. (**B**) Mean spike rate (indicated by colors) during contact at each pole location (top) for an example SA afferent, and predicted spike rate from the "full" GAM statistical model (Methods) fitted to predict instantaneous spikes from this neuron (bottom). The color scale for both panels is identical and ranges from 51 to 367 Hz. (**C**) Actual versus predicted mean spike rates during contact, pooled across neurons and pole locations (data for each neuron as in [B]). (**D**) Heatmap showing the Pearson correlation coefficient, *r*, between recorded spikes (smoothed by Gaussian kernel with $\sigma = 4$ ms) and predicted spike rates from GAM models (columns) fitted for each neuron (rows; blue circles: Merkel afferents) based on different combinations of mechanical variables. (**E**) Tuning surface for example Merkel afferent (same as in [A]) showing mean spike rate (color scale) binned by moment (M_0) and its rate of change (M_0'). Trajectories (colored curves) for example contacts are plotted on top of the surface. Each contact begins near the origin and proceeds counter-clockwise across either the top (for protraction) or bottom (for retraction) half of the tuning surface. Dashed lines indicate axis origins. Bins with fewer than 25 observations are white. (**F**) Schematic depicting the four quadrants of the $M_0 - M_0'$ tuning surface shown in (E). The whisker can be moving in the protraction or retraction direction and be in contact with a pole either in front of or behind the whisker. (**G**) Spike times shown individually (ticks) and smoothed (colored curves, Gaussian kernel with $\sigma = 2$ ms) for the example trajectories in (E), overlaid with spike rate "read off" from the tuning surface (black dashed traces). (**H**) Example $M_0 – M_0'$ tuning surfaces for three neurons that preferred protraction contacts (leftmost neuron from [E]). (**I**) Same as (H) but for three neurons that preferred retraction touches. (H-I) Dashed lines indicate the origin of each axis and are colored by afferent type (blue: Merkel; white: SA). The color scale for each surface ranges from 0 Hz to a maximum spike rate indicated above the surface (blue text: Merkel). Scale bars (red) indicate 2×10^{-7} N-m and 2×10^{-8} N-m ms^{-1} for M_0 and M_0', respectively. White bins as in (E).

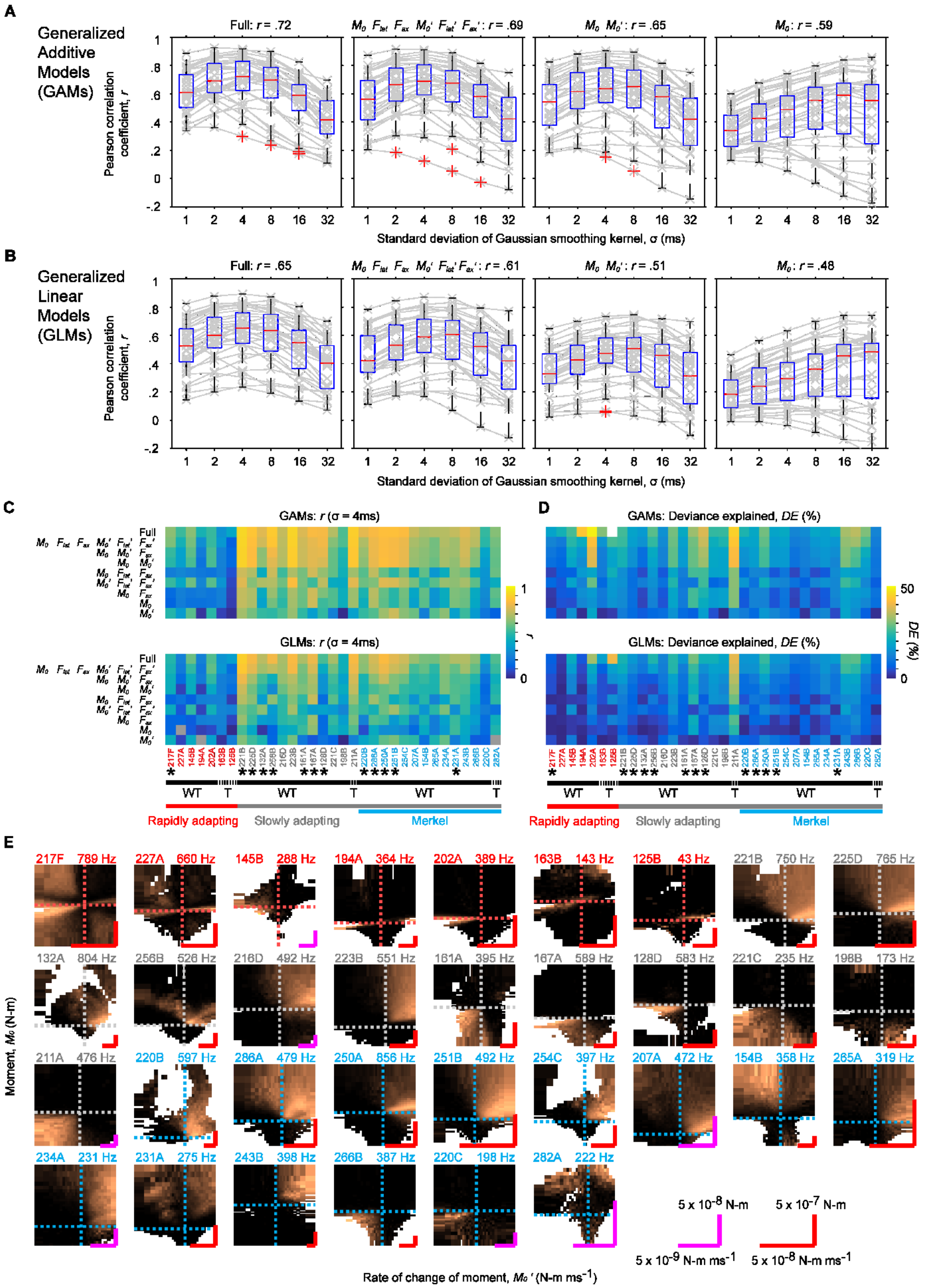

Figure 1.5 Tuning to contact forces and bending moment.

(**A**) Systematic evaluation of the performance of Generalized Additive Models (GAMs) fitted by different combinations of variables (shown in title of each plot) during contact periods for each neuron (gray lines; n = 33 afferents in each plot). The r value given in the title is the median Pearson correlation coefficient across neurons for the level of smoothing yielding highest performance. "Full" models include all dynamic variables (M_0, F_{ax}, F_{lat}) and their rates of change (M_0', F_{ax}', F_{lat}'), plus four kinematic variables (θ, ω, a, ζ). The performance of each model (gray crosses) was quantified as the Pearson correlation coefficient (r; y-axis) between predicted spike rate and the recorded spikes smoothed by Gaussian kernels with a range of sizes (in standard deviation, σ; x-axis). Box plots depict distribution of r values across neurons within each smoothing condition (medians: red lines; 25th and 75th percentiles: lower and upper box boundaries; outliers marked by red plus symbols; MATLAB "boxplot"). Most models achieved best performance with $\sigma = 4$ ms. (**B**) Evaluation of Generalized Linear Models (GLMs) for the same data showing similar relationships between model performance and the smoothing parameter. Conventions as in (A). (**C**) Heatmaps showing r values ($\sigma = 4$ ms) for GAMs (top) and GLMs (bottom) based on different combinations of mechanical variables (along rows) for each neuron (columns). Similar to Figure 1.4D but including additional models. Afferents are sorted and labeled along the x-axis identically to Figure 1.3C and are also listed by name to allow identification in Table 1. Conventions as in Figure 1.3C. GAMs outperform GLMs overall. (**D**) Same as in (C) but with performance quantified using deviance explained (%), which does not depend on smoothing. (**E**) Tuning surfaces for moment and its rate of change, for all touch recordings (n = 33). Dashed lines indicate the origin of each axis and are colored by afferent type (blue: Merkel; gray: SA; red: RA). The color scale for each surface ranges from 0 Hz to a maximum spike rate indicated by text above the surface (in Hz). Viscoelastic model was fitted to all Merkel and SA afferents except for 128D (for which the fitting algorithm failed). Red scale bars indicate 5×10^{-7} N-m and 5×10^{-8} N-m ms^{-1} for M_0 and M_0', respectively. Magenta scale bars indicate 5 x 10^{-8} N-m and 5 x 10^{-9} N-m ms^{-1} for M_0 and M_0', respectively. Bins with fewer than 25 observations are white.

Active touch responses are predicted by a simple mechanical model

We fitted a simple empirical model of viscoelastic coupling between moment at the whisker base and stress in the follicle (Figure 1.6A). Our goal was to test whether such coupling could explain the responses of Merkel and SA afferents. In the model, moment was converted into strain inside the follicle according to sigmoidal functions. Strain caused elastic and viscous stresses (modeled by a spring and damper, respectively) that were then summed, rectified and mapped linearly to spike rate up to a maximum of 1,000 Hz (Figure 1.6A,B; Methods). The model postulates that firing rate of Merkel and SA afferents is determined by instantaneous strain and its rate of change and does not depend on either stimulus or spiking history.

Remarkably, this mechanical model predicted spike rates at levels comparable to GAM statistical models (Figure 1.6C) and reproduced tuning surfaces (Figure 1.6D). The excellent fit between data and model suggests that filtering of contact stresses by tissue viscoelasticity underlies spike rate adaptation, and thus plays a central role in determining the activity of Merkel and SA afferents (Williams et al., 2010).

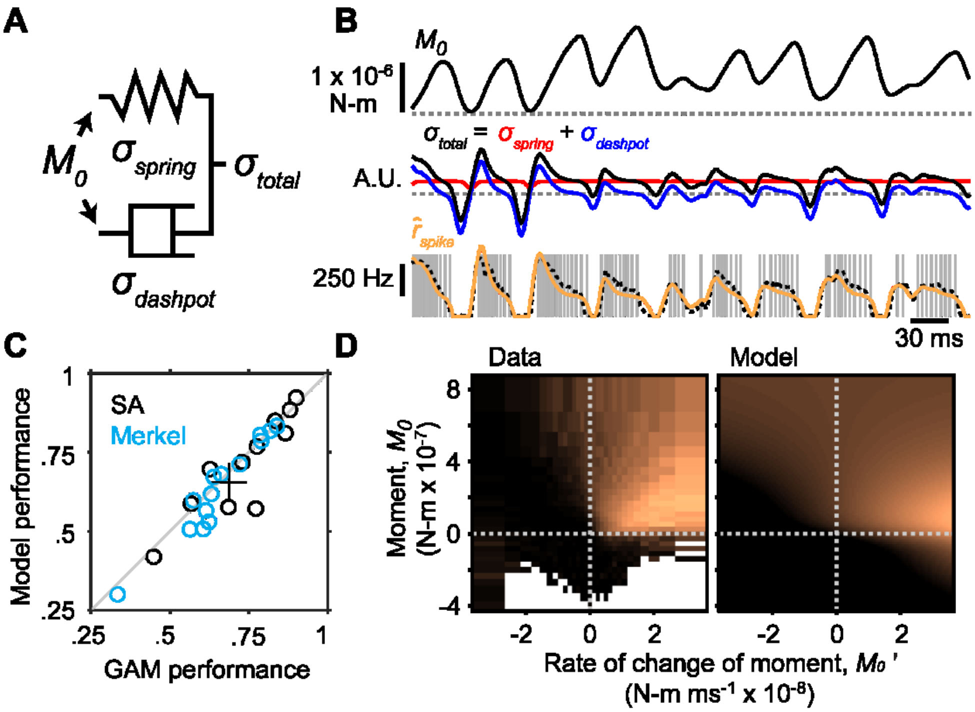

Figure 1.6 A simple mechanical model predicts responses to active touch.

(**A**) Schematic of the model. Moment at the base of the whisker causes strain on a spring and dashpot arranged in parallel. Variables representing elastic (σ_{spring}) and viscous ($\sigma_{dashpot}$) stresses are summed (σ_{total}) and scaled (to a maximum of 1,000 Hz) to yield spike rate. (**B**) Example model dynamics for a single touch. Top, Example trace of moment (M_0) during a protraction contact for a recording from a Merkel afferent (dashed gray line: $M_0 = 0$). Middle, Elastic (red) and viscous (blue) stress variables and their sum (black; dashed gray: $\sigma = 0$). Bottom, Individual spike times (gray ticks) aligned to the M_0 trace. Spike rate predicted from the viscoelastic model (orange) matched that predicted from the M_0–M_0' tuning surface (dashed black; left surface shown in [D]). This example represents a challenging trajectory containing wide ranges of M_0 and M_0'. (**C**) Viscoelastic model performance was similar to that of GAM statistical models based on M_0 and M_0'. Performance of each model was quantified by the Pearson correlation coefficient, *r*, between model-predicted spike rates and recorded spike rates (smoothed by Gaussian kernel with $\sigma = 4$ ms). Plot symbols show individual Merkel (blue circles, n =

14) and SA (black circles, n = 11; one SA excluded because model fitting failed) afferents and the mean ± 95% bootstrap confidence interval (black lines). (**D**) Tuning surfaces for real data (left) and simulated from the model (right). Color scale ranges from 0 to 500 Hz. Conventions as in Figure 1.4E.

Discussion

Our results quantify the responses of genetically identified Merkel and unidentified afferents during active touch. Merkel and SA afferents responded not only to touch, but also to self-motion. Self-motion responses encoded the position of the whisker within the current whisk cycle (whisk phase). This phase coding arose from a combination of external stresses related to the whisker's inertia, and internal stresses that reflected the activity of specific whisking muscles.

Recordings from TG of anesthetized rodents have shown that spike trains from whisker afferents can encode passively applied stimuli with exquisite fidelity and temporal precision (Bale et al., 2015; Jones et al., 2004). Passive stimulation studies have defined major features of the neural response to whisker deflection kinematics, such as deflection velocity and amplitude (Shoykhet et al., 2000; Stuttgen et al., 2008; Zucker and Welker, 1969). Studies using artificial whisking have shown that TG afferents respond to multiple features of whisker motion and touch (Szwed et al., 2003; Szwed et al., 2006; Wallach et al., 2016).

During active touch, Merkel and SA afferents responded to multiple mechanical variables. However, responses were concisely accounted for by two variables: bending moment (M_0) and its rate of change (M_0'). Our finding that Merkel and SA afferents signal rate of change of moment (M_0') is intriguing because, together with whisker velocity (ω), this quantity can be used to compute the radial distance to a touched object and even the three-dimensional shape of complex objects (Birdwell et al., 2007; Luo et al., 2009; Solomon and Hartmann, 2011).

A simple mechanical model largely explained Merkel and SA afferent spiking. Modeling the whisker-follicle-afferent complex in greater detail (Lottem and Azouz, 2011; Mitchinson et al., 2004) will constitute important future work, but our bare-bones model already gives precise prediction of touch responses and insight into the function of Merkel afferents. Spike rate adaptation in our model arose from tissue viscoelasticity. Spike rate adaptation due to tissue viscoelasticity differs from other forms, such as ion channel inactivation, with different implications for sensory processing. Ion channel inactivation causes stimulus sensitivity to decrease over time and recover slowly. In the case of viscoelastic adaptation, spikes reflect instantaneous stress with no loss of sensitivity.

All Merkel and SA afferents we tested showed sensitivity to bending moment and its rate of change (Figures 1.4 and 1.5). However, they differed in other mechanical sensitivities during touch (Figures 1.4 and 1.5). Afferents overall and even identified Merkel afferents, for instance, showed different levels of responsiveness to whisking in air (Figure 1.3C). The whisker follicle contains several morphologically distinct mechanoreceptor types, including two populations of Merkel endings (one at the rete ridge collar, near the skin surface, the other located deeper in the region of the ring sinus; (Ebara et al., 2002; Rice et al., 1986). Individual Merkel, RA (longitudinal lanceolate) (Sakurai et al., 2013) and club-like (Tonomura et al., 2015) afferents project to multiple trigeminal nuclei in the brainstem, and individual brainstem neurons receive convergent input from both RA and Merkel afferents (Sakurai et al., 2013). Yet these brainstem nuclei originate distinct pathways for somatosensory signals ascending to cortex, with markedly different response properties (reviewed in: Bosman et al., 2011; Diamond et al., 2008; Feldmeyer et al., 2013; Kleinfeld and Deschenes, 2011). An intriguing speculation is that functional subtypes of Merkel afferents might project to brainstem targets in a manner more specific than the overall population. In general a major outstanding question is how diverse afferent responses during active touch (Leiser and Moxon, 2007; Szwed et al., 2003) relate to mechanoreceptor types and their brainstem projections. Our approach, which combines quantification of sensory input during active touch with simultaneous recordings from genetically defined afferents, promises major progress on how different aspects of touch and proprioception are integrated by neural circuits.

Here, we investigated the responses of Merkel and unidentified afferents to whisking and active touch during behavior. Despite the popularity of the whisker system, only a very small number of studies have recorded from whisker afferents in behaving animals (Bush et al., 2016; Campagner et al., 2016; Khatri et al., 2009; Leiser and Moxon, 2007; Pais-Vieira et al., 2013; Yang et al., 2016). Only two of these studies measured the whisker bending necessary to estimate the forces and moments that drive spiking (Bush et al., 2016; Campagner et al., 2016). Our work supports these two studies, which both used statistical models to correlate the spiking of unidentified whisker afferents with mechanical variables estimated from high-speed video and extends them in multiple ways. First, our results are based in significant part on recordings from identified Merkel afferents (17 of 53 recordings). Second, while our results support the notion that afferent spiking is closely associated with whisker bending moment (Bush et al., 2016; Campagner et al., 2016), we show that, in addition to bending moment (M_0), its rate of change (M_0') must also be considered in order to explain spiking during touch. Third, we offer a simple mechanical model that explains these sensitivities in terms of contact forces and tissue viscoelasticity. Fourth, our data suggest that individual afferents respond to multiple mechanical variables beyond M_0 and M_0', of possible use for location coding (Pammer et al., 2013; Solomon and Hartmann, 2011).

Materials and methods

All procedures were in accordance with protocols approved by the Johns Hopkins University Animal Care and Use Committee.

Mice. *Rosa*$^{Ai32/Ai32}$ (Jackson Labs: 012569; *B6;129S-Gt(ROSA)26Sor*$^{tm32(CAG\text{-}COP4*H134R/EYFP)Hze}$*/J*) mice (Madisen et al., 2012) on a mixed background were mated with *TrkC*$^{CreER/+}$ mice (Bai et al., 2015). Date of conception was marked by observation of vaginal plug. To induce CreER–based recombination at embryonic dates E11.5-E13.5, pregnant females were dosed by oral gavage with 1.5 mg tamoxifen (Sigma) dissolved in sunflower oil (Sigma). Pups were delivered by Caesarian section at E19-E19.5 and reared by a CD1 foster mother (Charles River). For histological quantification of afferent labeling, *TrkC*$^{CreER/+}$ mice were crossed with *Rosa*$^{Ai9/Ai9}$ (Jackson Labs: 007909; *B6.Cg-Gt(ROSA)26Sor*$^{tm9(CAG\text{-}tdTomato)Hze}$*/J*) mice (Madisen et al., 2010) instead of *Rosa*$^{Ai32/Ai32}$ mice but otherwise generated identically. *Cck*$^{Cre/Cre}$ (Jackson Labs: 019021; *Cck*$^{tm1.1(cre)Zjh}$) mice (Taniguchi et al., 2011) were crossed with *Rosa*$^{Ai32/Ai32}$ mice. During behavior and recording experiments, mice were housed singly in a vivarium with reverse light-dark cycle (12 hours each phase). Behavior experiments were conducted during the dark (active) cycle. The sex and line of each mouse used for recordings is detailed in Table S1.

Surgery. Adult mice (6-18 weeks old) were implanted with titanium headposts (Yang et al., 2016). Prior to electrophysiological recordings, two small openings (0.5 mm anterior-posterior, 2 mm medial-lateral) in the skull were made centered at 0.0 and 1.0 mm anterior and 1.5 mm lateral to Bregma. Dura were left intact. Craniotomies were covered acutely with gelatin sponge (VetSpon) or chronically with silicone elastomer (Kwik-Cast, WPI) under a layer of dental acrylic (Jet Repair Acrylic).

Behavioral training and apparatus. Mice received 1 ml/day of water for ≥ 7 days prior to training. Mice were head-fixed and placed on a custom linear treadmill to promote whisking, because mice whisk as they run. Running was encouraged by providing water rewards following voluntary bouts of running. Water was delivered via a custom "lickport" under control of Bcontrol software (C. Brody, Princeton University). On training days (2-10 days total), mice were weighed before and after each training session to determine water consumed. If mice consumed < 1 ml, additional water was given to achieve 1 ml total.

A 0.500 mm diameter class ZZ gage pin (Vermont Gage) was oriented vertically and placed in range of the whiskers. The top of the pole was elevated above the remaining whiskers but remained within the depth of high-speed video focus. The X-Y position of the pole was controlled via two stepper motors and translation stages (O'Connor et al., 2010).

Electrophysiology. The awake mouse was head-fixed and allowed to run on the linear treadmill. The craniotomy was exposed and covered with PBS. A single tungsten recording electrode (2 MΩ nominal, Parylene coated; WPI) was lowered ~5.5 mm until it reached the trigeminal ganglion. Activity was monitored by audio monitor (A-M Systems). The tissue was allowed to relax at least 10 min to stabilize recordings. An identical reference electrode was lowered to a similar depth. The differential electrophysiological signal between recording and reference electrodes was amplified 10,000x, bandpass filtered between 300 Hz and 3,000 Hz (DAM80, WPI) and acquired at 20 kHz using Ephus (Suter et al., 2010) or WaveSurfer (http://wavesurfer.janelia.org). Data were acquired in 5 s "trials" synchronized with high-speed video. A micromanipulator (Sutter Instruments) advanced the recording electrode until a well-isolated unit responsive to manual whisker stimulation was encountered. The unit's receptive field, response type (RA or SA), and direction selectivity were manually classified. All whiskers except the row containing the whisker-of-interest (WOI) were trimmed short with microdissection scissors. The pole was moved to regular locations spaced within range of the WOI. The mouse was coaxed to run by small manual movements of the treadmill belt. While running mice whisked against the stationary pole. Immediately subsequent to recording, under light isoflurane the WOI was plucked with forceps for post hoc measurements of whisker geometry. After recording sessions, the craniotomy was covered with silicone elastomer and a thin layer of dental acrylic. Spike waveforms were obtained by thresholding high-pass filtered (500 Hz) traces and clustered using MClust-4.1 or MClust-4.4 (AD Redish et al.).

Optogenetic identification of Merkel afferents. Our tamoxifen dosing conditions in *TrkC*$^{CreER/+}$ mice result in labeling of SA1-Merkel afferents and proprioceptors (Bai et al., 2015). We used an intersectional strategy in which we capitalized on the lack of spindle-type proprioceptors in the whisker pad (Moore et al., 2015), and the single whisker receptive fields of TG neurons (Zucker and Welker, 1969), in order to avoid recording from proprioceptors. Specifically, afferents that were both light responsive and had clear responses to manual stimulation of a single whisker were considered to be "Merkel" afferents. Neurons were tested for light sensitivity by manually directing laser illumination (473 nm; UltraLasers, DHOM-M-473-200) to a whisker pad location centered on the follicle corresponding to the neuron's whisker receptive field (~100 mW out of a 200 μm, 0.39 NA fiber; fiber was hand-held but positioned ~2-3 mm from the skin). Light pulses were triggered and acquired simultaneously with electrophysiology traces by Ephus. High-speed video was simultaneously recorded and inspected post hoc to eliminate the possibility of movement-related activity. Spikes from optogenetic stimulation trials were clustered together with spikes from all other (non-stimulation) trials. Because TG neurons are not known to synaptically excite one another, "indirect" excitation can occur only through a loop involving sensory-motor loops and mechanical excitation. Thus, with powerful light excitation in a subset of *TrkC*^{CreER};*Rosa*^{Ai32} mice we observed a light-evoked whisker movement ("twitch") visible on high-speed video at latencies as short ~25 ms. However, we accepted only neurons that spiked at short latency (< 8 ms; 4.9 ± 1.3 ms; mean ± SD) and with low jitter (SD of first-spike latency: 0.91 ± 0.29 ms; Figure 1.2C,D) following onset of a brief light pulses (< 10 ms; typically 2-4 ms) delivered infrequently (0.4-10 Hz). Many but not all accepted neurons followed 10 Hz trains (not shown); however, our hand-held optical fiber did not permit quantitative analysis of spike reliability. Inspection of high-speed video showed that our light-identified neurons responded even when no twitch was evoked (not shown). In searching for light-responsive neurons, we directed the light not only to the follicle of interest, but also to distant parts of the whisker pad (> 1 whisker away; expected to evoke the same twitches) and confirmed specificity (Figure 1.1). We found that we could evoke spiking (not shown) by directing light to a region caudal to the whisker pad shown, where afferent fibers come together into the infraorbital nerve (Dorfl, 1985), indicating that afferents could be excited by illumination of their processes outside the follicle. We did not rely on stimulation of this caudal location while searching for light-activated units, because it evoked strong whisker twitches due, presumably, to synchronous excitation of many afferents.

An alternative approach to exciting Merkel cell-associated primary afferents is to excite the afferents synaptically via ChR2 excitation of Merkel cells themselves (Maksimovic et al., 2014). *The* Cck^{Cre} line labels Merkel cells (Maksimovic et al., 2014), but also other tissue in the whisker pad including muscle cells. We could trigger clear muscle contractions at multiple locations on the body by local light stimulation in $Cck^{Cre};Rosa^{Ai32}$ mice (not shown). Thus, in practice we found it difficult to obtain spikes with sufficiently short latencies as to be unambiguously evoked by light stimulation per se rather than mechanically via ChR2-based muscle excitation. We therefore focused on the $TrkC^{CreER};Rosa^{Ai32}$ mice, but did include one light-identified neuron from a $Cck^{Cre};Rosa^{Ai32}$ mouse that met our criteria (7.9 ± 1.3 ms latency to spike; mean ± SD).

High-speed videography. Video frames (640 pixels x 480 pixels, 32 μm/pixel) were acquired at 500 Hz using a PhotonFocus DR1-D1312-200-G2-8 camera (90 μs exposure time) and Streampix 5 software (Norpix). Light from a 940 nm LED (Roithner Laser) was passed through a condenser lens (Thorlabs) and directed into a 0.25X telecentric lens (Edmund Optics) after passing through the whisker field. Ephus triggered individual camera frames (5 s, 2,500 frames per trial) synchronized with electrophysiological recordings.

Data analysis – Tuning curves and tuning surfaces. Tuning curves and surfaces were constructed after removing outliers (defined in "Glossary" subsection below). Phase tuning curves were formed by binning data into 30 bins with approximately equal numbers of observations in each. For tuning surfaces, the range of each variable of interest was divided into 10 (for θ_{amp}, $\theta_{setpoint}$ and f_{whisk}) or 30 (all other variables) equally spaced bins, unless otherwise noted. Bins with < 25 observations were removed from analysis and appear white in the surfaces. The color scale for surfaces depicts the mean spike rate (for single unit recordings, in Hz) or voltage (for intrinsic protractor EMG, in mV) for each bin, and is scaled linearly from 0 to the maximum for each surface. For M_0 vs M_0' tuning surfaces, in order to more uniformly distribute observations among bins, we used non-uniform bin sizes as follows. First, observations were transformed by the sigmoidal function:

$$y = \frac{2}{1+e^{-k*x}} - 1,$$

where x was the raw observation value, y was the transformed value, and k was a factor controlling the degree of nonlinearity. For M_0, F_{ax}, and F_{lat}, k was the 80th percentile value for the distribution of each variable. For M_0', F_{ax}', and F_{lat}', k was the 90th percentile value. Bins were determined as described above, and then data were transformed back using the inverse function:

$$x = -\frac{1}{k}[\log(1-y) - \log(1+y)].$$

We note that our tuning surfaces show responses only to combinations of mechanical variables obtained through whisking, rather than to arbitrary combinations that may never occur during behavior (e.g. high moments occur only after smaller moments, because moment builds up as the whisker bends against the object).

Data analysis – Generalized Additive Models (GAMs). We used statistical models to quantify the “instantaneous” (in 1 ms time bins) relationship between spike probability and various mechanical and kinematic variables. We used GAM statistical models because they offered improved performance over conventional Generalized Linear Models (GLMs; Figure 1.5A-D), yet preserve many of the advantages in interpretability that GLMs have over “black box” models such as Random Forests (Hastie et al., 2009; Wood, 2006). We fitted GAMs using the “mgcv” package in R (Wood, 2006), with a binomial error structure and logit link function. Each model was of the form:

$$logit(Y) = \sum_i f_i(X_i) + \epsilon$$

where Y is the expected spike probability in a 1 ms bin, and $f_i(X_i)$ is a smoothing spline of the *i*-th variable X_i, and ϵ is an error term. All variables were linearly interpolated from 500 samples/s (our high-speed video rate) to 1000 samples/s to match the binning of spikes. The smoothing for each spline determined using a method (UBRE method in mgcv package; Wood, 2006) to prevent overfitting (values obtained with and without 10-fold cross validation of the entire model were nearly indistinguishable). Separate GAMs were fitted to contact (Figures 1.4 and 1.5) and whisking in air (Figure 2.6) data. To be included in fitting and prediction for a whisking in air GAM, a frame could not be an outlier (defined in “Glossary” section of Appendix) for any of θ, ω, a, ζ. Similarly, to be included in a contact period GAM, a frame could not be an outlier for any of θ, ω, a,ζ, M_0, F_{ax}, F_{lat}, M_0', F_{ax}', or F_{lat}'. The goodness of fit was quantified using (1) Pearson correlation coefficient (r) between predicted spike probability and spike counts smoothed with a $\sigma = 4$ ms Gaussian kernel (in Figure 1.5 we show performance using kernels with $\sigma = 1, 2, 4, 8, 16$ or 32 ms), and (2) deviance, defined as -2 times the difference in log likelihood between the fitted model and a saturated model (with one data point per observation; (Crawley, 2002). The "deviance explained" was 1 minus the ratio of model deviance to deviance of the null (one data point total) model. Deviance is a standard metric for quantifying and comparing the goodness of fit for linear models (Crawley, 2002), and unlike Pearson correlation does not require smoothing. We also fitted GLMs to the same data for contact periods (Figure 1.5). GLMs were fitted with 10-fold cross validation using the "GeneralizedLinearModel" class in MATLAB with a binomial error structure and logit link function.

Viscoelastic model. We measured time series of bending moment ($M_0(t)$) and spike rate ($r_{spike}(t)$; in Hz) and formulated an empirical model of the intervening mechanics. We assume that M_0 resulting from whisker-object contact dominates viscoelastic stress such that strain can be a fixed function of M_0, and that the strain caused by M_0 saturates. First, a sigmoidal function transformed M_0 into strain:

$$\varepsilon(M_0) = \frac{2}{1+exp(-k \cdot M_0+C)} - 1 \qquad \text{(Eq. M1)}$$

where k (in (N-m)$^{-1}$) and *C* (unitless) are fitted parameters. Thus, ε ranges from -1 to +1 and can be thought of as a fractional change in displacement, $\Delta L/L_0$, where L measures displacement from a reference point in the follicle and L_0 is the starting value of L. The effect of non-zero *C* is to set a "resting" strain in the absence of contact, such that $\varepsilon \neq 0$ when $M_0 = 0$. We defined a "capped" version (ε_{spring}) of ε:

$$\varepsilon_{spring} = \begin{cases} \varepsilon_{lim}, & \varepsilon > \varepsilon_{lim} \\ -\varepsilon_{lim}, & \varepsilon < -\varepsilon_{lim} \\ \varepsilon, & otherwise \end{cases} \qquad \text{(Eq. M2)}$$

where ε_{lim} (unitless) is a fitted parameter. The quantities ε_{spring} and ε can be thought of as strain components dominated by elastic and viscous tissue interactions, respectively. The model is then in Kelvin-Voigt form:

$$\sigma = \sigma_{spring} + \sigma_{dashpot} = E \cdot \varepsilon_{spring} + \eta \cdot \frac{d\varepsilon}{dt} \qquad \text{(Eq. M3)}$$

where total stress (σ; in Pa) is the sum of elastic (σ_{spring}) and viscous ($\sigma_{dashpot}$) stress, and *E* (in Pa) and *η* (in Pa-s) are fitted parameters that can be thought of as elastic and viscous moduli, respectively. Finally, predicted spike rate ($\hat{r}_{spike}$; in Hz) was simply a scaled version of σ, limited to the interval [0 Hz, 1,000 Hz].

$$\hat{r}_{spike} = \begin{cases} 0 & \sigma \cdot q < 0 \\ 1{,}000 & \sigma \cdot q > 1{,}000 \\ \sigma \cdot q & otherwise \end{cases} \qquad \text{(Eq. M4)}$$

The scale factor *q* (in Hz Pa^{-1}) was fixed for all units at 1,000.

The five parameters of the model (k , *c*, ε_{lim}, E, and η) were fitted to $M_0(t)$ after outlier removal, and after scaling M_0 by the 80th percentile value of M_0 for each neuron (this scaling was absorbed by fitted parameter *k*). Fitting was performed (MATLAB "fmincon") by minimization of the squared error between r_{spike} and $\hat{r}_{spike}$ evaluated for frames containing contact and whisking. The goal of the model was to explain spike rate during contact for Merkel and other SA afferents. In total, 25 of 26 (Merkel and unidentified SA) afferents were included (the fitting algorithm failed on 1 SA afferent; Table S1). Interestingly, the ratio of elastic to viscous stress in our fitted models was larger for afferents that preferred contacts in the retraction direction (not shown), perhaps due to asymmetric strains that result from deflections of a whisker in opposing directions (Whiteley et al., 2015). A prominent contribution of viscoelasticity to Merkel spiking would suggest that steady-state measurements of strain (Whiteley et al., 2015) in the Merkel-dense region of the follicle may represent a lower bound.

Histology – trigeminal ganglion. Mice were perfused intracardially with PBS followed by 4% paraformaldehyde in PBS (PFA). Tissue was post-fixed in 4% PFA overnight. Trigeminal ganglia (TG) were removed from the cranium and embedded in 5% agarose in PBS. Coronal sections (100 µm) were collected on a vibratome (ThermoFisher Scientific). Sections were washed in PBS then incubated at 4°C in PBT (1% bovine serum albumin and 0.4% Triton-X 100 in PBS) for 1 hour. Cell bodies of TG neurons were labeled using rabbit anti-NeuN (Millipore, MABN140, 1:1000) followed by goat anti-rabbit Alexa Fluor 647 (ThermoFisher Scientific, A-21244, 1:500) in PBT. Sections were then washed in PBS and mounted in Vectashield with DAPI (Vector Laboratories, H-1200). Images were acquired using a CCD camera (QImaging, QIClick) on an epifluorescence microscope (Olympus, BX-41).

Histology – whisker pad. Mice were perfused and tissue post-fixed as described above. Whisker pads were dissected, depilated by chemical hair remover (Nair), and cryoprotected in 30% sucrose solution overnight. Pads were embedded in optimal cutting temperature solution (OCT, Tissue-Tek) and flash frozen at -80°C. Sections (100 µm) were collected on a cryostat (Leica). Sections were washed in PBS, incubated at 4°C in PBT for 1 hour, then stained using primary and secondary antibodies dissolved in PBT as follows. Merkel cells were labeled using rat anti-keratin 8 (Developmental Studies Hybridoma Data Bank, University of Iowa, TROMA-I, 2.5 µg/ml). Afferent endings expressing ChR2-YFP in *TrkC*^{CreER};*Rosa*^{Ai32} were stained using rabbit anti-GFP (Millipore, AB3080, 1:500). Afferent endings expressing tdTomato in *TrkC*^{CreER};*Rosa*^{Ai9} mice were stained using rabbit anti-RFP (Rockland, 600-401-379, 1:500). Secondary antibodies were goat anti-rat Alexa Fluor 647

(ThermoFisher Scientific, A-21247, 1:500) or goat anti-rabbit Alexa Fluor 488 (ThermoFisher Scientific, A-11008, 1:1000). Confocal images were acquired on an LSM 510 (Zeiss).

Histology – quantification. To quantify specificity of labeling of whisker pad Merkel afferents (Figure 1.2B), we obtained confocal stacks from three whisker pads of three $TrkC^{CreER}$;$Rosa^{Ai9}$ mice. We targeted for imaging all labeled afferent endings present in all macrovibrissae follicles in the three pads. This resulted in 472 confocal stacks obtained with a Zeiss Plan-Apochromat 20x 0.8 NA objective at a resolution of 512 pixels x 512 pixels, 0.82-1.16 μm/pixel, with 2-3 μm steps in the z-axis. Two observers, working independently but not blinded to genotype, manually scored each labeled afferent into one of the following categories: (1) Merkel-cell associated; (2) longitudinal lanceolate; (3) club-like; (4) other ending type; (5) unclassified, given to afferents in which the ending type could not be determined. For afferents in which the observers did not agree, the category was set to (5), unclassified. Because we obtained confocal stacks from every labeled afferent we could find, without regard to whether it left the tissue section before terminating, was poorly stained, etc., many afferents (652 of 1,705) were scored as unclassified. Of these unclassified afferents, most (433 of 652) were due to disagreement between the two observers, almost always (412 of 433) because one observer scored the afferent as a Merkel and the other as unclassified. No afferents were scored as (4), other ending type. Merkel afferents were further scored by one observer as innervating the superficial Merkel cells in the rete ridge collar (51 or 1,045), or as innervating the deeper Merkel dense region (994 of 1,045).

Whisker and other hair trimming. One day prior to electrophysiological recording, under isoflurane (1.5%) non-mystacial hairs on the left side of the face were trimmed short with fine forceps and microdissection scissors (Fine Science Tools). All whiskers and microvibrissae were trimmed short except β, γ, δ, B1-4, C1-4, and D1-4. For improved whisker tracking and improved follicle location estimates, we sought to minimize the hairs in the field of view that were not the whiskers of interest. We did not use chemical hair remover out of concern that it could compromise whisker mechanics. Thus, hair between the whiskers was manually removed by plucking. Non-whisker hairs were maintained at this short level by repeating this procedure as necessary.

Video analysis. The backbone of each whisker was tracked at subpixel-resolution using the Janelia Whisker Tracker (Clack et al., 2012), yielding a set of "traces" (tracked objects in image X-Y coordinates) for each frame. All subsequent processing to extract θ, M_0, F_{ax}, F_{lat} , and the minimal distance from whisker to pole, d_{pole}, was conducted in MATLAB according to published methods (Pammer et al., 2013), with several modifications described below in "Video analysis" subsections. We used the Hilbert transform to quantify the instantaneous phase (Φ), amplitude (θ_{amp}) and setpoint ($\theta_{setpoint}$) of bandpass (8-30 Hz, Butterworth) filtered θ (Hill et al., 2011). Instantaneous whisking frequency (f_{whisk}) was calculated based on the time derivative of Φ after unwrapping and conversion to whisk cycles.

Video analysis – pre-processing. The location or absence of the pole was automatically determined for each video frame using a mean squared error-based template matching algorithm. A number of events could render individual videos ineligible for further processing. These events included changes of pole position within a video, occasional failure of pole detection, grooming behavior, the experimenter introduced shadow of an optical fiber used for optogenetic stimulation, or whisker cutting manipulations. Individual trials were flagged by ad hoc heuristics as likely containing such events and marked for exclusion from further processing. Using a custom GUI, human curators manually inspected every trial and either verified the automatically determined status or, if necessary, corrected errors.

Video analysis – identifying tracked whiskers. To identify the same whiskers across frames we used a simple algorithm based on applying the following rules: (1) The location of the base $\vec{r}$ of a whisker trace in frame *t*, should have the smallest shift from $\vec{r}$ of the trace for the same whisker in the previous frame, *t-1*, among all candidate traces:

$$I_{interest}(t) = \underset{I_x(t-1)}{argmin} \left|\vec{r}_{I_{interest}(t)} - \vec{r}_{I_x(t-1)}\right|,$$

where $I_{interest}$(t) is the identity label of the whisker of interest at frame *t*, $I_x(t-1)$ is the identity label of any trace *x* at frame t-1, $\vec{r}_{I(t)}$ represents the base location of a trace labeled by $I(t)$. (2) The shift of the base location of a trace should not exceed 40 pixels per frame (0.64 mm per ms). With this constraint, if a match could not be found in a certain frame, the frame was skipped and the program reported it as a missing measurement. Trials with more than 1% (25 frames) missing measurements were excluded from analysis. (3) The anterior-posterior order of the follicle positions of identified whiskers was not allowed to change. (4) Traces with arc-length shorter than 100 pixels (3.4 mm) were ignored.

Video analysis – face masking. Computing time series of whisker bending moment at the follicle (M_0) relies on being able to measure curvature from the same point on the whisker (arc length distance from the follicle) and to estimate the follicle location across all video frames. As previously described (Pammer et al., 2013), the use of a "mask" to truncate the tracked whisker traces as they approach the face helped prevent tracking "noise" near the face. The follicle location was then estimated by extrapolation along the angle of the whisker base past the intersection of the whisker and the mask (Pammer et al., 2013). In prior work (Pammer et al., 2013), a single mask was used per whisker across frames and trials. Here we extended this approach by using a separate mask for each frame, obtained using a custom algorithm that fitted a smoothing spline to the contour of the face. First, we subtracted from each frame a spatially scaled version of itself:

$$i_{diff}(x, y) = i(x, y) - i(1.2\,x, 1.2\,y),$$

where $i(x, y)$ and $i(1.2\,x, 1.2\,y)$ were pixel values at coordinate (x, y) and $(1.2\,x, 1.2\,y)$ in a video frame, respectively. The origin $(0,0)$ was defined as the midpoint of the lower edge of the frame. Non-overlapping area between $i(x, y)$ and $i(1.2x, 1.2y)$ was excluded. The grayscale image i_{diff} was then converted to a binary image, b_{diff}:

$$b_{diff}(x, y) = \begin{cases} 0, & i_{diff}(x, y) < \frac{1}{2}\max(i_{diff}) \\ 1, & otherwise \end{cases}.$$

Because mice were head-fixed the face could appear only in a subset of pixels; the rest were set to 0:

$$b_{face}(x, y) = \begin{cases} 0, & y > 0.375\,x + 120 \\ b_{diff}(x, y), & otherwise \end{cases}.$$

A structural element 10 pixels wide and 1 pixel high was used (MATLAB "*strel*") to erode b_{face} (MATLAB "*imerode*") such that vertical structures were selectively removed.

A smoothing spline was fitted to points having pixel value 1 in the eroded b_{face} (MATLAB "fit"; smoothing parameter 1×10^{-5}). For faster computation, we reduced the smoothing spline to 10 equally spaced points (vectors) covering the segment of the face contour relevant for whiskers. The horizontal boundaries of this segment were determined for each frame by extending the minimal and maximal horizontal coordinates of identified whisker follicles by 30 pixels each. The resulting 10 vectors defining this segment were then scaled back by the factor of 1.2 used initially to compute i_{diff}.

We additionally applied a custom filter (across time) to handle rare occasions in which the mouse forepaw intruded into the image and caused sudden jumps in the fitted face contour. Taking the image x-coordinate of one point on the face contour at frame *t*, $x(t)$, as an example, the filter first obtained a "hypothesized" value of $x(t)$ as $x_{hypo}(t) = x(t-1)$. The initial estimate of $x(t)$ obtained from the process described above, $x_{initial}(t)$, was then combined with $x_{hypo}(t)$ to yield:

$$x(t) = k \cdot x_{hypo}(t) + (1-k) \cdot x_{initial}(t),$$

$$k = \min\left(\left|x_{hypo}(t) - x_{initial}(t)\right|, 0.98\, R_x\right) / R_x,$$

where k sets the relative weighting of x_{hypo} and $x_{initial}$ in the estimate, and R_x is a constant that sets the maximal per-frame jump. R_x was set empirically to 0.64 mm. The maximum value of *k* was limited to 0.98 in order to avoid x getting trapped at $x(t) = x_{hypo}(t)$. For the first frame of each trial, x_{hypo} was set to the value of $x_{initial}$. Image y-coordinates were filtered identically except the constant limiting the maximal jump, R_y, was empirically set to 0.32 mm.

The mask for each frame was then obtained by scaling the face contour by a user-settable factor to offset it slightly from the face (~10-20 pixels). As in prior work (Pammer et al., 2013), frames in which the tracked whisker did not intersect the mask were considered missing data. Thus, the user-settable factor was chosen to be as small as possible (to keep the mask as close as possible to the face) while also minimizing the number of frames without whisker-mask intersections.

Video analysis – whisker baseline curvature. Calculating change in whisker curvature at location p in time point t, ($\Delta\kappa_p(t)$, necessary to compute $M_0(t)$) depends on an estimate of the baseline curvature, $\kappa_p^{baseline}(t)$.

$$\Delta\kappa_p(t) = \kappa_p(t) - \kappa_p^{baseline}(t).$$

The $\kappa_p^{baseline}$ was derived from whisking-in-air curvature κ_p^{air}, i.e. in the absence of contact. However, when projected onto the video imaging plane, whisker curvature can appear to change due to roll of the whisker about its long axis (Knutsen et al., 2008) as well as to changes in elevation. To account for these variabilities, we used the following empirical model to estimate baseline for each time point:

$$\kappa_p^{baseline}(t) = f_{roll}(\theta(t)) + f_{elevation}(T),$$

where $f_{roll}(\theta(t))$ is a 2nd order polynomial fitted to $\kappa_p^{air}(t)$ as a function of θ across all trials and $f_{elevation}(T)$ is the median value of $\kappa_p^{air}(t) - f_{roll}(\theta(t))$ for each trial T (requires at least 50 frames, otherwise $f_{elevation}(T) = 0$ mm^{-1}). f_{roll} models the θ dependent variability in measured κ_p due to stereotyped protraction-dependent whisker roll (Knutsen et al., 2008). $f_{elevation}$ is a constant for each trial and models a slowly varying offset, presumably due to slow changes in whisker elevation. Finally, we calculated $\Delta\kappa_p$ for each time point as:

$$\Delta\kappa_p = \kappa_p - \kappa_p^{baseline}.$$

We estimated the effective "noise" level of our curvature estimates, σ_κ, for each session as:

$$\sigma_\kappa = 100\% \times \textstyle\sum_i \left|\Delta\kappa_p(t_i)\right| / N_{air} \div \sum_j \left|\Delta\kappa_p(t_j)\right| / N_{contact},$$

where t_i are the N_{air} time points across the entire session where $d_{pole} > 1$ mm and $\theta_{amp} > 2.5°$, and t_j are the $N_{contact}$ time points containing whisker-pole contact. This quantifies how large curvature changes measured during whisking in air were as a percentage of those measured during contact. As an estimate of "noise", σ_κ is conservative in that this assumes curvature change during whisking in air results from measurement error, whereas to some extent it may also include true inertial bending (cf. Figure 2.3). Across 33 sessions, mean σ_κ was 7.8 ± 5.0% (± SD).

Video analysis – whisker bending stiffness. Bending moment at location *p* depends on change in curvature and bending stiffness, $M_p = \Delta\kappa_p(EI_p)$. The bending stiffness, EI_p, is the product of Young's Modulus (*E*) and the area moment of inertia at *p*, (I_p), a geometrical quantity (Birdwell et al., 2007; Pammer et al., 2013). Thus, in addition to uncertainty in $\Delta\kappa_p$ (quantified above), uncertainty in moment must consider *E* and I_p. We used a fixed value of *E* = 5 GPa, obtained in prior work for the mouse C2 whisker (Pammer et al., 2013) by comparison of force-displacement data to numerical simulations that model the whisker as a tapered beam (Birdwell et al., 2007). Stress-strain curves measured from distal and proximal segments of rat whiskers indicate that *E* varies among individual whiskers (standard deviation: ~1.5 GPa; Quist et al., 2011) and along the length of an individual whisker (~35%; Quist et al., 2011), but not systematically with whisker row/arc identity. Because I_p depends on the fourth power of whisker radius (Birdwell et al., 2007; Pammer et al., 2013), whisker geometry is the more consequential factor in determining bending stiffness for tapered whiskers. This geometry can vary considerably across individual whiskers, across mice and even across time for individual mice. Here we obtained the individual whisker corresponding to every recorded neuron by plucking immediately following the recording session. This was particularly important for us because, in contrast to prior work that leveraged the stereotypy of whisker C2 (Pammer et al., 2013), we used several different whiskers. We mounted each plucked whisker on a glass slide and obtained high resolution (2.5 μm / pixel) brightfield images (BX-41 microscope, Olympus) covering the full length of the whisker using a CCD camera (QImaging, QIClick). Images were stitched together (FIJI; Preibisch et al., 2009), and the composite image was used to measure the whisker radius at points along its full length. We treated each whisker as a cone based on its radius at base and its length. Consistent with prior work (Hires et al., 2016), we found that the shape of individual whiskers deviated slightly from that of a pure cone (not shown), with uncertainty in I_p of ~50%. Taken together, our estimates of uncertainty in E, I_p and $\Delta\kappa_p$ imply that our reported values of absolute bending moment and forces must be considered approximations, accurate to no better than a factor of two (Taylor, 1997).

Video analysis – contact detection. We classified frames into those with and without whisker-pole contact using a strategy that combined machine learning with manual curation. Classification was performed using Random Forests (using MATLAB "TreeBagger" class). The predictor vector $\vec{x}$ for the *i*-th time point t_i was:

$$\vec{x}(t_i) = \left(d_{pole}(t_{i-k}), d_{pole}^{\prime}(t_{i-k}), \Delta\kappa_p(t_{i-k}), \Delta\kappa_p^{\prime}(t_{i-k})\right), \qquad k = -2, -1, 0, 1, 2$$

where $d_{pole}^{\prime}$ and $\Delta\kappa_p^{\prime}$ are derivatives with respect to time. Missing data points in the predictors were interpolated. A separate classifier was trained for each session. Training data were based on videos curated by trained humans using a custom GUI. We manually curated the contact status of 1,837,500 frames, on average 55,682 frames per session. Classifier performance for each session was tested using out-of-bag prediction on all manually curated data for a session. The overall rate of correct classification was 99.5 ± 0.2% (mean ± SD across 33 sessions) with a false positive rate of 0.3 ± 0.1%. The rates at which a one frame (2 ms) shift occurred between the predicted and true times of contact onsets and offsets were 10.2 ± 4.8% and 12.4 ± 4.3%, respectively. These performance metrics used only frames during whisking ($\theta_{amp} > 2.5°$), since non-whisking periods were not used in any analysis that depended on contact classification. That is, our contact classification was intended to be valid only for periods of whisking.

Video analysis – smoothing and differentiation. Trials with more than 2% of frames having missing θ, $\Delta\kappa_p$ or d_{pole} data were excluded. We first smoothed θ, M_0, F_{ax} and F_{lat} with a Savitzky-

Golay filter (3rd order, span of 9 frames), interpolating missing frames when possible. Angular velocity, acceleration and jerk were the first, second and third derivatives of θ with respect to time, $\omega \equiv \theta'$, $\alpha \equiv \omega'$, and $\zeta \equiv \alpha'$, respectively. Derivatives were calculated using central differences (via MATLAB "gradient"; e.g., for frame *i*, $\omega(i) = (\theta(i+1) - \theta(i-1))/2$). Derivatives for dynamic variables were $M_0' \equiv \Delta M_0/\Delta t$, $F_{ax}' \equiv \Delta F_{ax}/\Delta t$, and $F_{lat}' \equiv \Delta F_{lat}/\Delta t$, where Δ indicates a difference from frame *i* to *i*+1. Variables were smoothed with a Savitzky-Golay filter (3rd order, span of 9 frames) after each differentiation step.

Chapter 2: Stresses Underlying Whisker Self-motion Repsonses[2]

During whisking behavior in rodents, neurons in the brainstem (Moore et al., 2015), thalamus (Moore et al., 2015; Yu et al., 2006), and primary somatosensory cortex (Crochet and Petersen, 2006; Curtis and Kleinfeld, 2009; Fee et al., 1997; Hires et al., 2015) show responses modulated by whisk phase. In part because the whisker pad lacks classical proprioceptors such as muscle spindles (Moore et al., 2015), these self-motion responses have been hypothesized to serve a proprioceptive role, with whisk phase providing a coordinate system for object localization (Curtis and Kleinfeld, 2009; Kleinfeld and Deschenes, 2011; Szwed et al., 2003). Primary afferent spiking at specific whisk phases has been observed during "artificial whisking" (Szwed et al., 2003; Wallach et al., 2016), in which the whiskers are moved by muscles following electrical stimulation (Zucker and Welker, 1969), and even during behavior (Campagner et al., 2016; Khatri et al., 2009; Leiser and Moxon, 2007). However, the genetic identity and mechanical sensitivities of the neurons responsible for these self-motion responses have remained elusive.

We reveal that Merkel and SA afferents provide a source of self-motion signals that encode whisker position within the current whisker cycle (phase). We demonstrate that this phase coding arises from a combination of external and internal stresses. Finally, we show that the distribution of preferred phases across the population of afferents, which spans the whisk cycle, reflects diversity in tuning to stresses related to whisker inertia and the activity of specific muscles.

---

[2] Sections of this chapter are adapted from Severson et al., 2017.

Merkel and unidentified SA afferents encode whisk phase

We next investigated coding during whisking in air, in the absence of touch. The rhythmic motion of whisking can be decomposed into an amplitude, setpoint and phase (Harrington et al., 2011). Whisk phase (Φ) quantifies the position of the whisker within the current protraction-retraction cycle (Curtis and Kleinfeld, 2009; Fee et al., 1997; Hill et al., 2011; Szwed et al., 2003). Here, we found that all WT* afferents were also dramatically modulated by phase, with large changes in spike rate between non-preferred and preferred phases (Figure 2.1A-C; 2.1 ± 3.4 Hz vs 51.2 ± 105.7 Hz, respectively; median ± IQR; n = 15 total, including the earlier 13 WT* afferents and 2 additional SA afferents that were "putative" WT*: defined as responsive to manual whisker stimulation and meeting criteria for whisking in air responsiveness, but for which we did not collect whisker-pole contact data; Table S1). Preferred phase of each afferent was largely invariant across whisk cycles of different amplitudes, frequencies and setpoints (Figure 2.2). Across the population of afferents, preferred phase spanned the whisk cycle (Figure 2.1D,E).

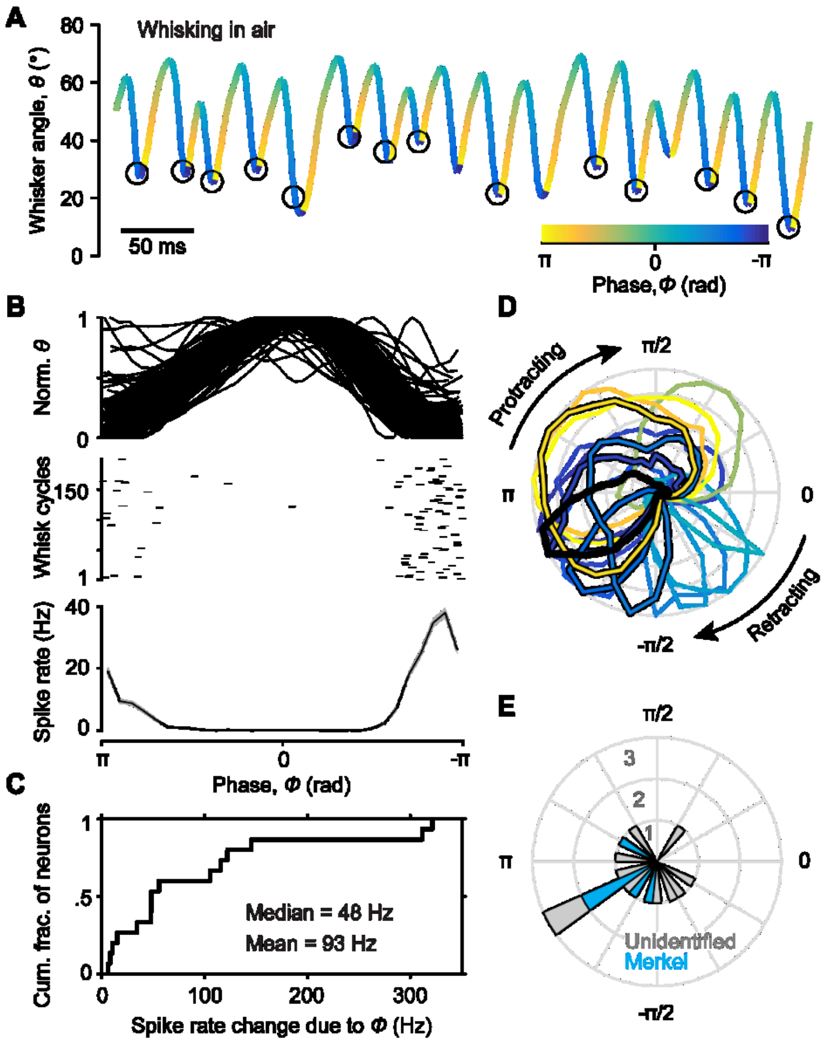

Figure 2.1 Self-motion responses encode whisk phase.

(**A**) Example whisker position trace overlaid with spike times (black circles) for a Merkel afferent during whisking in air. Color scale depicts phase within the whisk cycle. Spikes occurred near full retraction (phase of $-\pi/\ \pi$) during whisking. (**B**) Normalized and superimposed whisker position traces (top) and spike time raster (middle) for 200 whisk cycles randomly chosen from 6,325 total cycles, and mean spike rate (bottom; the "phase tuning curve"; ± SEM across all 6,325 cycles). Same afferent as in (A). (**C**) Cumulative histogram showing spike rate changes due to phase modulation (maximum minus minimum of the phase tuning curve) for WT* afferents (n = 15, including 5 Merkel, 9 SA and 1 RA). (**D**) Normalized phase tuning curves for WT* afferents in polar coordinates (n = 15). Preferred phase of each afferent is indicated by colors (color scale as in [A]). Merkel afferents (n = 5) include the black curve (example from [A]) and those with black outline. (**E**) Polar histogram showing the distribution of preferred phases (peak of tuning curves from [D]; blue: Merkels).

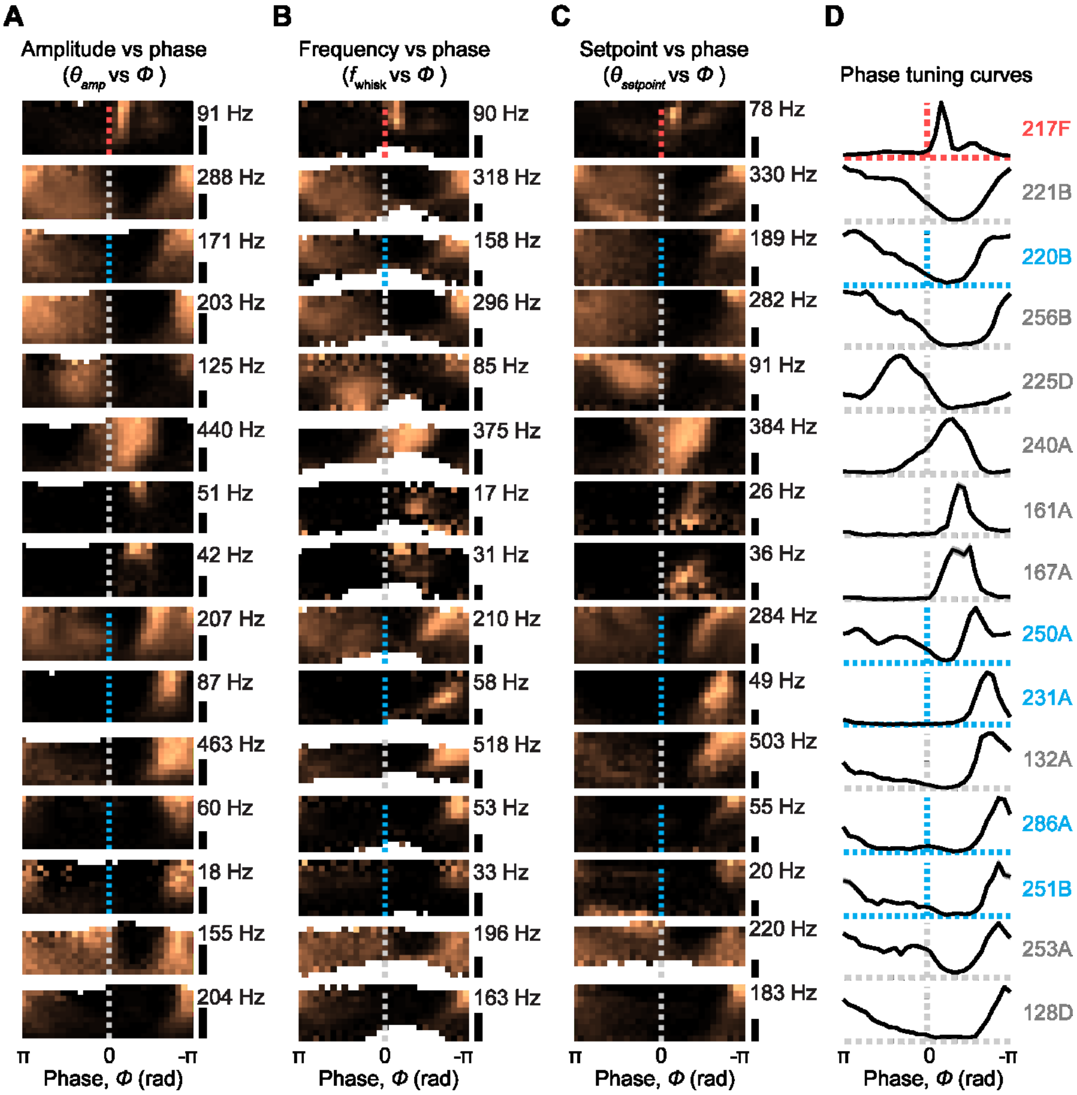

Figure 2.2 Phase tuning during whisking in air across amplitudes, frequencies and setpoints.

(**A**) Tuning surfaces for each afferent (n = 15 WT* afferents, arrayed vertically), showing spike rate binned by both phase (x-axis) and whisk amplitude (y-axis; scale bars: 10°). Color scale for each surface spans 0 Hz to a maximum firing rate (in Hz) indicated to the right of each panel. Vertical dashed lines mark phase of 0 and are colored according to afferent type (blue: Merkel; gray: SA; red: RA). (**B**) Tuning surfaces for the same neurons (rows aligned with [A]) but with spike rate binned by phase (x-axis) and frequency (y-axis; scale bars: 10 Hz). (**C**) Tuning surfaces for the same neurons (rows aligned with [A]), but with spike rate binned by phase (x-axis) and setpoint (y-axis; scale bars: 20°). (**D**) Phase tuning curves normalized and in Cartesian coordinates (mean ± SEM spike rate) for each neuron (rows aligned with [A]). Axes are colored by afferent type as in (A). Unit names are listed to allow identification in Table 1.

Phase coding arises from external and internal stresses

As muscles accelerate the whisker, a net moment is produced at the base of the whisker in proportion to the acceleration, $\vec{M} = I\vec{\alpha}$, where I is the moment of inertia. This moment will bend the whisker, cause strain in the follicle, and potentially open mechanically activated ion channels. However, muscle force must not only accelerate the whisker against its moment of inertia, but also overcome tissue viscoelastic forces that depend on displacement (θ) and velocity (ω) (we neglect air resistance). Mechanoreceptors may be directly sensitive to these internal (muscle and viscoelastic) forces.

To test whether phase tuning depended on $\vec{M}$, the moment caused by the whisker's resistance to rotation, we performed an experiment in which we progressively cut off distal segments of the whisker and re-measured tuning (Figure 2.3). In recordings from a new set of putative WT* afferents (n = 13, including 12 SA and 1 RA), we first obtained baseline responses during whisking in air. Next, we cut off a distal portion of the whisker, thereby reducing the whisker's moment of inertia and thus $\vec{M}$, and recorded new responses from the same afferent. We repeated this process for up to three cuts, shortening the whisker eventually to near its base (Figure 2.3A; final length: 0.37 ± 0.43 mm, mean ±

SD, n = 13) and thus dramatically reducing its moment of inertia, $I \sim 0$, and abolishing $\vec{M}$. Spiking during whisking in air was eliminated by this manipulation for a subset (6 of 13) of afferents (Figure 2.3B,E; from 50.1 ± 42.3 Hz for intact whisker, to 0.9 ± 0.7 Hz after final cut, mean ± SD, n = 6, including 5 SA and 1 RA). Spike rates from these afferents increased with acceleration (Figure 2.3B; either positive or negative acceleration), as expected if whisker inertia drove spiking. Other afferents (7 of 13) showed self-motion responses that remained after cutting (Figure 2.3C-E; 86.1 ± 71.5 Hz for intact whisker vs 70.3 ± 58.5 Hz after final cut, mean ± SD, n = 7 SA), with phase tuning curves that were largely (Figure 2.3C) or partially unchanged (Figure 2.3D). Thus, for some afferents internal forces are sufficient to produce strong, phase-tuned spiking.

Strikingly, preferred phases across the population not only spanned the whisk cycle when whiskers were intact (Figure 2.1 and Figure 2.3F), but largely did so even after whiskers were fully cut (Figure 2.3G). How does this distribution of phase preferences relate to the underlying mechanical sensitivities of each afferent?

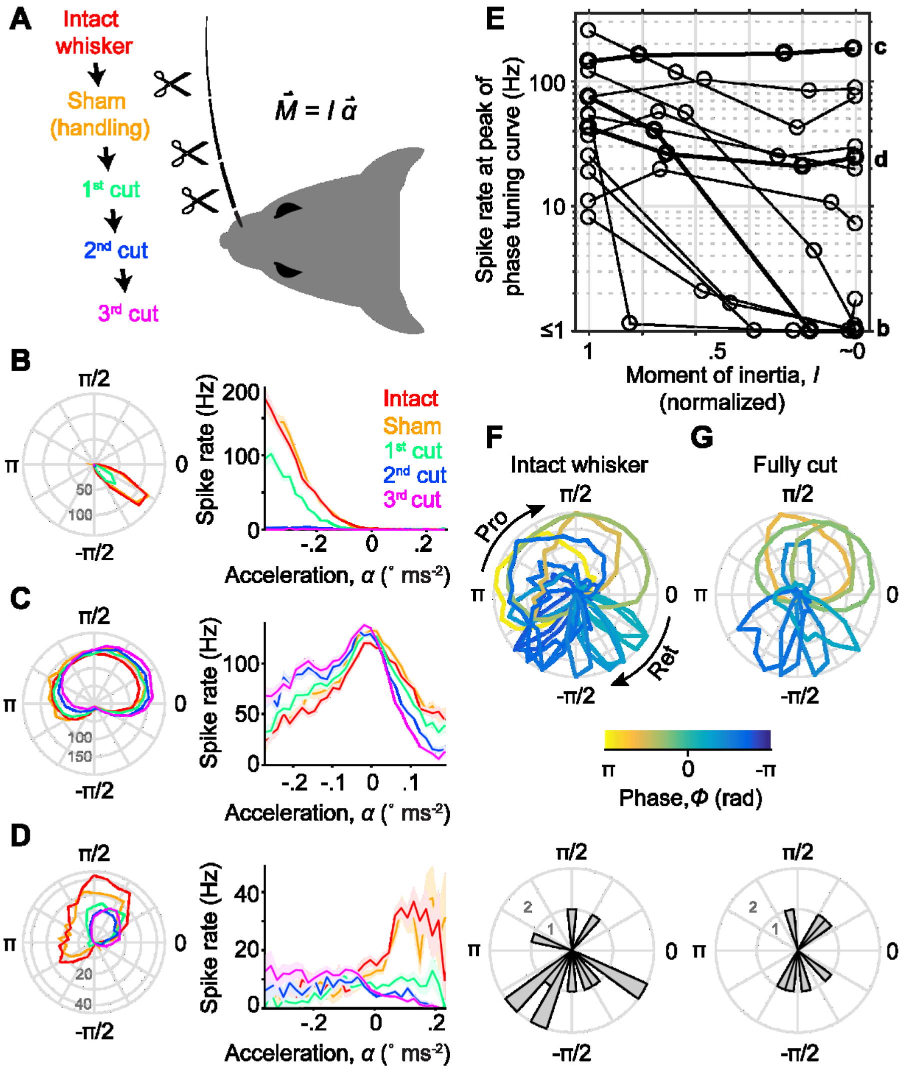

Figure 2.3 Self-motion responses arise from both external and internal stresses.

(**A**) Schematic of the experiment. Responses during whisking in air were recorded across progressive cuts to shorten the relevant whisker and decrease its moment of inertia, *I* (resistance to change in angular motion). Bending moment at the base of the whisker ($\vec{M}$), proportional to *I* and angular acceleration ($\vec{\alpha}$), was thus progressively reduced. As a control, prior to cutting the whisker was it was handled in a sham manipulation. (**B**) Tuning curves for phase (left) and acceleration (right; ± SEM) are shown for an example SA afferent across cutting conditions (colors, as in [A]). Afferent showed gradual reduction of spike rates down to zero as the whisker was progressively cut to its base (i.e. when *I* ~ 0). Note that preferred phase remained constant as overall spike rate decreased. (**C**) Example

SA afferent with little change in responses after progressive cutting even in the "fully cut" condition. Conventions as in (B). Example SA afferent with response that were reduced but not eliminated by cutting. Conventions as in (B). (**E**) Summary showing spike rate at the preferred phase for each afferent (n = 13 SA), as a function of the remaining whisker moment of inertia (normalized to intact condition). Examples from (B-D) are plotted with thick lines and indicated at right by corresponding lower case letters (b,c,d). A log scale for the spike rate axis accommodates the wide range across afferents. (**F**) Overlay of normalized phase tuning curves (top) and histogram of preferred phases (bottom) for each afferent (n = 13 SA) from the intact whisker condition. Conventions as in Figure 2.1D-E. (**G**) As in (F) but for fully cut whisker conditions (n = 7; only neurons with ≥ 3 Hz peak response).

Distribution of phase preferences mirrors tuning to inertial and muscle-specific stresses

Muscles controlling whisking (Dorfl, 1982; Haidarliu et al., 2015; Haidarliu et al., 2010; Wineski, 1985) are active at distinct phases of the whisk cycle in rats (Hill et al., 2008). We collected simultaneous high-speed video and EMG data from mice for two major muscle groups that control whisking, the intrinsic protractor (IP) and *m. nasolabialis* (NL) muscles (Figure 2.4A, solid curves; Figure 2.5). EMG phase modulation in mice (Figure 2.4A, solid curves) was similar to that in rats (Figure 2.4A, dashed curves; data taken from Hill et al., 2008), as expected from their isomorphic whisking musculatures (Haidarliu et al., 2015; Haidarliu et al., 2010). Whisk phase was also associated with stereotyped patterns of whisker acceleration and jerk (Figures 2.4B and 2.6). Can these patterns of muscle activation and kinematics explain the phase tuning curves we observed?

We examined in further detail the phase tuning curves obtained before (Figure 2.4C) and after (Figure 2.4D) whisker trimming from individual afferents. For those afferents that continued to spike after whisker trimming, the phase tuning curves were correlated with activation of either IP or NL muscles (Figure 2.4D, bottom 7 afferents; Pearson correlation between phase tuning and EMG curves: $r = 0.66 \pm 0.27$, mean ± SD, n = 7 SA afferents; same afferents as in Figure 2.3G). Thus, spiking in these afferents after whisker trimming was likely due to muscle-induced stresses. For each afferent, we subtracted the cut-whisker phase tuning curve from the intact-whisker phase tuning curve to obtain a measure of the net spike rate "lost" at each phase following the abolishment of whisker inertia (Figure 2.4E). These subtracted tuning curves were correlated with positive acceleration, negative acceleration or jerk (Figure 2.4E; $r = 0.71 \pm 0.19$, mean ± SD, n = 13). In separate experiments, we obtained additional recordings from putative WT* afferents (Figure 2.4F; n = 5 total, including 3 Merkel and 2 SA) in which the whisker had already been cut to near its base (within ~0.5 mm of the follicle). Phase tuning curves in these afferents were strongly correlated with EMG from either IP or NL muscles (Figure 2.4F; $r = 0.76 \pm 0.06$, mean ± SD, n = 5).

We found striking similarities between the average phase modulation of spike rate in individual afferents and the average phase modulation on kinematic variables related to inertial forces and IP or NL muscle activity. Comparison of EMG activity with simultaneously measured whisker kinematics showed strong correlations between IP muscle activity and positive whisker velocity (Figure 2.5B,D), and between NL activity and negative velocity (Figure 2.5F,H). This suggests that statistical models fitted to instantaneous kinematic variables (which together reflect the combined actions of internal forces and whisker inertia) should be able to account for self-motion responses and their modulation by whisk phase. We again fitted GAM statistical models, this time to explain spike rate as a function of combinations of kinematic variables during periods of whisking in air for all WT* afferents (n = 28, same afferents as in Figure 2.1 and "intact" whisker condition of Figure 2.3; Table 1). For each model, we then calculated the Pearson correlation between predicted and actual phase tuning curves (Figure 2.7A,B). While afferents typically showed poor sensitivity to single kinematic variables (position, velocity, acceleration or jerk; θ, ω, a, or ζ), combinations of three or more variables predicted phase tuning curves nearly perfectly (full model with θ, ω, a, and ζ: $r = 0.97 \pm 0.04$, mean ± SD, n = 28, including 5 Merkel, 22 SA and 1 RA; Figure 2.7A,B). Thus, phase tuning can also be understood as a sensitivity of each afferent to a specific region within multidimensional kinematic space (Figure 2.7C; our results thus confirm in identified afferents of awake mice the results of Wallach et al., 2016).

Together, our results show that phase tuning arises from external (inertial) forces and internal forces that mirror the activation of specific muscles, which in combination allow afferents to respond with preferred phases that span the whisk cycle (Figure 2.4G).

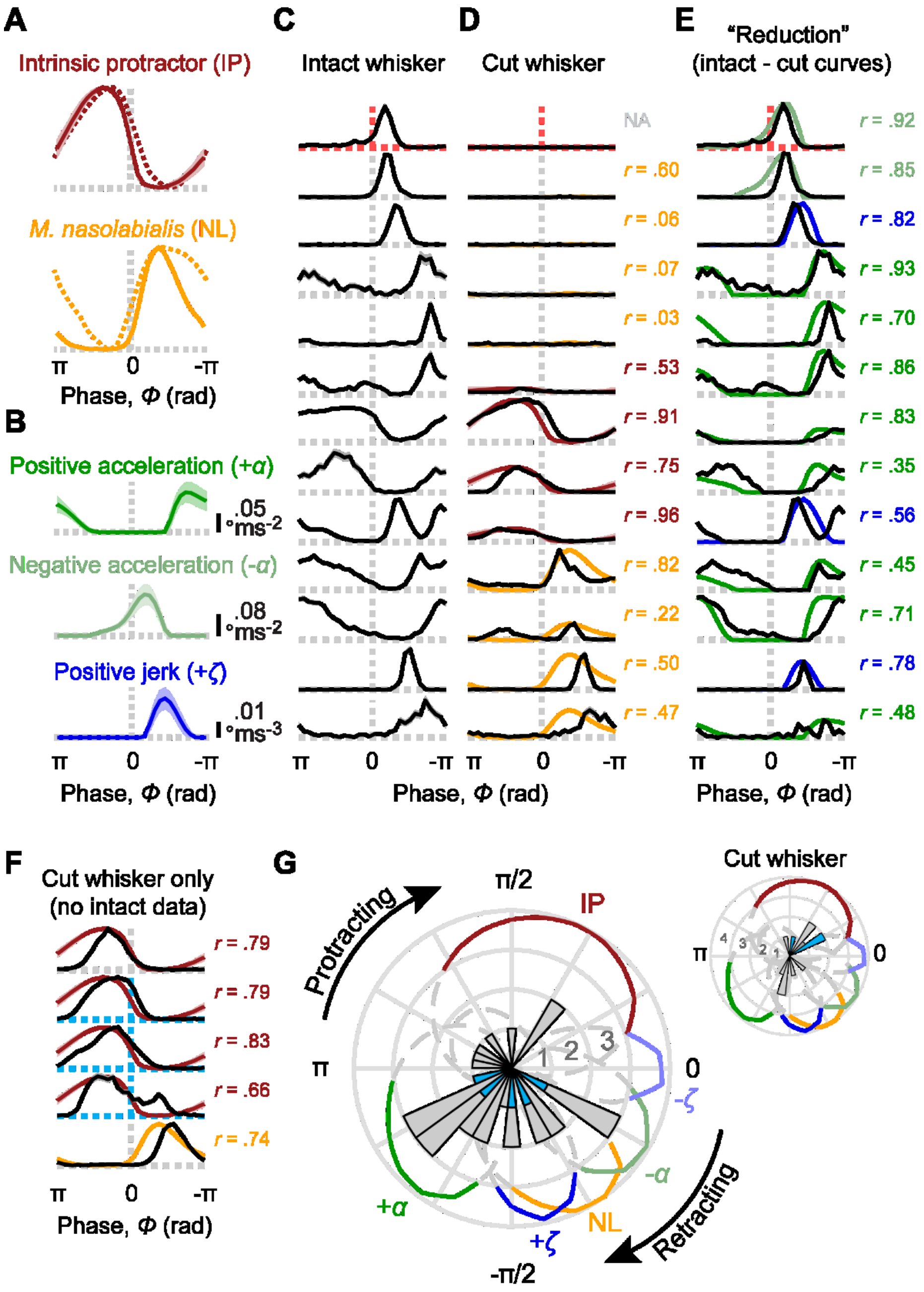

Figure 2.4 Phase coding reflects tuning to inertial and muscle-specific stresses.

(**A**) Electromyogram (EMG) as a function of whisk phase is shown for two main whisking muscles, the intrinsic protractors (top, solid brown; mean ± SD across n = 3 mice), and the extrinsic retractor *m. nasolabialis* (bottom, solid yellow; n = 1 mouse). Overlaid are published rat EMG data for the same muscles (dashed curves; obtained from Hill et al. 2008). (**B**) Absolute values of positive acceleration (+*α*; top, dark green), negative acceleration (-*α*; middle, light green) and positive jerk (+*ζ*; bottom, dark blue) as a function of whisk phase (mean ± SD after setting values with opposite sign to 0; n = 53 recording sessions). (**C**) Normalized phase tuning curves (± SEM) for afferents in the progressive whisker cutting experiment, prior to cutting (same afferents as in Figure 2.3E). Dashed lines indicate phase 0 (vertical dashed lines) and spike rate 0 (horizontal) and are colored by afferent type (gray: SA, n = 13; red: RA, n = 1). (**D**) Afferents from (C) shown for the fully cut whisker condition. Afferents are aligned by rows with (C) and displayed on the same vertical scale (normalized across intact and cut conditions). Mouse EMG traces from (A) are overlaid for each afferent based on the best match (Pearson correlation coefficient between EMG and spike rate tuning curves, *r*, shown to right of each curve; NA: correlation not computed due to zero spikes). (**E**) Same afferents as in (C, D), aligned by rows and with same normalization, but showing apparent "reduction" in spike rate at each phase, obtained by subtracting cut from intact whisker tuning curves. Negative values were set to zero. Mean kinematics traces from (B) are overlaid for each afferent based on the best match (Pearson correlation coefficient, *r*, between curves; shown to right of each pair of curves; matches chosen from among $\pm a$ and $\pm \zeta$). (**F**) Same as (D) but for additional afferents (n = 3 Merkel and n = 2 SA; Merkels: blue dashed lines) recorded after the whisker had already been cut. (**G**) Summary polar histogram showing preferred phase for all WT* afferents (n = 28, including 5 Merkels, 22 SA and 1 RA; blue bars: Merkels). Colored traces illustrate the normalized kinematics and EMG curves from (A, B) in polar coordinates (shown dashed and gray below 75th percentile for clarity). Inset, histogram of preferred phase for all recordings in which the whisker was fully cut (n = 12 including 3 Merkel and 9 SA; n = 6 not plotted due to ≤ 3 Hz peak rate).

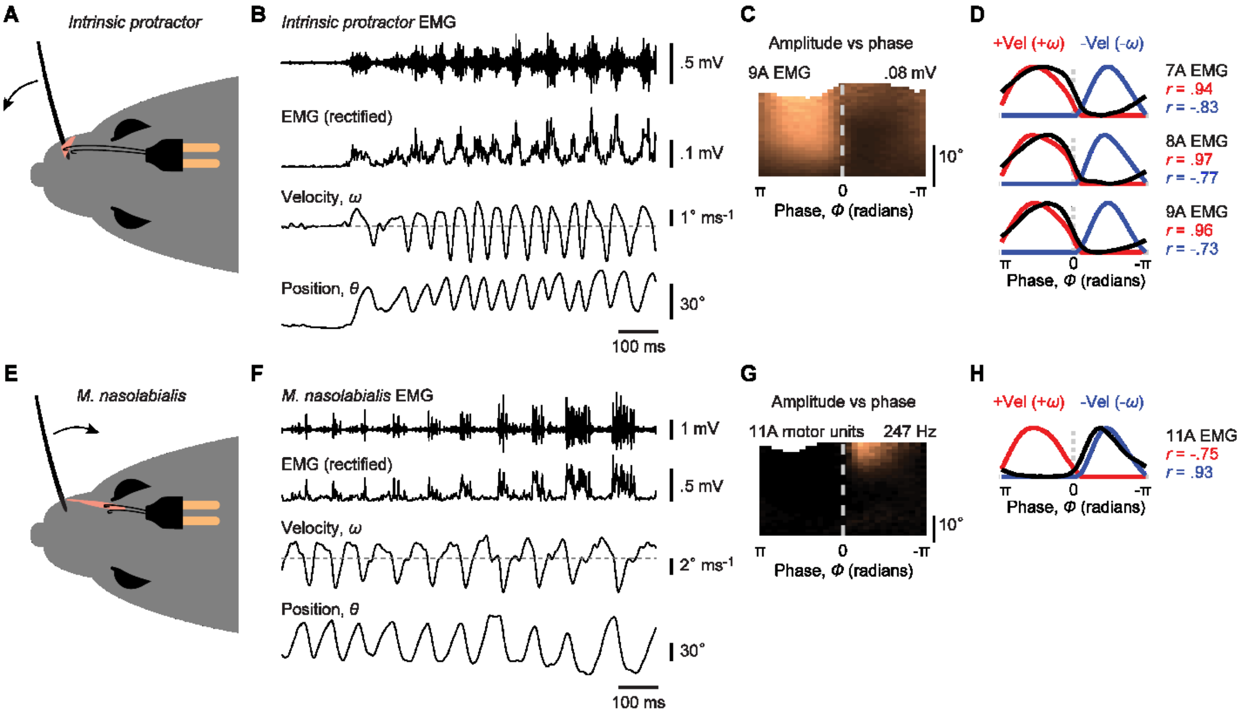

Figure 2.5 Electromyogram (EMG) recordings from muscles that drive whisking.

(**A**) Schematic of chronic EMG recording procedure targeting intrinsic protractor muscle. During implantation of electrodes at this site, current stimulation resulted in whisker protraction. (**B**) Example EMG signal recorded together with high-speed whisker video during exploratory whisking. Rectified EMG signals were averaged into 2 ms bins. Intrinsic protractor activity peaked while velocity (ω) was positive, prior to peak position (θ). (**C**) Tuning surface for intrinsic protractor recording in (B), showing mean rectified EMG as a function of whisk phase (x-axis) and amplitude (y-axis, scale bar: 10°) measured from high-speed video (30 equally spaced bins for both phase and amplitude). Color ranges from 0 (black) to 0.08 mV. (**D**) Traces of mean rectified EMG (black curves) as a function of phase, for each of three intrinsic protractor recordings. Traces of mean whisker velocity as a function of phase were split into positive (red) and negative (blue) values, rectified and overlaid for each recording. Pearson correlation coefficients shown at right indicate that intrinsic protractor muscles and positive velocity were highly correlated within whisk cycles. (**E**) Schematic of chronic EMG recording procedure to target the extrinsic retractor muscle *m. nasolabialis*. During electrode implantation, passing current resulted in whisker pad retraction. (F) Example EMG signal for *m. nasolabialis*, with whisker velocity and position from high-speed video. Motor unit spikes were prevalent in this recording. Extrinsic retractor activity peaked while velocity was negative, just after peak position. (**G**) Same as (C), but based on motor unit spike rate. Color ranging from 0 (black) to 247 Hz. (**H**) Same as (D), but for *m. nasolabialis* recording, showing high correlation with negative velocity within whisk cycles.

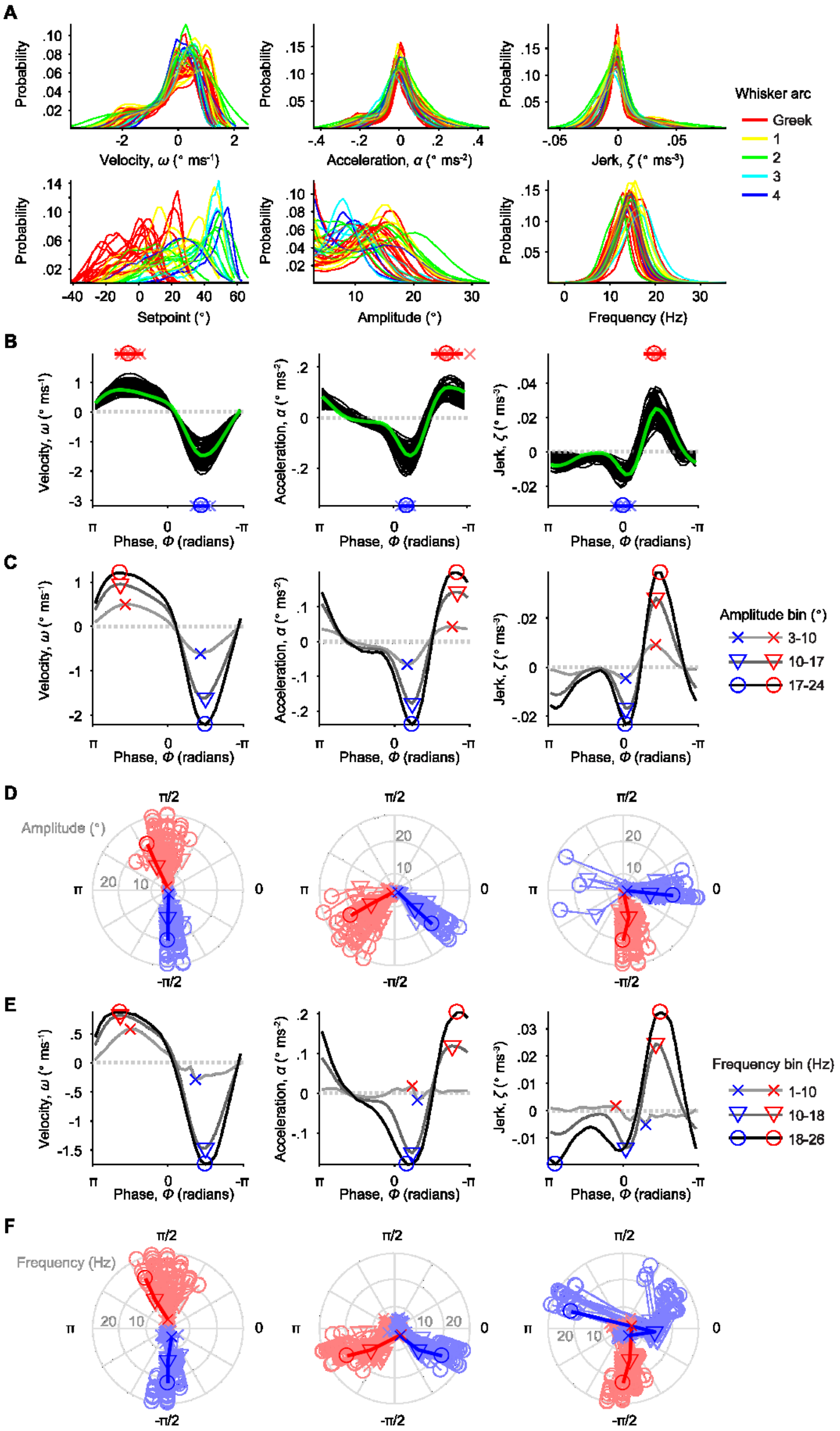

Figure 2.6 Distributions of kinematics and degree of invariance of kinematics with phase.

(**A**) Traces in each panel show probability distributions of a kinematic variable (indicated under each plot) for individual recording sessions (n = 33 sessions). Colors indicate whisker arc (columnar identity in whisker array on face). (**B**) Traces show the mean velocity (left), acceleration (middle), or jerk (right) binned by phase (x-axis) for the recording sessions in (A). Green traces show one example session. Crosses indicate the phases at which positive (red) and negative (blue) peaks occur for individual traces. Corresponding circles and error bars show the mean ± 3 SD of these peaks. (**C**) Mean kinematics binned by phase (x-axis) and amplitude (grayscale traces; bins indicated in legend at right) for the example session (green curves) in (B). Markers indicate the phases where positive (red) and negative (blue) peaks occur for low (cross), middle (triangle), and high (circle) amplitude bins, respectively. (**D**) For all sessions, phase (angular axis) and amplitude (radial axis) values of the peaks extracted as in (C). Color and symbol conventions as in (C). Peaks from the same sessions are connected by lines. Data from the example session in (B) are plotted with thick lines. (**E, F**) Similar to (C, D) but for whisk frequency instead of whisk amplitude. The phases where peaks in kinematics occur are largely invariant across amplitudes and frequencies, except for negative jerk.

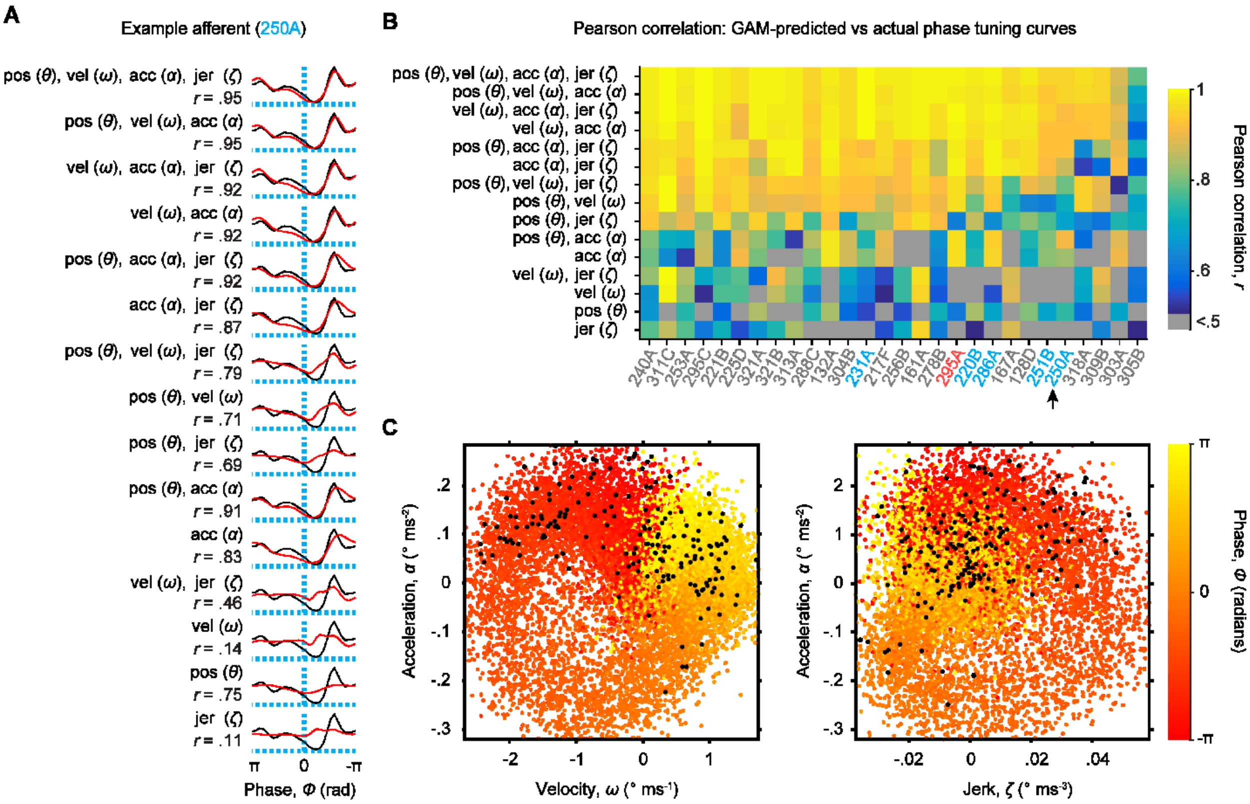

Figure 2.7 Phase tuning in terms of instantaneous combinations of kinematic variables.

(**A**) Each row shows an overlay of the observed phase tuning curve (black, same in each row) for an example Merkel afferent and a tuning curve predicted from a GAM model (red) fitted to one of 15 possible combinations (indicated at left) of four kinematic variables (*θ*, whisker position; *ω*, velocity; *a*, acceleration; *ζ*, jerk) during whisking in air. Pearson correlation coefficient between observed and predicted curves, *r*, is shown to the right for each row. (**B**) Heatmap of *r* quantified as in (A) for each model type (kinematic variables listed at left) for all WT* neurons (columns). Gray indicates *r* values < 0.5. Arrow indicates the example afferent from (A). Afferent names along the x-axis are colored by afferent type (blue: Merkel; gray: SA; red: RA). Models containing at least acceleration and velocity (or jerk) produced good performance, while those lacking acceleration generally performed worse. (**C**) Spikes during whisking in air are triggered in a confined region of kinematic subspace, giving rise to phase tuning (inspired by Wallach et al. 2016). Left, Each point in the background is the instantaneous acceleration (y-axis), velocity (x-axis), and phase (color) for a random subset of frames (15,000 out of ~590,900 total) for the example afferent in (A). In the foreground, another random subset of frames were drawn (1,500 of ~590,900) and those with spikes were plotted as black dots. Right, Same as left panel but acceleration and jerk, and with different randomly chosen frames.

Discussion

Our data reveal Merkel afferents to be a likely source of these widely observed responses, with activity that (like unidentified SA afferents) was exquisitely phase tuned. Thus, Merkel afferents send proprioceptive information to the brain. The behavioral contexts that rely on whisker proprioception are under active investigation (Knutsen et al., 2006; Mehta et al., 2007; O'Connor et al., 2013).

The distribution of preferred phases across our population of afferents spanned the whisk cycle, with a slight abundance during the retraction phase (Figure 2.4G). Although examples of phase-tuned afferents have been shown previously (Bermejo et al., 2004; Campagner et al., 2016; Khatri et al., 2009; Leiser and Moxon, 2007) (1-6 per paper), only two prior studies have reported samples large enough to permit analysis of the distribution of preferred phases (Szwed et al., 2003; Wallach et al., 2016). Both used artificial whisking and found, like our study in awake animals, that preferred phase spanned the whisk cycle (Szwed et al., 2003; Wallach et al., 2016). However, each study found a relative abundance of preferred phases during the protraction phase (Szwed et al., 2003; Wallach et al., 2016). Our results suggest that the preferred phase of a given afferent will depend on its sensitivity to a specific combination of external and internal stresses (Figure 2.4G), which could differ not only across experimental preparations but also modes of behavior. For instance, we found individual afferents whose phase tuning mirrored that of specific muscles (intrinsic protractor and *m. nasolabialis*). The degree of activation of these muscles differs across artificial and natural whisking and may also differ across behavioral conditions. While downstream circuits receive strongly phase-tuned spiking from the population of afferents, we speculate that the shape of this distribution may vary systematically with different modes of whisking, and be interpreted in the context of central signals that represent aspects of whisking other than phase (Hill et al., 2011).

Approximately a third of individual afferents responded robustly during self-motion, encoding whisk phase in the absence of touch. These afferents also responded during touch, raising the question of how self-motion responses can be "deconvolved" from touch responses. This is a problem also faced by other proprioceptive systems. Microneurography studies in humans have found, and suggested proprioceptive roles for, cutaneous afferents that respond both to touch and to voluntary movements of the hand (Edin and Abbs, 1991; Hulliger et al., 1979) and face (Johansson et al., 1988; Trulsson and Johansson, 2002). We found that a subset of Merkel and unidentified afferents respond to whisking and touch (WT), while others respond only to touch (T). Moreover, primary afferents that respond to whisking but not touch (W) have previously been reported (Szwed et al., 2003), and may arise from Merkel- or non-Merkel afferents (Ebara et al., 2002; Rice et al., 1986) not in sampled in our work. Thus, downstream circuits could deconvolve self-motion from touch responses at the population level, by comparing activity from afferents that respond to self-motion and touch with activity from those responding to either whisking or touch alone. Alternatively, self-motion and touch responses could also be separated by accelerating non-linear input-output curves in downstream circuits (Moore et al., 2015).

Finally, we demonstrate that phase tuning arises from both external and internal forces that reflect whisker inertia and the activity of specific muscles, and suggest that, across the population of afferents, the balance of these factors allows preferred phase to span the whisk cycle. Together, our data suggest that Merkel afferents in the mouse whisker system are positioned to play a dual role in both proprioception and touch, sending to the brain multiplexed information in two somatosensory modalities critical for perception.

Materials and methods

Methods for surgery, behavioral training and apparatus, electrophysiology, optogenetic identification of Merkel afferents, high-speed videography, tuning curves and tuning surfaces, Generalized Additive Models, whisker and other hair trimming, video analysis, video pre-processing, identifying tracked whiskers, face masking, and smoothing and differentiation were identical to those used in the previous chapter. Additional methods used in this chapter are listed below.

Progressive whisker cutting experiment. Trigeminal ganglion recordings were conducted as described earlier. The recording electrode was advanced by the micromanipulator until a well-isolated unit responsive manual stimulation and active whisking was found. High-speed video was continuously recorded, including both active whisking periods and manual manipulations. While the whisker was at its full length, whisking in air (WIA) responses were recorded as the mouse actively whisked for several minutes. At the beginning of the experiment and following each manipulation, unit responses to manual touch were briefly recorded to enable online and post-hoc matching of touch-evoked and whisking-evoked spike waveforms, thus ensuring correct mapping of the unit's receptive field. A sham handling manipulation, an internal control, was conducted to test the assumption that whisker handling did not affect WIA responses. The whisker shaft was held gently with Teflon-tipped forceps (Electron Microscopy Sciences) for several seconds and released. After sham handling and subsequent manipulations, the same unit's WIA responses were recorded for several minutes. For the first cut and subsequent cutting manipulations, the whisker was held with forceps, and a piece measuring approximately one third of its length was cut with microdissection scissors. The cut whisker fragment was collected in a plastic tube for post-hoc measurement. For most experiments, this cutting, collection, and recording procedure was repeated for a second and third cut. After the final cut, the external length of the whisker was near zero. Any remaining external whisker length was measured immediately after the experiment with a microruler while the mouse was under isoflurane anesthesia.

Collected whisker fragments were transferred from the tube and arranged on a glass microscope slide. A glass cover slip was placed over the mounted whisker and fixed in place with nail polish. Brightfield images (BX-41 microscope, Olympus) of each fragment were obtained at high resolution (1 μm / pixel) using a CCD camera (QImaging, QIClick) and stitched together (FIJI; Preibisch et al., 2009). The lengths of each fragment were summed to find the total length of the intact whisker. The base radius (R; in m), total intact length (L; in m), and remaining length (x; in m) were used to estimate moment of inertia (I; in kg·m^2) of the whisker in the intact ($L = x$) and post-cut conditions ($L >$ x) for subsequent analysis. The whisker was assumed to be an ideal, rigid cone rotating about an axis perpendicular to its long axis and located at the center of its base. I was estimated by the equation:

$$I = \pi\rho R^2\left(\frac{1}{5L^2}x^5 - \frac{1}{2L}x^4 + \frac{1}{3}x^3\right)$$

where whisker density (ϱ) was assumed to be 2000 kg/m^3.

Sweeps with manual manipulations (touch, handling, cutting) were identified using high-speed video and removed from further analysis. The video recording session was partitioned into "cutting groups" that included all sweeps prior to any cutting or handling manipulation (*intact*), following sham handling (*sham*), and following each *n*-th cut (*Cut n)*. Because the fully cut whisker could not be tracked, kinematic quantities were acquired from a surrogate whisker (described below). Spike waveforms were obtained and clustered across the entire session as described above. Units were included in further analyses if the shape and amplitude of the mean waveform of manual touch-evoked spikes did not change significantly over time and matched the mean waveform of whisking-evoked spikes (if any) for each cutting group.

Video analysis – tracking "surrogate" whiskers. In three experimental conditions, we used surrogate whiskers because the whisker of interest could not be tracked. (1) When the whisker was cut progressively (Figure 2.3), after the final cut the whisker was too short to track. In order to maintain consistency of kinematic measurements across the sequential cuts, we tracked a "surrogate" whisker throughout the experiment, typically the most caudal remaining whisker. (2) Experiments in which the whisker of interest had been cut prior to start of recording (Figure 2.4F). In these cases, the surrogate whisker was from the same whisker arc as the whisker of interest. (3) We included two afferents in our analysis of phase tuning (Figures 2.1C-E, 2.7 and 2.4G) obtained while multiple rows of whiskers were intact and occluded tracking of the whisker of interest. In these cases, we typically tracked the most caudal whisker. For all data based on surrogate whiskers, only trials with no pole in reach of the whiskers were included, such that no contacts could occur.

EMG implantation surgery. Adult mice (6-26 weeks old) were implanted with titanium headposts (Yang et al., 2016) and allowed at least 2 days to recover. Electrodes were made by connecting PFA coated tungsten microwire (50 μm, A-M Systems, #795500) to gold-plated pins (WPI, #5482). The pins were insulated with heat-shrink tubing, and then glued together and fixed to the headpost using cyanoacrylate glue (Krazy Glue) and dental acrylic (Jet Repair Acrylic). An incision was made in the skin caudal or dorsal to the target muscle. One pair of wires was implanted in each mouse into either *m. nasolabialis* or the intrinsic protractors. The coating at the end of each wire was stripped 0.5-1.0 mm and bent to form a hook. The hooked end of each wire was placed into the beveled end of a 30G needle (BD, #305128) to shuttle it beneath the skin to the target muscle. The two wires were placed ~1 mm from each other in the target muscle. Bipolar current was applied across the pair of wires using a stimulus isolator (WPI, A365) to induce movement. Implantation was considered successful if minimal stimulation (25-100 μA) produced movement characteristic of the target muscle (*m. nasolabialis*, pad retraction; intrinsic protractors, specific protraction of a few adjacent whiskers). The incision was sutured closed (8/0, Fine Science Tools #12051-08) and covered with antibiotic ointment (Pac-Kit). Mice were allowed at least 1 day to recover before recording.

EMG recording and analysis. Fur and all whiskers except those in C row were trimmed short with microdissection scissors (Fine Science Tools). The mouse was head-fixed and allowed to run on the treadmill. EMG signals were acquired in 5 s trials synchronized with high-speed whisker video. The differential signal between the two wires was amplified 1,000x, bandpass filtered between 1 Hz and 10 kHz (DAM80, WPI) and acquired at 20 kHz using Ephus. After recording, signals were bandpass filtered between 400 Hz and 3 kHz (Butterworth, 7th order). For intrinsic protractor recordings, the signal was then rectified and binned to obtain the mean rectified EMG for each 2 ms high-speed video frame. For the *m. nasolabialis* recording, we observed apparent motor unit spikes (Deschenes et al., 2016), and obtained the times of these spikes by thresholding the bandpass filtered signal. The *m. nasolabialis* phase tuning curve (Figures 2.4A and 2.5G-H) was then obtained using these motor unit spike times. Whisk phase was determined by tracking a C-row or Greek whisker.

Data analysis – Calculation of kinematic variable probability distributions. Curves depicting mean kinematic variables (ω, a, ζ, θ_{amp}, $\theta_{setpoint}$ and f_{whisk}) as a function of phase (Figures 2.4 and 2.6) were calculated as described previously for phase tuning curves except after replacing the neural response with the kinematic variable. We used 30 bins to estimate probability distributions of ω, a, ζ, θ_{amp}, $\theta_{setpoint}$ and f_{whisk} (Figure 2.6A).

Chapter 3: Encoding of Whisking Kinematics by Facial Mechanoreceptors[3]

Proprioception is the sense of where the body or its parts are in space. To interpret touch, it is critical that the brain also knows where in space the touched body part was at the time of contact. Thus, touch and proprioception are intimately linked during normal sensory-motor function. Touch begins with the activation of low-threshold mechanoreceptors (LTMRs) in the skin. Information about body position can come from efference copy signals that report the motor commands ultimately used to control muscles. However, the nervous system contains dedicated mechanoreceptive proprioceptor endings to provide feedback about actual, rather than intended, position. Classical proprioceptors include muscle spindle and Golgi tendon organ afferents.

Many rodents use rapid motions of their mystacial vibrissae (whiskers) to explore the tactile world (Carvell and Simons, 1990; Welker et al., 1964b; Wineski, 1983). Curiously, the muscles controlling these "whisking" motions, as with other facial muscles, lack classical proprioceptor endings (Moore et al., 2015). Therefore, feedback about whisker position must occur via self-motion-triggered ("reafferent") activity of peripheral mechanoreceptors other than classical muscle proprioceptors, such as the cutaneous LTMRs responsible for sensing touch. Neurons throughout the whisker somatosensory system respond to whisker self-motion in a manner that depends on the relative position of the whisker within the current whisk cycle, or whisk "phase" (Campagner et al., 2016; Crochet and Petersen, 2006; Curtis and Kleinfeld, 2009; Fee et al., 1997; Hires et al., 2015; Khatri et al., 2009; Leiser and Moxon, 2007; Moore et al., 2015; Severson et al., 2017; Wallach et al., 2016; Yu

---

[3] Sections of this chapter are adapted from Severson et al., 2018.

et al., 2006; Yu et al., 2016). Whisk phase is thought to be a key coordinate system for whisker-based sensation (Curtis and Kleinfeld, 2009; Kleinfeld and Deschenes, 2011; Szwed et al., 2003).

LTMRs that innervate the whisker follicles encode whisk phase and other aspects of whisker motion and touch during active sensing (Bush et al., 2016; Campagner et al., 2016; Khatri et al., 2009; Leiser and Moxon, 2007; Severson et al., 2017; Szwed et al., 2003; Szwed et al., 2006; Wallach et al., 2016). These LTMRs include Merkel-type endings, which are slowly adapting and thought to play a major role in perception of object shape and texture. Individual Merkel and unidentified slowly adapting whisker afferents respond both to touch and to self-motion (Severson et al., 2017). Self-motion (reafferent) responses arise from diverse mechanical sensitivities of whisker afferents (Campagner et al., 2016; Severson et al., 2017; Wallach et al., 2016), and may be used by the brain for whisker proprioception (for behavioral studies addressing whisker proprioception, see: Knutsen et al., 2006; Mehta et al., 2007; O'Connor et al., 2013). Neurons in the brainstem (one synapse downstream from mechanoreceptors) with tactile receptive fields on parts of the face other than whiskers can also respond during whisking in a manner that reports whisk phase (Moore et al., 2015). This suggests that mechanoreceptors innervating facial parts other than whiskers could encode whisker motion, including whisk phase, but this has not been tested. What is the full set of possible mechanoreceptor sources of information that could tell the mouse brain about whisker motion, and how do they compare to one another?

Here, we addressed this question by recording whisker motion and electrophysiological responses from primary mechanoreceptor afferents innervating several distinct structures on the face, including regions of hairy skin, vibrissae other than the mystacial whiskers, and jaw muscles (Figure 3.1A). We compared the encoding of whisker motion among these different populations of mechanoreceptors to that of whisker mechanoreceptors. We find that a subset of hairy skin mechanoreceptors encodes whisker motion at levels comparable to whisker mechanoreceptors.

However, as a population, whisker and other non-whisker vibrissae mechanoreceptors encode the most information about whisker motion. Our results suggest that information about whisking arises from multiple sensory sources, providing the brain with a robust basis for facial proprioception.

Self-motion encoding by whisker mechanoreceptors

We obtained electrophysiological and high-speed video recordings (500 Hz) from head-fixed mice as they ran on a treadmill and whisked freely in air (Figure 3.1B; Supplemental Video 1). From these video frames, we measured several kinematic variables derived from the whisker's angular position (θ) (Figure 3.1C). During whisking θ can be decomposed into three quantities that the brain appears to process differently (Hill et al., 2011): midpoint (θ_{mid}), amplitude (θ_{amp}), and phase (Φ) (Figure 3.1D; Materials and Methods). Whisker primary motor cortex (wM1) robustly encodes θ_{mid} and θ_{amp} (Hill et al., 2011; Huber et al., 2012), and sends this information along cortico-cortical pathways to primary somatosensory cortex (wS1) (Petreanu et al., 2012). This suggests that the brain could use efference copy to keep track of θ_{mid} and θ_{amp}. A small fraction of neurons in wM1 does encode Φ, including after transection of the infraorbital nerve (Hill et al., 2011) that carries sensory information from the whisker pad (Dorfl, 1985). However, the encoding of Φ by neurons across all levels of the ascending somatosensory system, as well as the elimination of phase signals in wS1 after peripheral block of whisking (Fee et al., 1997), indicate a major reafferent contribution to phase coding in the brain. For this reason, and because whisk phase is thought to be a key coordinate scheme for whisker sensation, we focused analysis of the encoding of whisk phase. However, we also analyzed encoding of θ_{mid} and θ_{amp} to determine whether they too could be directly sensed, and encoding of whisker angle (θ), angular velocity (θ'), and angular acceleration (θ''), as these quantities give insight into the mechanical basis of what makes mechanoreceptors spike (Severson et al., 2017; Wallach et al., 2016).

We aligned these kinematic quantities with simultaneously recorded spikes from different classes of facial mechanoreceptor afferents (Figure 3.1E).

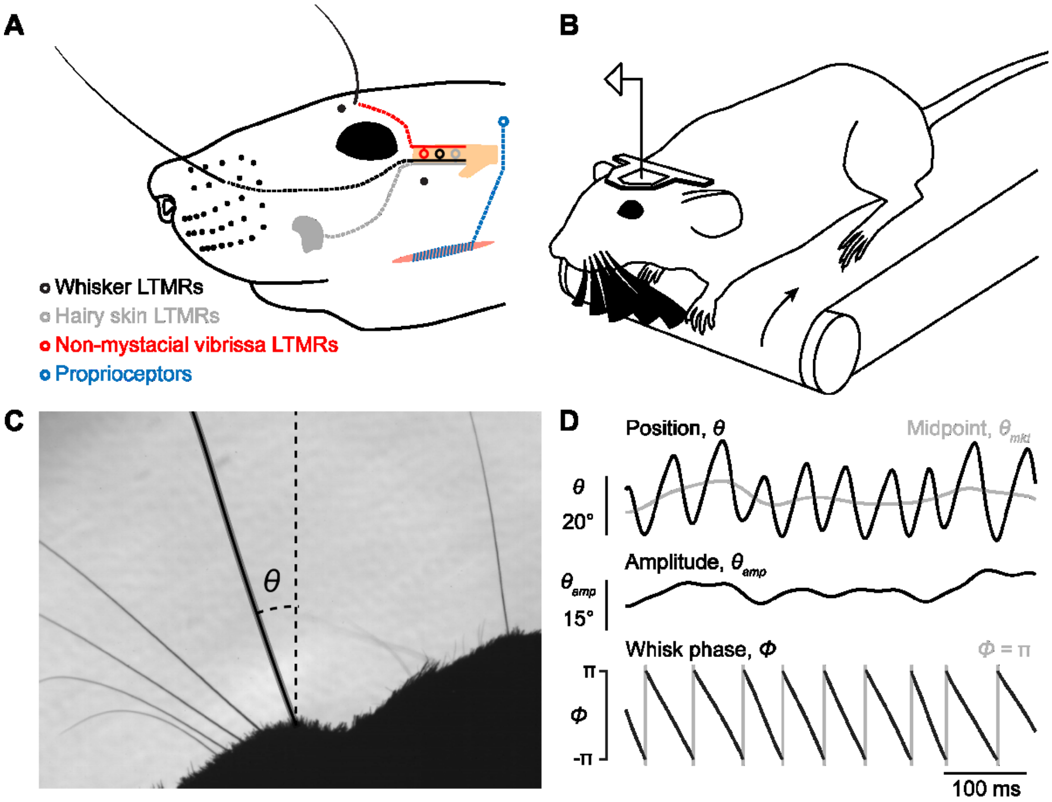

E

Afferent group	Recording location	Units recorded	Units whisking-sensitive
Whisker	TG	67	42
Hairy skin	TG	85	58
Non-mystacial vibrissa	TG	35	19
Proprioceptors	MeV	43	33

Figure 3.1 Recording whisking and spikes from mechanosensory afferents.

(**A**) Schematic illustrating different types of afferents (open circles with dotted lines) recorded in these experiments, grouped by type of receptive field. These include four populations: trigeminal ganglion (TG, yellow) low threshold mechanoreceptors (LTMRs) with receptive fields localized to either a whisker follicle (black), hairy skin (gray; patch depicts receptive field), or a non-mystacial vibrissa (red), or trigeminal mesencephalic nucleus (MeV) proprioceptors innervating facial muscles (blue). (**B**) Schematic of experimental setup. A head-fixed mouse ran on a treadmill and whisked in air. Single units were recorded simultaneously with high-speed (500 Hz) video of the whiskers. (**C**) Example video frame, capturing the silhouette of the whiskers and profile of the mouse face. To track whisking kinematics, the angle (θ) of a whisker (black trace) relative to the mediolateral axis (dotted line) was measured. (**D**) Top, example one second trace of whisker position (θ, black) and its midpoint position (θ_{mid}, gray). Middle, whisk amplitude (θ_{amp}) is the half-width, in degrees, of the whisk cycle. Lower bound of scale bar indicates 0°. Bottom, whisk phase (Φ, black), computed for the same trace, is the relative position of the whisker within a whisk cycle. Times when the whisker is in its fully retracted position ($\Phi = \pi$) are indicated by gray lines. (**E**) Table indicating electrode location (either TG or MeV), number of recorded units, and number of whisking-sensitive units (non-overlapping 95% CI for mean spike rate during whisking vs non-whisking and >1 Hz mean spike rate during whisking) recorded for each mechanoreceptor group.

We first analyzed units in the trigeminal ganglion (TG) with touch receptive fields confined to single whiskers (Figure 3.2A, n = 67). Many of these afferents were direction-selective, preferring manual deflections in either the protraction or retraction direction (not shown). A subset of these whisker afferents was more active during whisking (n = 42 “whisking-sensitive” units, defined in Glossary) and strongly modulated by phase, preferring to fire at a particular phase of the whisk cycle (Figure 3.2B,C). This sharp phase tuning largely reflects sensitivity to inertial stresses (Severson et al., 2017). We used information theory analyses to quantify how well spiking of single mechanoreceptors encoded phase and other variables related to whisker kinematics. Specifically, we calculated the mutual information (MI; Cover and Thomas, 2006), a measure of association between two random variables derived from their joint probability distribution (Figure 3.2D), between (1) spike counts obtained during 2 ms video frames, and (2) binned values (Materials and Methods) of kinematic variables extracted from the video frames, including θ, θ', θ'', θ_{amp}, θ_{mid}, and Φ. Mutual information between phase and spike count for whisker afferents, expressed as a rate via multiplying by the 500 Hz sampling frequency, was 9.1 ± 23.8 bits/s (median ± interquartile range [IQR]; n = 42 whisking-sensitive units). To determine which kinematic variable best accounted for the spiking of whisker afferents, we calculated a "normalized mutual information" by dividing MI by the spike count entropy (Jamali et al., 2016). This quantity gives the fraction of spike count uncertainty accounted for by a given kinematic variable. Whisker afferent spike counts were better explained by phase (Figure 3.2E; normalized MI = 0.096 ± 0.121; median ± IQR) than by θ (0.034 ± 0.064), θ' (0.046 ± 0.086), θ'' (0.030 ± 0.076), θ_{amp} (0.012 ± 0.024), or θ_{mid} (0.0089 ± 0.013; $p < 0.0031$ for all 5 comparisons, two-tailed K-S tests).

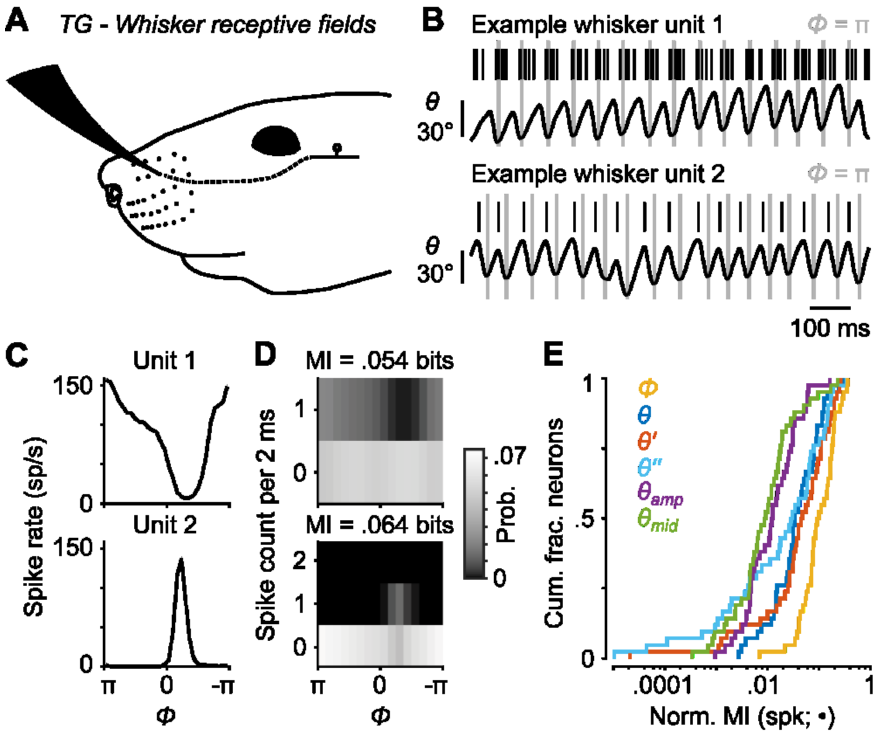

Figure 3.2 Self-motion responses from mechanoreceptors innervating whisker follicles.

(**A**) Schematic illustrating a unit with receptive field mapped to a whisker follicle (e.g. whisker B2; n = 67 total, 42 whisking-sensitive). (**B**) Spike times (black ticks) for two example whisker afferent units, each aligned with whisker position traces in black (gray lines: fully retracted positions). Unit 1 (top) responded during protracting phases, and unit 2 (bottom) responded during retracting phases. (**C**) Phase tuning curves (mean ± SEM; SEM here and in some subsequent panels narrower than line width) for unit 1 (top) and unit 2 (bottom). (**D**) Joint probability distributions for spike count and whisk phase (Φ), obtained from 2 ms periods corresponding to individual video frames, for unit 1 (top) and unit 2 (bottom). Mutual information (MI) between spike count and phase for each unit is shown at the top of each panel. Per 2 ms period, unit 1 spiked up to once and unit 2 up to twice. (**E**) Cumulative distributions of normalized mutual information values for all whisking-sensitive whisker mechanoreceptors (n = 42), measured between spike count and each kinematic quantity (•): phase (Φ, yellow), position (θ, dark blue), angular velocity (θ', red), angular acceleration (θ'', light blue), whisking amplitude (θ_{amp}, purple), and whisking midpoint (θ_{mid}, green). A subset of whisker afferent recordings was previously reported (Severson et al., 2017) and are reanalyzed here (see Table 2 for details).

Whisker motion coding by mechanoreceptors innervating hairy skin

While whisker mechanoreceptors showed strong phase coding, our goal was to put this coding into context by comparing the information provided by these whisker afferents to that of any other types of mechanoreceptor we could find that responded during whisking in air. We began by recording from TG units with touch receptive fields on hairy skin (n = 85) rather than a vibrissa (Figure 3.3A). Afferents responded to manual deflections of all small hairs or a small number of guard hairs within the mapped receptive field, were rapidly adapting, and responded to touch in all directions (not shown). Remarkably, activity of a large number of facial hairy skin afferents was modulated during whisking in air (Figure 3.3B, 58 of 85 were whisking-sensitive). Consistent with the lack of direction-selectivity, many facial hairy skin afferents fired at multiple phases (e.g. both protraction and retraction phases) of the whisk cycle (Figure 3.3C). Phase coding by hairy skin afferents varied by receptive field location, such that units with receptive fields closer to the whisker pad tended to encode phase more strongly than those distant from the pad (Figure 3.3D; overall MI rate = 1.3 ± 4.5 bits/s; median ± IQR).

We next grouped the hairy skin receptive fields into six different "zones" of the face (Figure 3.4), including the pad, cheek, snout, eye, lip, and jaw. Units with receptive fields on the whisker pad ($n = 14$) were particularly modulated by phase (13 of 14 were whisking-sensitive). We found several receptive fields comprised of small hairs surrounding whisker follicles, in between whisker arcs or rows, or flanking the outer whiskers. Receptive fields on the pad were smaller in area than other regions of the face (Figure 3.3D). Pad hairy skin afferent encoding of phase (MI rate = 9.26 ± 8.53 bits/s, median ± IQR) was comparable to whisker afferents and significantly higher than afferents innervating hairy skin on the cheek (0.73 ± 2.10 bits/s), eye (1.11 ± 3.57 bits/s), lip (0.75 ± 1.76 bits/s), snout (1.63 ± 1.23 bits/s), and jaw (0.08 ± 0.09 bits/s; Figure 3.3E, $p < 0.032$ for all 5 two-tailed K-S tests). Across all facial hairy skin afferents, normalized MI (Figure 3.3F) was significantly higher for phase (0.0165 ± 0.0348) compared to θ' (0.0062 ± 0.0098), θ'' (0.0056 ± 0.0098), θ_{amp} (0.0085 ± 0.012), and θ_{mid} (0.0094 ± 0.011; $p<0.003$ for all 4 two-tailed K-S tests), but similar to θ (0.014 ± 0.023; $p = 0.77$ two-tailed K-S test).

Video capturing facial motion and whisker position suggested that widespread patterns of skin strain likely occur in a manner correlated with whisking, with stronger correlations between skin and whisker displacements occurring for facial regions on or near the whisker pad (Figure 3.4). In addition to skin movements, we observed that the vibrissae above the eye whisk in phase with the whiskers. We next focused our attention on vibrissae outside of the whisker pad.

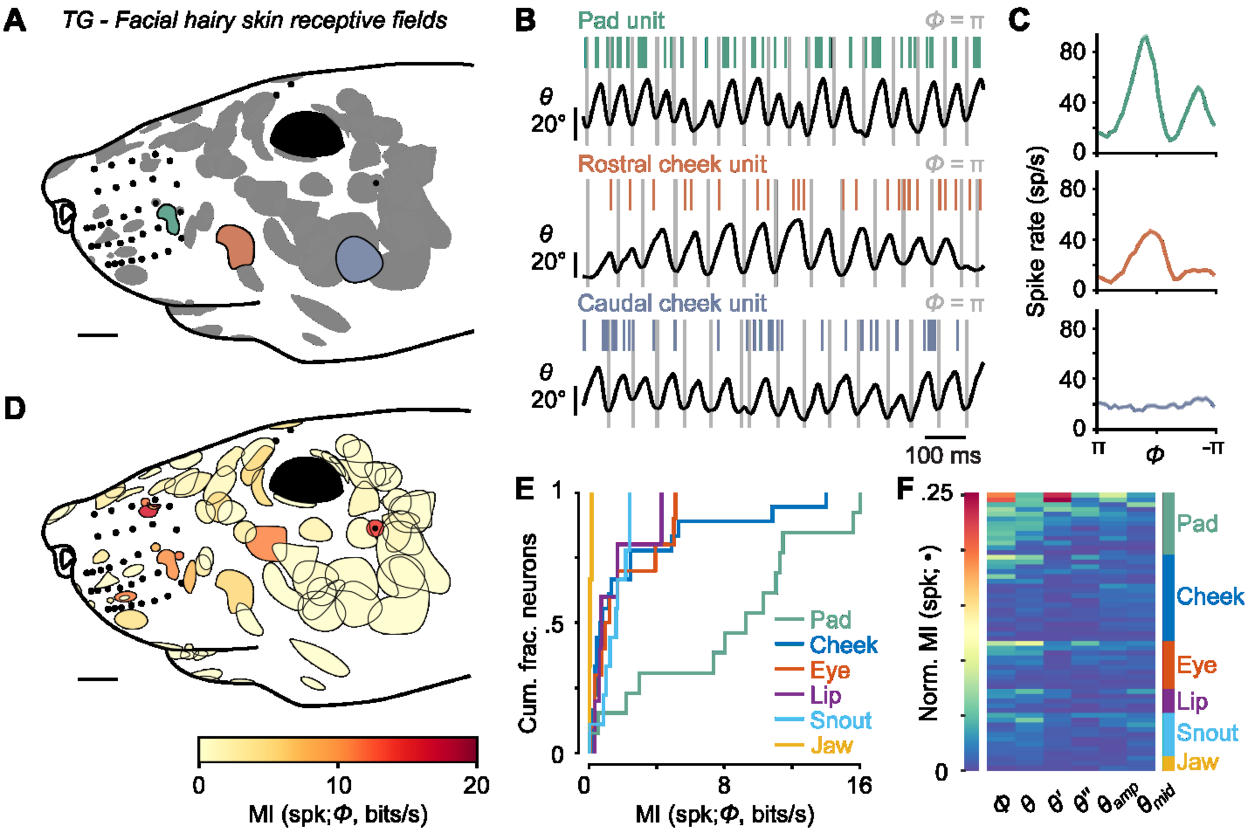

Figure 3.3 Self-motion responses from mechanoreceptors innervating facial hairy skin.

(**A**) Receptive fields on facial hairy skin (n = 85). Approximate size, shape, and location of receptive fields (gray) were compiled onto a template image of a mouse face (scale bar: 2 mm). Colored receptive fields show examples from whisker pad (green), rostral cheek (orange), and caudal cheek (blue). Whisker follicles and non-mystacial vibrissae (filled black dots) are included as fiducial marks. (**B**) Example one second traces showing spike times (colored ticks) aligned with whisker position (black trace; gray lines: fully retracted positions), from recordings corresponding to the examples in (A). (**C**) Phase tuning curves (mean ± SEM) for example pad unit (green, top), rostral cheek unit (orange, middle), caudal cheek unit (blue, bottom). Example cheek units illustrate that units with similar mean spike rates during whisking can differ in their phase modulation. (**D**) Mutual information (MI; expressed as a rate by multiplying by the sampling frequency of 500 Hz; color scale) between spike count and phase overlaid on outlines of receptive fields (scale bar: 2 mm). Many but not all receptive fields with large MI values were located near whiskers. (**E**) Cumulative distributions of MI rate between spike count and phase for whisking-sensitive units with receptive fields in each region of the face, including whisker pad (green, n = 13), cheek (dark blue, n = 18), eye (red, n = 10), lip (purple, n = 5), snout (light blue, n = 9), and jaw (yellow, n = 3). (**F**) Heatmap of normalized MI values for all whisking-sensitive facial hairy skin units (n = 58), measured between spike count and each kinematic quantity (•, columns): phase (Φ), position (θ), angular velocity (θ'), angular acceleration (θ''), amplitude (θ_{amp}), and midpoint (θ_{mid}). Units (rows) are sorted by receptive field location (labeled at right) and within each face region by increasing normalized MI averaged across the kinematic quantities.

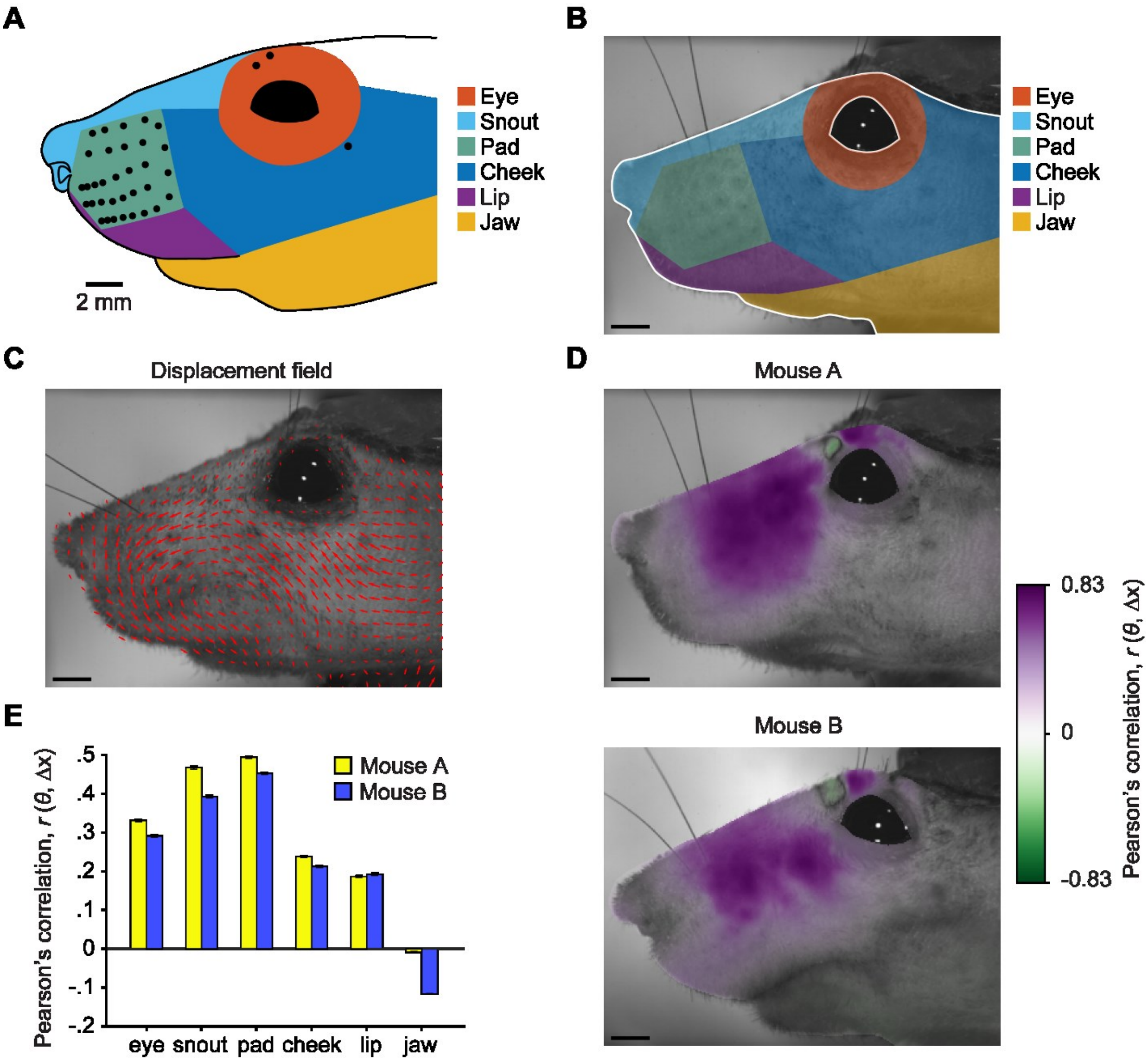

Figure 3.4 Widespread facial movement correlated with whisker motion.

(**A**) Six facial regions on template mouse face were used for categorizing afferent receptive fields. Zones were drawn based on fiducial marks, including the mystacial whiskers (filled circles). Locations of non-mystacial vibrissa follicles (open circles) are also indicated. Receptive fields were scaled to the template image. (**B**) "Fixed" template image for image registration method of tracking facial motion. Overlaid are facial regions drawn using image fiducial marks. Pixels outside the edge of the face and within the eye, outlined in white, were effectively excluded from image registration by setting their values to zero. (**C**) Example "moving" frame overlaid with a subset of the estimated x- and y-displacements, plotted as vectors (red arrows), that would align it to the fixed template image. (**D**) Template images from each of two mice overlaid with color scale showing Pearson's correlation coefficients (*r*) between the time series of each pixel's x-displacement (Δx) and the A1 whisker position (θ). (**E**) Pearson's *r* values averaged (± SEM) across all pixels within each facial region, separately for two mice. (B-D) Scale bars: 2 mm.

Non-mystacial vibrissa movement correlates with whisking

Mice have several vibrissae outside of the whisker pad, including two supraorbital vibrissae above the eye, one genal vibrissa on the cheek (Danforth, 1925), and several microvibrissae on the upper lip (Figure 3.5A; Brecht et al., 1997). These sinus follicle structures are highly conserved within strains of mice (Dun and Fraser, 1958) and are present in many other mammals (Danforth, 1925; Wineski, 1983). Surprisingly, in our high-speed videos we noticed periodic movement of supraorbital vibrissae apparently locked to whisking. To quantify these movements, we simultaneously tracked non-mystacial vibrissae and whiskers (i.e. mystacial vibrissae) using high-speed videography. Supraorbital vibrissae (Figure 3.5B-D) and the genal vibrissa (Figure 3.5B-D) moved in phase with the whiskers. We observed some instances of "missed" whisk cycles, in which the whisker moved, but the supraorbital or genal vibrissae remained still (Figure 3.6). Microvibrissa barely moved (Figure 3.5B-D). Small translations we observed could be due to passive pulling of lip tissue during whisking, rather than active rotation of the microvibrissa follicle.

We computed cross-correlations to quantify the phase lag and degree of correlation between whiskers and the supraorbital and genal vibrissae, and microvibrissae (Figure 3.5E). We first analyzed pairs of whiskers to set an "upper bound" on correlations, as whiskers in the same row have highly correlated movements (Wallach et al., 2016). Adjacent whiskers correlated almost perfectly (Pearson's correlation coefficient, $r = 0.98 \pm 0.03$, n = 14 recordings from 11 mice) with no phase lag (0.00 ± 0.03 radians). These strong correlations among whiskers also validated the use of adjacent or nearby whiskers—chosen for their convenience in obtaining high-speed videos of both whiskers and other vibrissae—when quantifying correlations between whiskers and other vibrissae.

Supraorbital vibrissae movements correlated strongly with whisker movements ($r = 0.78 \pm 0.07$, mean ± SD, n = 6 recordings from 6 mice), but with a short delay (Figure 3.5B,E; $\Phi_{lag} = 0.27 \pm 0.05$ radians, mean ± SD; p = 4.9e-12, one-tailed t-test). Whisking amplitude (θ_{amp}) was smaller for supraorbital vibrissae (4.7 ± 2.1°, mean ± SEM) compared to whiskers (Figure 3.5F; 12.5 ± 2.5°, mean ± SEM; p = 1.1e-6, one-tailed t-test).

Genal vibrissa motion also correlated strongly with that of the whiskers ($r = 0.83 \pm 0.08$, mean ± SD), but with a longer phase delay (Figure 3.5C,E; $\Phi_{lag} = 0.61 \pm 0.18$ radians, mean ± SD; p = 9.9e-11, one-tailed t-test). Whisking amplitude for genal vibrissae was also smaller (2.2 ± 1.4°, mean ± SEM) compared to the tracked whiskers (Figure 3.5F; p = 6.9e-9, one-tailed t-test) and supraorbital vibrissae (p = 0.016, one-tailed t-test).

Microvibrissae motion correlated with whisker motion less well ($r = 0.27 \pm 0.29$, mean ± SD, n = 3 recordings from 3 mice) with a short delay ($\Phi_{lag} = 0.44 \pm 0.11$ radians, mean ± SD; p = 4.8e-10, one-tailed t-test; Figure 3.5D,E). Whisking amplitude for microvibrissae (Figure 3.5F, 0.84 ± 0.23°, mean ± SEM) was smaller than for whiskers (p = 3.5e-7, one-tailed t-test) and supraorbital vibrissae (p = 0.0086, one-tailed t-test). With smaller amplitude movements and smaller sizes, the mechanical stresses generated at the base of microvibrissae during whisking are likely smaller than those at the bases of other vibrissae types.

Non-mystacial vibrissa mechanoreceptors encode information about whisking

The motion of non-mystacial vibrissae was correlated with whisker motion during whisking. Therefore mechanoreceptors with receptive fields on these vibrissae could show activity patterns that encode whisker self-motion. To test this possibility, we recorded from TG units with touch receptive fields on non-mystacial vibrissae. We found units, some of which were active during whisking, on supraorbital vibrissae (8 of 17 whisking-sensitive), genal vibrissae (3 of 8 whisking-sensitive), and microvibrissae (8 of 10 whisking-sensitive). Non-mystacial vibrissa afferent spiking aligned with whisk phase (Figure 3.5G). Similar to whisker afferents, we observed examples of sharp phase tuning (Figure 3.5H).

Supraorbital afferents encoded similar amounts of information about phase (MI rate = 16.2 ± 14.9 bits/s, median ± IQR) as genal afferents (5.2 ± 8.6 bits/s, median ± IQR; $p = 0.23$, two-tailed K-S test), and more than microvibrissa afferents (Figure 3.5I; 0.74 ± 1.60 bits/s, median ± IQR; $p = 0.0014$, two-tailed K-S test). The spike counts of non-mystacial vibrissa afferents overall were better explained by Φ (Figure 3.5J; normalized MI = 0.062 ± 0.17, median ± IQR) and θ (0.047 ± 0.042) compared to θ_{amp} (0.019 ± 0.034), and θ_{mid} (0.021 ± 0.033; $p < 0.049$ for all 4 two-tailed K-S tests).

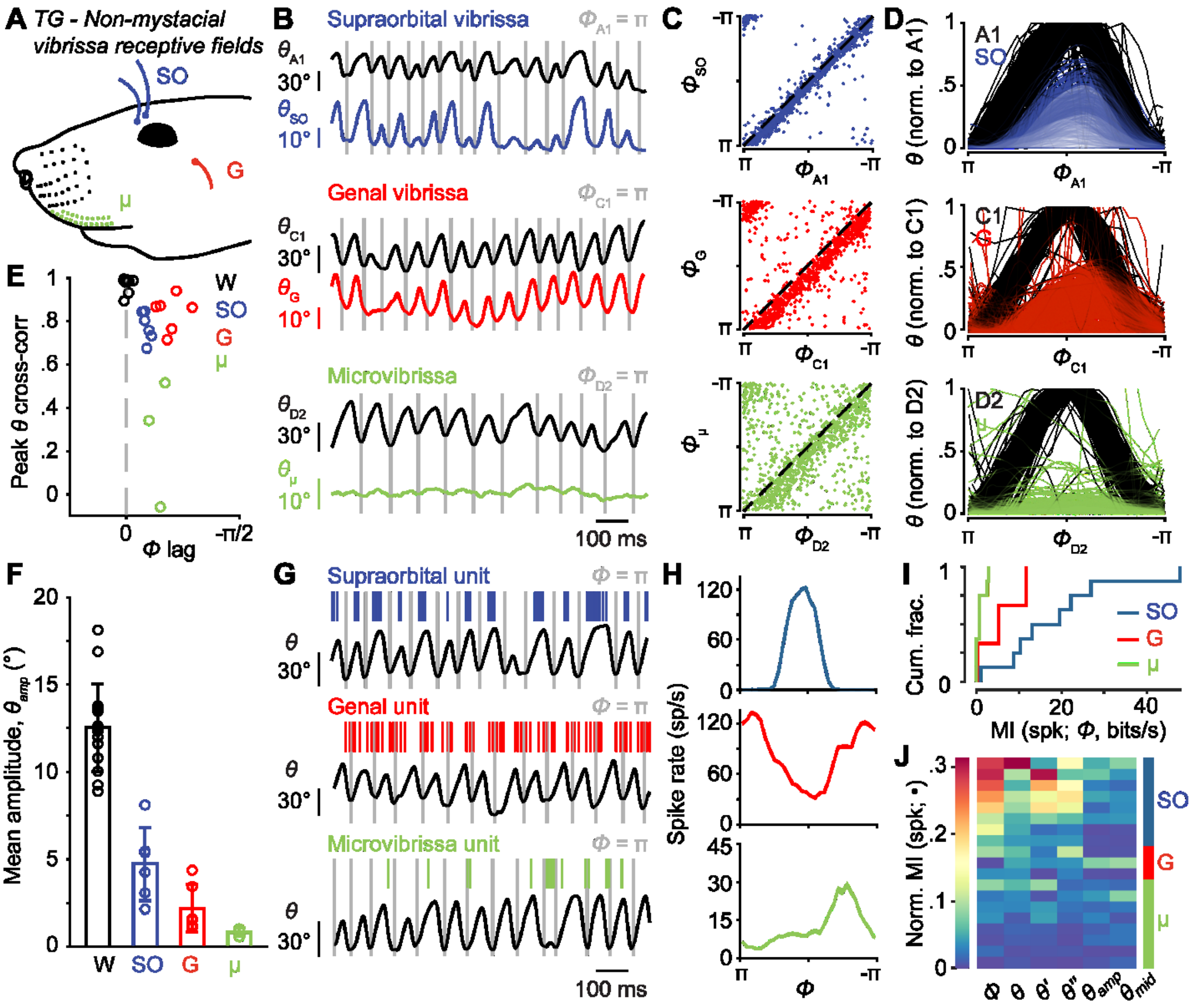

Figure 3.5 Non-mystacial vibrissae move in phase with whiskers, and their mechanoreceptors encode motion.

(**A**) Schematic of non-mystacial vibrissae included in these experiments: supraorbital (SO, blue) above the eye, genal (G, red) on the cheek, and microvibrissae (μ, green) on the upper lip. (**B**) Correlated motion between whiskers and non-mystacial vibrissae. Example one second trace of whisker (black) and vibrissa angle (top, supraorbital, blue; middle, genal, red; bottom, microvibrissa, green) tracked simultaneously (gray lines: fully retracted whisker positions). (**C**) Scatter plot of whisk phase for whisker vs non-mystacial vibrissae (n = 1000 randomly chosen frames; top, SO, blue; middle, G, red;

bottom, µ, green; dashed black lines: unity). (**D**) Trajectories of whisker and non-mystacial vibrissa angles through each whisk cycle, normalized to the whisker angle (n = 500 randomly chosen cycles; top, A1 and SO angle; middle, C1 and G angle; bottom, D2 and µ angle). (**E**) Peak cross-correlation (Pearson's r) and phase lag (open circles) for θ of tracked whisker and either adjacent whisker (W, gray; n = 14 whisker pairs from 12 mice), supraorbital (SO, blue; n = 6 recordings from 6 mice), genal (G, red; n = 6 recordings from 6 mice), or microvibrissa (µ, green; n = 3 recordings from 3 mice). (**F**) Mean whisk amplitude for whisker (W, gray), supraorbital (SO, blue), genal (G, red), or microvibrissa (µ, green). Bars indicate mean ± SD across recordings. (**G**) Example one second periods with spike times from supraorbital unit (top, blue ticks), genal unit (middle, red ticks), and microvibrissa unit (bottom, green ticks) aligned with position of the tracked whisker (θ, black trace; gray lines: fully retracted whisker positions). (**H**) Phase tuning curves (mean ± SEM) for the same examples in (G): top, SO, blue; middle, G, red; bottom, µ, green. (**I**) Cumulative distributions of mutual information rate between spike count and phase of whisking-sensitive units with receptive fields on non-mystacial vibrissae, including SO (blue, n = 8), G (red, n = 3), and µ (green, n = 8). (**J**) Heatmap of normalized mutual information for all whisking-sensitive non-mystacial vibrissa units (n = 19), measured between spike count and each kinematic quantity (•, columns): phase (Φ), position (θ), angular velocity (θ'), angular acceleration (θ''), amplitude (θ_{amp}), and midpoint (θ_{mid}). Units (rows) are sorted by receptive field location (labeled at right) and within each non-mystacial whisker by increasing normalized MI averaged across the kinematic quantities.

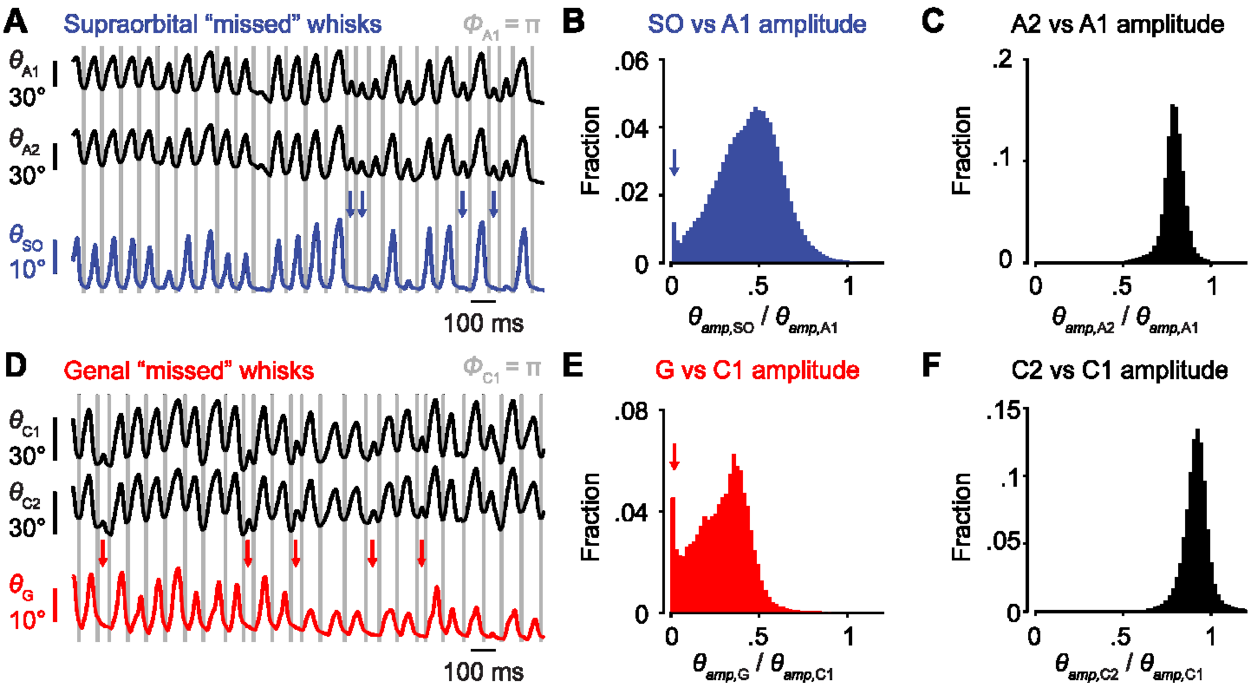

Figure 3.6 Example "missed" whisks by non-mystacial vibrissae.

(**A**) Example traces of simultaneously recorded A1 whisker position (θ_{A1}, top black trace), A2 whisker position (θ_{A2}, bottom black trace) and supraorbital vibrissa position (θ_{SO}, blue; gray lines: fully retracted phase of A1). Whisks by A1 that we not matched by whisks of SO vibrissae (missed whisks) are marked by blue arrows. (**B**) Histogram of ratio of supraorbital vibrissa amplitude ($\theta_{amp,SO}$) over A1 whisker amplitude ($\theta_{amp,A1}$) for whisking periods (330,085 frames) in the example recording in (A). Ratios above 1.2 are not shown on plot for clarity (0.09% of frames). The peak with ratio near zero, indicated by a blue arrow, indicates a substantial fraction of missed whisks in this example recording. (**C**) Same as (B) but for A2 vs A1 whiskers. There is no histogram peak indicative of missed whisks (0.16% of values are above the axis limit of 1.2). (**D**) Example traces of θ_{C1} and θ_{C2} (black traces) and θ_G (red; gray lines: fully retracted phase of C1). Missed whisks by the genal vibrissa are marked by red arrows. (**E**) Histogram of ratio of genal vibrissa amplitude ($\theta_{amp,G}$) versus C1 whisker amplitude ($\theta_{amp,C1}$) for whisking periods (96,429 frames) in the example recording in (C). Ratios above 1.2 not shown (0.36% of frames). Missed whisks with amplitude ratio near zero are indicated by the red arrow. (**F**)

Same as (E) but for C2 vs C1 whiskers. There is no histogram peak indicative of missed whisks (0.75% of values are above the axis limit of 1.2).

Information encoded by jaw proprioceptors

The trigeminal mesencephalic nucleus (MeV) resides in the brainstem and contains mechanoreceptor neurons that innervate the masseter muscles involved in mastication. Recently, it has been suggested that MeV neurons respond to aspects of whisker motion (Mameli et al., 2017; Mameli et al., 2010; Mameli et al., 2014), which necessitates their inclusion in a full account of possible sources of peripheral information about whisker motion available to the brain (Bosman et al., 2011). We thus recorded the activity of single neurons using 32-channel tetrode microdrives implanted in MeV (Figure 3.7A).

As with TG recordings, head-fixed mice were placed on a treadmill to elicit running and whisking. Mice also licked at a lickport for water rewards. We used this preparation to identify jaw muscle proprioceptors, as their activity was strongly modulated by the licking associated with reward consumption (Figure 3.7B,C). For analysis we considered both these putative jaw muscle proprioceptors ($n = 23$ units), plus units that were recorded on the same tetrode as a putative proprioceptor ($n = 20$ units) and therefore also presumably in MeV. We did not observe obvious phasic modulation of MeV activity during whisking (Figure 3.7B; periods of licking excluded from this analysis). MeV units ($n = 33$ whisking-sensitive) were not tuned to whisk phase (Figure 3.7D) and thus did not encode much information about phase (0.04 ± 0.04 bits/s, median ± IQR).

However, we did observe a correlation between MeV activity and whisking midpoint (Figure 3.7D,E). Several units increased or decreased spiking with increasing θ_{mid}. In addition, the kinematic variables that associated best with MeV spike counts were midpoint, amplitude, and position (Figure 3.7F). However, MI values between spike count and these quantities were low (e.g. θ_{mid}: 0.17 ± 0.38

bits/s, median ± IQR). Thus, MeV activity is not correlated with whisk phase and appears only weakly correlated with whisking midpoint. We speculate that this weak correlation may be explained by slight changes in jaw position associated with whisking around more or less protracted midpoints.

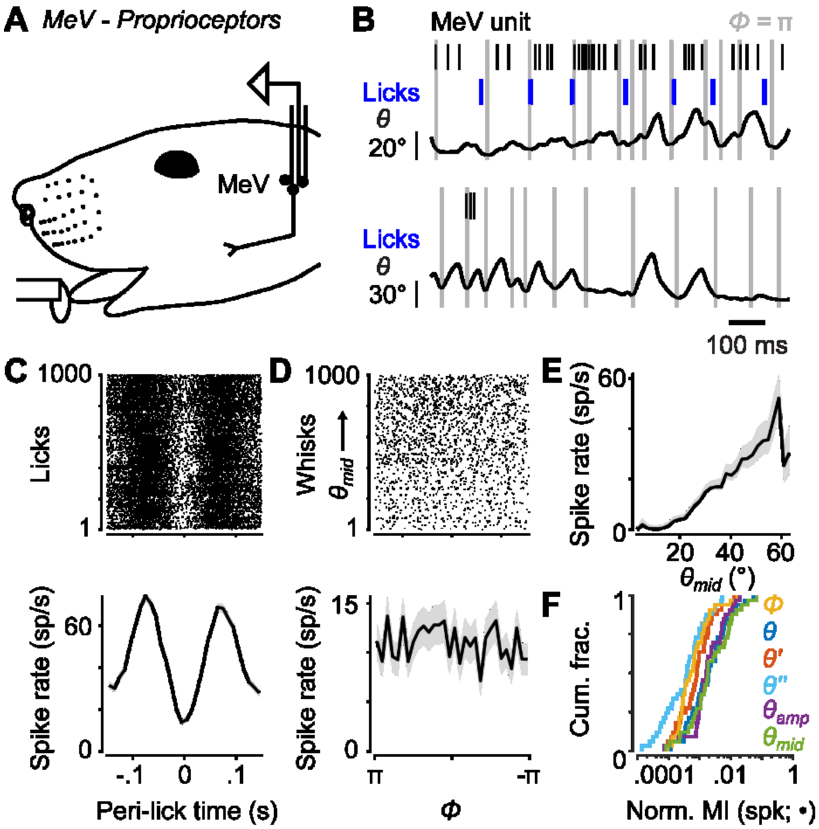

Figure 3.7 Responses of proprioceptors in the trigeminal mesencephalic nucleus during licking and whisking.

(**A**) Schematic of trigeminal mesencephalic nucleus (MeV) electrophysiological and behavioral recordings. Microelectrode drives were implanted into MeV. Putative MeV jaw proprioceptors were identified based on responses to passive jaw stretch and to active jaw movements occurring while licking for water reward. (**B**) Example one second period with MeV unit spike times (black ticks) and lick times (blue ticks) aligned with position (black trace) of the tracked whisker (gray lines: fully retracted positions). (**C**) Top, spike raster aligned to lick times (n = 1000 randomly chosen licks) for example unit in (B). Bottom, peri-event time histogram aligned to lick times (mean ± SEM) for all licks. (**D**) Top, spike raster aligned to whisk cycles (n = 1000 randomly chosen whisks) for unit in (B). Bottom, peri-event time histogram aligned to whisk phase (mean ± SEM) for all whisk cycles. Whisks are ordered by increasing mean θ_{mid}. (**E**) Midpoint (θ_{mid}) tuning curve (mean ± SEM) for unit in (B). (**F**) Cumulative distributions of normalized mutual information for all whisking-sensitive MeV units (n = 33), measured between spike count and each kinematic quantity (•): phase (Φ, yellow), position (θ, dark blue), angular velocity (θ', red), angular acceleration (θ'', light blue), amplitude (θ_{amp}, purple), and midpoint (θ_{mid}, green).

Comparison of whisker motion coding across facial mechanoreceptor classes

So far, we have described how well whisker afferents and other types of facial mechanoreceptors encode whisk phase and other variables related to whisker motion. A major goal was to compare whisker self-motion coding by whisker afferents with that of other classes of afferents. We directly compared coding of whisk phase and midpoint, given the importance of these variables in describing whisking behavior and neural activity (Curtis and Kleinfeld, 2009; Hill et al., 2011; Kleinfeld and Deschenes, 2011; Severson et al., 2017; Wallach et al., 2016). Overall, as a population the non-mystacial vibrissae afferents best encoded θ_{mid} (Figure 3.8A; MI rate = 0.81 ± 1.80 bits/s, median ± IQR), with similar encoding by whisker afferents (0.68 ± 1.08 bits/s, median ± IQR; p = 0.28 two-tailed K-S test vs non-mystacial afferents) and facial hairy skin afferents (0.72 ± 1.16 bits/s, median ± IQR; p = 0.61 two-tailed K-S test). MeV spike counts encoded θ_{mid} less well than all other afferent classes (0.17 ± 0.38 bits/s, median ± IQR; $p < 6.7e-4$ for all three two-tailed K-S tests). Similarly, normalized mutual information values showed that θ_{mid} explained spike counts less well for MeV than for all other afferent classes (Figure 3.8B; MeV: 0.0019 ± 0.0077; whiskers: 0.0089 ± 0.0134; non-mystacial vibrissae: 0.021 ± 0.033; facial hairy skin: 0.0094 ± 0.0110; median ± IQR; $p < 6.2e-4$ for all three two-tailed K-S tests of MeV vs other afferents).

Phase was best encoded by whisker (Figure 3.8C; MI rate = 9.1 ± 23.8 bits/s, median ± IQR) and non-mystacial vibrissae afferents (2.9 ± 11.9 bits/s, median ± IQR; p = 0.15 two-tailed K-S test vs whisker) compared with facial hairy skin afferents (1.3 ± 4.5 bits/s, median ± IQR; p = 3.0e-5, two-tailed K-S test vs whisker) and MeV afferents (0.04 ± 0.04 bits/s, median ± IQR; p = 8.9e-16, two-tailed K-S test vs whisker). Similarly, normalized mutual information values showed that phase better explained the spike count of whisker afferents (Figure 3.8D; 0.096 ± 0.121, median ± IQR) compared with facial hairy skin (0.017 ± 0.035, median ± IQR; p = 1.0e-10, two-tailed K-S test), non-mystacial vibrissae (0.062 ± 0.166, median ± IQR; p = 0.02, two-tailed K-S test), and MeV afferents (6e-4 ± 10e-4, median ± IQR; p = 8.9e-17, two-tailed K-S test).

While whisker mechanoreceptors as a group were overall best at encoding phase, other mechanoreceptor populations included more or less informative subgroups. For a more stringent comparison, we considered the best encoding subgroup from each population: whisker pad mechanoreceptors within facial hairy skin, supraorbital vibrissa mechanoreceptors within non-mystacial vibrissae, and putative jaw muscle proprioceptors within MeV. Mutual information between phase and spike count was similar for whisker (Figure 3.8E; n = 42; 9.1 ± 23.8 bits/s), pad (n = 13; 9.3 ± 8.5 bits/s, median ± IQR), and supraorbital mechanoreceptors (n = 8; 16.2 ± 14.9 bits/s; p > 0.11 for all three two-tailed K-S tests), and negligible for jaw proprioceptors (n = 23; 0.04 ± 0.04 bits/s; p < 8.4e-6 for all three two-tailed K-S tests). Thus, while whisker mechanoreceptors as a group best encode whisk phase, mechanoreceptors with receptive fields on whisker pad hairy skin and on the supraorbital vibrissae also send to the brain a signal that encodes whisk phase (Figure 3.8F).

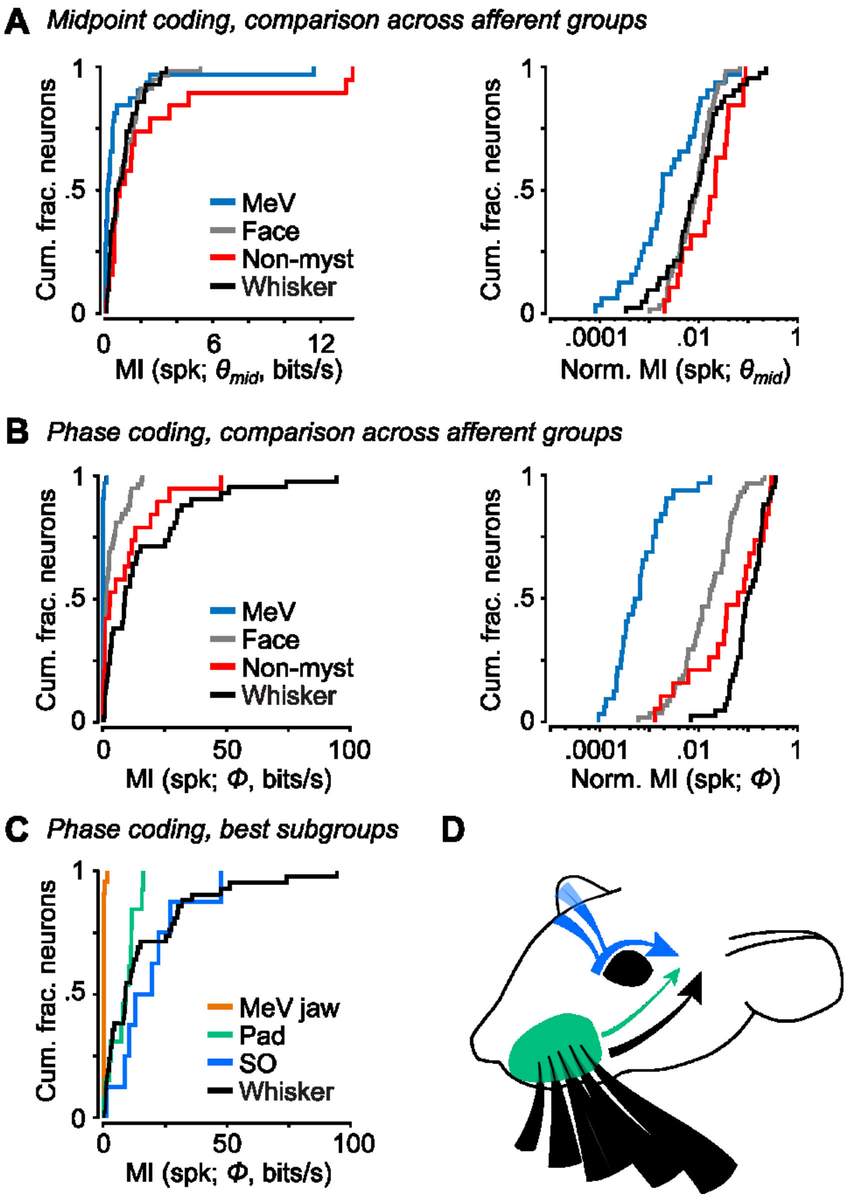

Figure 3.8 Coding of self-motion by diverse classes of facial mechanoreceptors.

(**A**) Summary cumulative distributions of mutual information rate between spike count and midpoint (θ_{mid}) for whisking-sensitive MeV (blue, n = 33), face (gray, n = 58), non-mystacial vibrissae (red, n = 19), and whisker units (black, n = 42). (**B**) Left, summary cumulative distributions of normalized mutual information between spike count and θ_{mid} for all whisking-sensitive MeV (blue), face (gray), non-mystacial vibrissae (red), and whisker units (black). Right, summary cumulative distributions of MI rate between spike count and phase (Φ) for whisking-sensitive units. (**C**) Left, summary cumulative distributions of normalized mutual information between spike count and phase for all whisking-sensitive MeV (blue), face (gray), non-mystacial vibrissae (red), and whisker units (black). Right, summary cumulative distributions of MI rate between spike count and phase for whisking-sensitive jaw proprioceptors (orange, n = 23), whisker pad afferents (green, n = 13), SO afferents (blue, n = 8), or whisker afferents (black, n = 42). Data for pad and SO afferents taken from Figures 3.3E and 3.5I, respectively. (**D**) Schematic depicting flow of information about whisking kinematics from various peripheral mechanoreceptors to the brain: whisker follicle afferents (black), supraorbital vibrissa afferents (blue), and whisker pad hairy skin afferents (green). (B,D) Data are taken from Figures 3.2, 3.3, 3.5, and 3.6 and plotted together for comparison.

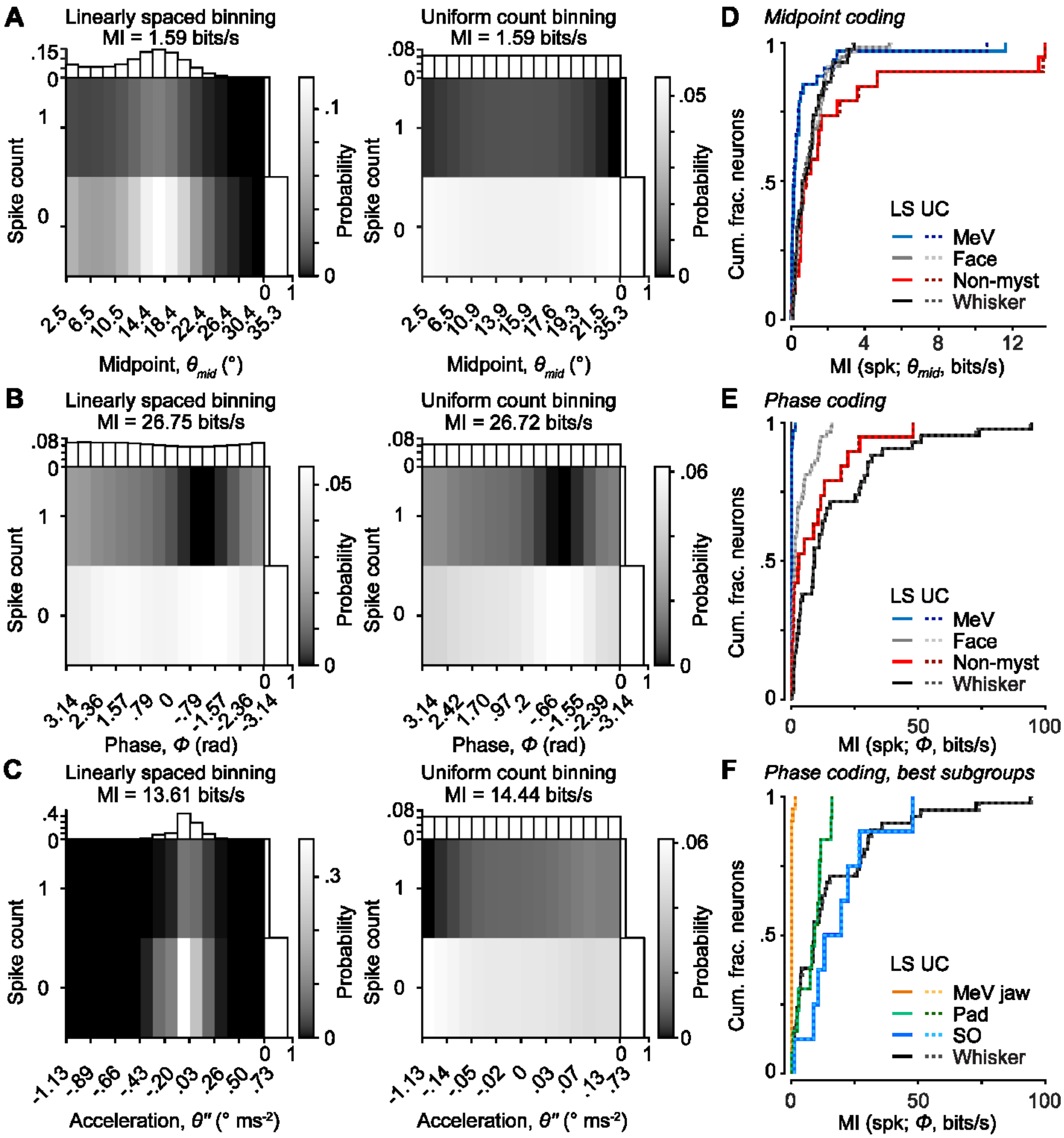

Figure 3.9 Alternative binning methods for mutual information calculation.

(**A**) Joint distribution for spike count and whisk midpoint (θ_{mid}) comparing linearly spaced (left, same calculation reported throughout paper) and uniform count (percentile) binning (right) of θ_{mid} for an example whisker afferent. Note that bin edges are not equally spaced for uniform count binning. Marginal distributions are plotted for θ_{mid} (top) and spike count (right). Mutual information (MI) rate values calculated using each method of binning are reported at the top. (**B**) Joint distribution for spike count and whisk phase (Φ) comparing linearly spaced binning (left) and uniform count binning (right) of Φ for the same example unit. Marginal distributions are plotted on top and to the right. Note that the distribution of phase is almost uniform, except fewer bins are observed during retraction phases due to rapid whisker retraction. MI rate values calculated using each method of binning are reported at top. (**C**) Joint distribution for spike count and angular acceleration (θ'') comparing linearly spaced (left) and uniform count binning (right) of θ'' for the same example unit. Marginal distributions are plotted on top and right. Note that distribution of θ'' has longer tails than θ_{mid} and Φ. MI rate values are reported at top. (**D**) Cumulative distributions of MI rate between spike count and θ_{mid}, calculated using linearly spaced ("LS", solid lines) or uniform count ("UC", dotted lines) binning for the different afferent groups (linearly spaced values are repeated from Figure 3.8A). (**E**) Cumulative distributions of MI rate between spike count and Φ, calculated using linearly spaced (solid lines) or uniform count (dotted lines) binning for the different afferent groups (linearly spaced values are repeated from Figure 3.8B). (**F**) Cumulative distributions of MI rate between spike count and Φ, calculated using linearly spaced (solid lines) or uniform count (dotted lines) binning for the best afferent subgroups (linearly spaced values are repeated from Figure 3.8C).

Discussion

Here we surveyed primary mechanoreceptive afferents that innervate multiple regions of the face to quantify correlations between spiking activity of these mechanoreceptors and whisker motion. Our specific goal was to provide a comprehensive account of the possible sources of reafferent information sent to the brain about whisking. This quantitative survey provides important context to interpret the encoding of whisker motion—and in particular, whisk phase—previously observed among whisker afferents (Campagner et al., 2016; Severson et al., 2017; Wallach et al., 2016), and more generally to investigate the hypothesis that facial proprioception relies on the reafferent activity of cutaneous LTMRs. We found that whisker afferents as a group encoded whisk phase best, together with supraorbital and genal vibrissae afferents. Thus, our results support the hypothesis that the strong phase coding observed in prior work with whisker afferents (Campagner et al., 2016; Severson et al., 2017; Wallach et al., 2016) could serve as a basis for whisker proprioception.

We found that a large number of mechanoreceptors with receptive fields on the hairy skin of the face responded in a phasic manner during whisking. While passive or active touch of the whiskers did not strongly activate facial hairy skin mechanoreceptors, passive stretch of the skin within or near their receptive fields was sufficient to cause spiking (not shown). This suggests that skin strain occurring within the receptive field, and in a pattern correlated with whisker motion, likely underlies the self-motion responses of these afferents. Activity of cutaneous afferents has also been reported during jaw movements in rabbits, with activity of non-direction selective, hairy skin afferents responding to self-motion in a manner proportional to movement speed (Appenteng et al., 1982). In humans, microneurography studies have reported activity in cutaneous afferents related to active movement of the face (Johansson et al., 1988), ankle (Aimonetti et al., 2007), knee (Edin, 2001), and finger (Edin and Abbs, 1991; Hulliger et al., 1979). Thus, "cutaneous" (reafferent) signals of potential use for proprioception occur across a wide variety of body parts and animal species.

Using high-speed videography, we found correlated motions of the non-mystacial vibrissae and the mystacial whiskers. In rodents, major aspects of the structure and innervation (Fundin et al., 1995; Wineski, 1985) of the supraorbital and genal vibrissae closely resemble those of mystacial vibrissae (Fundin et al., 1994). Motions of these non-mystacial vibrissae were assessed in the golden hamster, and they were found to be relatively immobile (Wineski, 1983). Here, we show that in mice, supraorbital and genal vibrissae are indeed mobile and whisk in phase with the whiskers. The observation of tight coupling of whisker and non-mystacial vibrissa movements adds to our understanding of the exquisitely coordinated orofacial motor actions in rodents (Kurnikova et al., 2017; Welker et al., 1964a) and suggests that their premotor circuits are linked (Deschenes et al., 2016; Kleinfeld et al., 2014; McElvain et al., 2018; Moore et al., 2013). Afferents with receptive fields on these structures, especially the supraorbital and genal vibrissae, displayed strong phase tuning and carried information about phase comparable to that of whisker afferents. While these afferents encode the phase of the whiskers in the whisk cycle, the supraorbital and genal vibrissae are unlikely to contact objects that are in reach of the whiskers. Thus, an interesting possibility is that afferents with these non-whisker vibrissae receptive fields could provide the brain with a phase signal that is, unlike that of the whisker afferents we report here and in past work (Severson et al., 2017), unperturbed by contacts between whiskers and objects in the world. Alternatively, whisker afferents that respond to whisking in air but not touch have also been found and could serve this role (Szwed et al., 2003). Neural circuits that separate touch and self-motion signals arising from the same neurons are also possible (Moore et al., 2015).

Recent reports have found that neurons in the trigeminal mesencephalic nucleus can be activated during periods of whisker motion, leading to the suggestion that MeV neurons encode whisking kinematics (Mameli et al., 2017; Mameli et al., 2010; Mameli et al., 2014). However, these studies were limited to anesthetized animals. To clarify whether MeV must be considered as a source of information about whisking kinematics (Bosman et al., 2011) during behavior, we recorded extracellularly from MeV units during periods of active whisking and during periods of licking. We found that MeV units did not encode whisk phase nor other rapid aspects of whisker motion. MeV units did encode the midpoint of whisking, albeit very modestly relative to other afferent classes. MeV houses the muscle spindles of jaw muscles, which spike during jaw movements (Goodwin and Luschei, 1975). We therefore speculate that these weak correlations with midpoint occur due to coordinated motion of the jaw and whisker pad, perhaps with subtle jaw muscle changes occurring at more protracted whisking midpoints (which occur at higher locomotion speeds; Sofroniew et al., 2014). However, we identified MeV units in our extracellular recordings based on responses to licking (presumably jaw-motion-correlated) or based on a unit being recorded on the same tetrode (nearby location) as a licking-correlated unit. It is possible that MeV houses neurons that we did not sample and that encode other aspects of whisking.

Together, our results provide a quantitative survey of how much information mechanoreceptors in the face can provide the mouse brain about whisking. Our data reveal that non-mystacial vibrissae can whisk in phase with the whiskers, and that mechanoreceptors innervating these non-mystacial vibrissae, as well as a subset of mechanoreceptors innervating facial hairy skin, can provide the brain with information about whisker motion comparable to mechanoreceptors that innervate the whiskers. Whisker mechanoreceptors provided the best, but not the only, source of information about whisking for the brain to use in whisker proprioception. We conclude that the coding of whisker self-motion occurs via a multitude of sensory signals arising from distinct classes of facial mechanoreceptors.

Materials and Methods

All procedures were in accordance with protocols approved by the Johns Hopkins University Animal Care and Use Committee.

Mice. Mixed background mice were housed singly in a vivarium with reverse light-dark cycle (12 hours each phase). Behavior experiments were conducted during the dark (active) cycle. The sex and line of each mouse used for recordings is detailed in Table S1.

Surgical preparation – TG recordings. Adult mice (6-18 weeks old) were implanted with titanium headcaps (Yang et al., 2016). Prior to electrophysiological recordings, two small openings (0.5 mm anterior-posterior, 2 mm medial-lateral) in the skull were made centered at 0 and 1.0 mm anterior and 1.5 mm lateral to Bregma, with dura left intact. Craniotomies were covered acutely with hemostatic gelatin sponge (VetSpon, Ferrosan Medical Devices) or chronically with silicone elastomer (Kwik-Cast, WPI) followed by a layer of dental acrylic (Jet Repair Acrylic).

Surgical preparation – MeV recordings. Custom microdrives with eight tetrodes (Cohen et al., 2012) were built to make extracellular recordings from MeV neurons. Each tetrode comprised four recording wires (100-300 k**Ω**). A ~1 mm diameter craniotomy was made (centered at -5.4 mm caudal to bregma, 0.9 mm lateral to midline) for implanting the microdrive to a depth of 2 mm, ~0.5 mm dorsal to MeV. Adult mice (9-18 weeks old) were implanted with a titanium headcap for head-fixation. The microdrive was advanced in steps of ~100 μm each day until reaching MeV, identified by the presence of clear high-frequency firing responses to jaw opening and/or closing. Putative MeV jaw proprioceptors were identified post hoc by clear modulations of spike rate aligned to lick times (Figure 3.7C).

Behavioral training and apparatus. Mice received 1 ml water per day for ≥ 7 days prior to training. Mice were head-fixed and placed on a linear treadmill to promote whisking, as mice whisk during running. Voluntary bouts of running were encouraged by providing subsequent water rewards via a custom lickport. On training days (2-10 days total), mice were weighed before and after each session to determine the volume of water consumed. If mice consumed < 1 ml, additional water was given to achieve 1 ml total. During recordings, treadmill position was tracked with a custom optical rotary encoder comprised of a 3D printed encoder disk (2 cm diameter, 20 holes) and a commercial photointerrupter (1A51HR, Sharp).

Whisker and other hair trimming. One day prior to electrophysiological recording, non-mystacial hairs on the left side of the face were trimmed short with fine forceps and microdissection scissors (Fine Science Tools), during isoflurane (1.5%) anesthesia. For TG recordings, all whiskers and microvibrissae were trimmed short except β, γ, δ, B1-4, C1-4, and D1-4. For improved tracking of whiskers, we minimized obstruction of the field of view by hairs that were not whiskers intended to be tracked. We did not use chemical hair remover. Fur between the whiskers was manually removed by plucking or trimming. Non-whisker hairs were maintained at this short length by repeating this procedure as necessary. Receptive fields on facial hairy skin were always on fur cut <1 mm by trimming. Whisker and non-mystacial vibrissa afferents were recorded while the vibrissa in the receptive field was at or near its intact length.

Trigeminal ganglion electrophysiology. Recordings from TG afferents were performed as described (Severson et al., 2017). Briefly, awake mice were head-fixed and allowed to run on the treadmill. The craniotomy was exposed and covered with PBS. A single tungsten recording electrode (2 MΩ nominal, Parylene coated; WPI) was lowered ~5.5 mm until it reached the TG. The tissue was allowed to relax at least 10 min to stabilize recordings. An identical reference electrode was lowered to a similar depth or placed outside the craniotomy in the PBS. The differential electrophysiological signal between recording and reference electrodes was amplified 10,000x, bandpass filtered between 300 Hz and 3,000 Hz (DAM80, WPI), and acquired at 20 kHz in 5 second sweeps. Electrophysiology, high-speed video, and other measurements were synchronized by Ephus (Suter et al., 2010) or WaveSurfer (http://wavesurfer.janelia.org) software. A micromanipulator (Sutter Instruments) advanced the recording electrode until a well-isolated unit responsive to manual touch stimulation was encountered. The unit's receptive field, response type (RA or SA), and direction selectivity were manually classified. All whiskers except the row containing the whisker-of-interest and/or surrogate tracking whisker were trimmed short. Small manual movements of the treadmill encouraged the mouse to run and whisk. After recordings, the craniotomy was covered with silicone elastomer and a thin layer of dental acrylic. Spike waveforms were obtained by thresholding high-pass filtered (500 Hz) traces and clustered using MClust-4.1 or MClust-4.4 (AD Redish et al.). A subset of TG whisker afferent recordings is reanalyzed from a previous report (Severson et al., 2017), as detailed in Supplemental Table 1.

MeV electrophysiology. Water was intermittently delivered via a lickport tube placed below the animal's snout. Lick signals were recorded by a custom electrical circuit designed to detect when the tongue contacted the lickport. Lick traces and broadband voltage traces from individual tetrode wires were acquired continuously at 30 kHz (Intan Technologies). Signals were bandpass filtered online between 0.1 Hz and 10 kHz, highpass filtered offline below 500 Hz, and spikes were detected using a threshold of 4-6 standard deviations of the filtered signal. The timestamp of the peak of each detected spike, as well as a 1-ms waveform centered at the peak, were extracted from each channel of the tetrode for spike sorting, and clustered using MClust (AD Redish et al.).

Mapping facial hairy skin receptive fields. The touch receptive fields of TG units were identified with a hand-held probe, while monitoring activity using an audio monitor (Model 3300, A-M Systems). When a whisker receptive field could not be found, the receptive field could often be located after probing hairy skin on the entire face. In these cases, before recording began, the extent of the receptive field was mapped by determining the region of hair and skin in which gentle touch with fine forceps

(Dumont AA, tip dimensions 0.4 mm x 0.2 mm; FST, #11210-10) evoked spikes and marked with a fine, water-based color marker (0.3 mm tip, Micro-Line, Platinum Art Supplies). Following the recording, the mouse's head with marked receptive fields and a micro-ruler (Electron Microscopy Sciences, #62096-08) were photographed (13 megapixel camera, LG Stylo 2) from the side, above, and/or below. The receptive fields were then compiled on a template "face map". The template image was drawn by outlining the profile and fiducial marks (e.g. eye, whisker follicles, nostrils) of a side view image of a mouse's face in Adobe Illustrator CS 6 (Adobe Systems). The approximate shape, location, and relative size of each imaged receptive field were mapped onto the template by: outlining the receptive field, locating nearby fiducial marks in the original image, applying a fixed scaling to match receptive field and template image dimensions, and translating to align to fiducial marks in the template image. Using the SVG Interactivity Panel in Illustrator, receptive fields were tagged with unique identifier text and their coordinates exported to a text file subsequently read into MATLAB. Borders of each zone of the face (e.g. pad, cheek) were drawn by outlining and connecting fiducial marks (Figure 3.4). Receptive fields were designated to the zone in which the center of mass was located.

High-speed videography. Video frames (640 pixels x 480 pixels, 32 μm/pixel) were acquired at 500 Hz using a PhotonFocus DR1-D1312-200-G2-8 camera (90 μs exposure time) and Streampix 5 software (Norpix). Light from a 940 nm LED (Roithner Laser) was passed through a condenser lens (Thorlabs), through the whisker field, reflected off a mirror (Thorlabs), and directed into a 0.25X telecentric lens (Edmund Optics). Ephus or WaveSurfer triggered individual camera frames (5 seconds, 2,500 frames per sweep) synchronized with electrophysiological recordings. To record microvibrissa movement, whiskers were trimmed, except for the D-row whiskers used for tracking whisker movement. The LED was rotated 30° to capture an oblique view of the profile of the mouse's face, thus maximizing the apparent length of the microvibrissae to enable tracking. To record facial and supraorbital vibrissa movements, the mouse's fur was trimmed to <1 mm, as described above. Whiskers and microvibrissae were trimmed to the base, except for the A-row whiskers used for tracking whisker movement. An additional mirror was placed in the light path to capture a side view of the mouse's face.

Video analysis. All whisker tracking was computing using the Janelia Whisker Tracker (Clack et al., 2012). X-Y coordinates of the whisker objects for each frame were computed by tracing the backbone of each whisker at subpixel-resolution. To reduce noise in measurement of θ, we truncated the tracked whisker trace at its intersection with that frame's "facemask", a curve offset from an outline of the face profile. The facemask was drawn for each frame, briefly, by fitting a smoothing spline to the contour of the face and performing several other image processing steps in MATLAB (Severson et al., 2017). The whisker's follicle location was then estimated by extrapolating past the facemask along the angle of the whisker base (Pammer et al., 2013; Severson et al., 2017). A simple "linking" algorithm was used to ensure the same whisker was tracked across frames. Traced objects outside of the expected region of interest, e.g. whisker pad, and outside of the expected length range were excluded. Whisker identity was then determined based on its follicle X-coordinate in either ascending or descending order. Finally, a number of events could render individual videos ineligible for further processing. These events included objects placed in or entering the video frame or grooming behavior. Using a custom GUI, every sweep was inspected to determine if an exclusion event had occurred.

Processing kinematics. We used the Hilbert transform to quantify the instantaneous phase (Φ), amplitude (θ_{amp}) and midpoint (θ_{mid}) of bandpass (8-30 Hz, Butterworth) filtered θ (Hill et al., 2011). Instantaneous whisking frequency (f_{whisk}) was calculated by taking the time derivative of the unwrapped Φ signal. We first smoothed θ with a Savitzky-Golay filter (3rd order, span of 9 frames) and interpolated missing frames when possible. Angular velocity, θ', the time derivative of θ, was calculated using central differences and smoothed with the same Savitzky-Golay filter. Sweeps with more than 2% of frames having missing θ data were excluded. For θ, θ', θ_{amp}, f_{whisk}, θ_{mid}, observations outside of the 0.25 and 99.75 percentiles were excluded. No outlier removal was performed on Φ. We calculated cross-correlation values (MATLAB 'xcorr' with 'coeff' option) on pairs of traces for whiskers and non-mystacial vibrissae (Figure 3.5E) after converting the sampling intervals from equally spaced time intervals to equally spaced phase intervals, using linear interpolation separately for each whisk cycle. Whisk cycles containing any non-whisking frames were removed. For cross-correlation analysis, we included between 79 and 333 videos for each session, including 195-591 seconds of whisking data.

Tracking facial movement. We acquired epochs of facial movement with high-speed video (500 Hz, 480 pixels x 640 pixels, 32 μm/pixel) to analyze correlations between facial skin movement and whisker kinematics (Figure 3.4). Two mirrors were placed in the light path to capture a side view of the mouse's face. Facial hair and whiskers were trimmed short except two A-row whiskers for tracking whisker movement. Displacement of each pixel for each frame was estimated by applying an image registration algorithm (MATLAB "imregdemons" with pyramid level iterations 32, 16, 8, and 4) that aligns each "moving" frame with a "fixed" template frame. First, fixed and moving frames were resized by half on each dimension (to 320 pixels x 240 pixels; MATLAB "imresize" with bicubic smoothing) to reduce compute time and file size. Next, pixel values outside of the face and in the eye were set to zero. Image registration was then applied to every video frame in the session. We then calculated Pearson's correlation coefficients between the time series of x-dimension pixel displacement values (Δx) and whisker position (θ) time series. Y-displacement values were not used for calculating correlations because they could not be estimated as accurately from 2D images, due to substantial out-of-image-plane curvature of the mouse face that varies along the y-dimension. Mean Pearson's r values for each facial region (Figure 3.4E) were obtained by averaging *r* values across all pixels within each facial region. These regions were determined for the fixed template image using fiducial marks as described above.

Data analysis – tuning curves. To calculate tuning curves, kinematic variables were processed by performing outlier removal, restricting observations to whisking periods, and binning into 30 equally spaced bins, unless otherwise noted. Bins with fewer than 25 observations were set to NaN.

Data analysis – mutual information. Mutual information (MI) was calculated between the distributions of spike counts and kinematic variable values across individual 2 ms frames. The distribution of spike counts was $P(X = x), x \in \{0,1,2, \ldots n\}$, where *n* is the maximum number of spikes observed during a single 2 ms frame across the duration of the recording. For the recordings presented here, *n* was ≤ 3. For each kinematic variable, *Y*, the distribution $P(Y)$ was estimated after binning *Y* into 16 equally spaced bins ranging from max(*Y*) to min(*Y*) after removing outliers as described above. Uniform count binning of kinematic variables yielded similar results for θ_{mid} and Φ (Figure 3.9). The joint distribution $P(X = x, Y = y)$ was estimated similarly. MI (Cover and Thomas, 2006) was then computed as:

$$MI(X;Y) = \sum_{x \in X, y \in Y} P(x,y) log_2 \frac{P(x,y)}{P(x)P(y)}$$

To obtain the "MI rate", we multiplied MI by the sampling frequency, which was always 500 Hz. To calculate "normalized MI" for each recording, we first calculated the entropy of the spike count distribution:

$$H_X = -\sum_{x \in X} P(x) \log_2 P(x).$$

Normalized MI was then computed as:

$$Normalized\ \ MI = \frac{MI(X;Y)}{H_X}$$

Discussion

The previous chapters chronicled my work on primary afferent encoding of active touch and self-motion using whisking as a model for active sensation. The following section will discuss the problems addressed, findings, significance, limitations, and future directions for each chapter.

In Chapter 1, we set out to define the mechanical variables underlying the activity of Merkel afferents innervating whisker follicles during active touch. We find that bending moment and its rate of change largely explains spiking by Merkel and slowly adapting afferents during whisking against an object. Excellent prediction of spiking by a simple mechanical model suggests that a viscoelastic transformation by whisker follicle tissues may underlie this sensitivity to moment and its rate of change.

These findings have far-reaching implications. First, defining the mechanical sensitivities of the primary afferents in the whisker system informs the field about the relevant channels of tactile information extracted by pre-neuronal and neuronal processes. One channel provided by Merkel afferents is essentially a low-frequency filter of contact moments that could be used for shape coding downstream. For example, theoretical work (Solomon and Hartmann 2011; Pammer, O'Connor et al. 2013) proposes that mechanical signals at the whisker base can be used to determine the radial distance of contact with an object. Specifically, the relative magnitudes of either moment and axial force or of moment and its rate of change are informative about this radial distance. We found that moment and its rate of change were predictive of Merkel afferent spiking. Axial force was less predictive. This suggests that the latter calculation method and input from Merkel afferents alone could be used by downstream neurons to calculate radial distance. Feedback about the velocity of movement is required for this computation. The former calculation involving axial force would require another afferent source, which, so far, has not been found.

Another significant result of these findings is the demonstration that identified Merkel afferents can be effectively modeled by a Kelvin-Voigt viscoelastic model during active touch, consistent with prior modeling of responses during passive touch and artificial whisking (Mitchinson et al., 2004). This suggests that the location and mechanical properties of the receptor and nearby tissues are critical for understanding the response properties of mechanoreceptors. Merkel afferents are stereotypically located at the edge of the keratinocyte-rich epidermis. This location poises these receptors for elastic coupling to keratin- and collagen-rich keratinocytes. Our model suggests that this transduced elastic stress is necessary for the classic slowly adapting properties of Merkel cells and their associated afferents. Similar viscoelastic models have been useful for understanding mechanical filtering by other receptor types in glabrous skin. For example, the Pacinian corpuscle is known for its coding of high frequency vibrations and large receptive fields. The Pacinian corpuscle ending structure is composed of a thin nerve fiber ensheathed by numerous concentric layers of glial tissue from non-myelinating Schwann cells (reviewed in: Fleming and Luo, 2013). Our current understanding is that the viscous layers of tissue act to filter out low-frequency mechanics such that stress only results from the dynamics of high-energy vibrations propagating through the tissue. Viscoelastic models will be instrumental for defining how mechanics are encoded by other afferent types. Thus, based on our mechanical framework, the functions of mechanoreceptors should depend on the location, shape, and mechanical properties of the end organ structure. This leads us to limitations of our study of Merkel afferents during active whisker touch.

First, our imaging setup and mechanical modeling was restricted to the radial-azimuthal plane. The vertical orientation of the pole and predominantly azimuthal rotation of the whiskers allowed us to disregard relatively small forces and kinematics in the elevation dimension. We also disregard twisting moment and bending moment in the elevational-radial plane, which should be small relative to the bending moment we measured in the azimuthal-radial plane. Three-dimensional imaging would allow quantification of all three moments. It has been shown recently that whisker torsional angle is highly correlated with whisker angle (Knutsen et al., 2008). We took advantage of this fact to reduce apparent changes in curvature due to torsion. Our setup allowed us to collect and analyze large numbers of samples within these restricted dimensions. However, our findings were limited by this setup. For example, we found slowly adapting neurons were almost always direction selective, i.e. sensitive to contact in the protraction or retraction direction. Our limited setup prevented us from analyzing the direction selectivity in the elevation dimension, and thus we could not measure the two-dimensional orientation selectivity. Future studies could relate orientation selectivity, measured using controlled passive deflections in all directions, to sensitivity to moments measured in three dimensions during active touch. To achieve variability in the angle of contact moments, the pole could be oriented at various angles, e.g. slanted toward or away from the animal. I predict that Merkel and other afferents are sensitive not only to object location, but also object orientation. This could have important implications for the amount of shape information that is already present at the primary afferent encoding stage.

Our ability to label the cell type of whisker afferents was a step forward, as the type of structure does inform us about its function. However, a major limitation of this work was our inability to define the exact morphology of each afferent we recorded. We were agnostic to the gross location of our Merkel afferent endings in either the ring sinus or Rete ridge collar, although the vast majority (~95% of counted endings) reside in the ring sinus. For Merkel afferents, fine morphological reconstruction could explain much of the within-type variability we observed. Functional properties, including orientation selectivity, mechanical threshold, mechanical sensitivity, and sensitivity to mechanics during whisking in air could be explained by the number and location of Merkel afferent end feet contacts onto Merkel cells. Similarly, the activity of a rapidly adapting afferent could be explained by the number and location of its longitudinal lanceolate endings. The whisker afferent is an ideal system to test this structure-function hypothesis because of our ability to accurately quantify the mechanical inputs at the base of the whisker.

We found that mechanical adaptation largely explains spiking during active touch. We disregarded other putative sources of adaptation, such as channel inactivation. Mechanotransduction for touch and proprioception depends on the mechanosensitive channel Piezo2 (Coste et al., 2010; Ranade et al., 2014; Woo et al., 2015). Mechanically-induced currents in Merkel cells and their associated afferents in touch domes and whisker follicles depend on Piezo2 (Woo et al., 2014; Ikeda et al., 2014). Mechanically-activated currents in cells expressing Piezo2 adapt rapidly, and alternative splicing alters the adaptation properties of the channel (Szczot et al., 2017). Merkel cells express a more slowly adapting isoform of Piezo2, and sensory neurons in the DRG express a variety of isoforms. Adaptation observed in different types of mechanoreceptors may depend on channel inactivation properties of Piezo2 splice variants. Future work should catalog the splice variants and adaptation properties of Piezo2 expressed in genetically-defined types of mechanoreceptors. Furthermore, understanding how mechanical and electrical adaptation interact will improve our models of how mechanical signals are transduced in various tactile sense organs, such as hairy skin, whiskers, and fingertips.

Another limitation is that we did not take full advantage of the genetic tools at our disposal. Genetic access to mechanoreceptor cell types allowed us to optogenetically label Merkel afferents in vivo. This gave us the ability to define the mechanical sensitivities that drive spiking in Merkel afferents. Given these results, we can only speculate on the functional importance of this cell type. Other genetic tools, such as optogenetic and chemogenetic silencing, have been used by numerous studies to assess the function of cell types in behaving animals. Transient inactivation of Merkel afferents could cause deficits in touch-dependent behaviors, such as discrimination of object location, shape, or texture. Central projections to particular trigeminal nuclei could also be silenced to assess the necessity of particular pathways in these behaviors. Similarly, sufficiency could be tested by optogenetic activation (O'Connor et al., 2013). Similar methods could be extended to other cell types and sensory organs. The TrkC-CreER line we utilized is very specific (>99% Merkel afferent labeling) but may not be efficient enough to allow proper assessment of the functional importance of Merkel afferents. Thus, it is important to continue to develop genetic labeling techniques to specifically and efficiently label mechanoreceptor types in rodents and other species.

In Chapter 2, we set out to define the mechanical stresses that underlie whisker afferent responses during whisking in air. We observed strong phase coding in many afferents, which we found results from mechanical stresses related to whisker inertia and muscle activation.

Of significance, we identified Merkel afferents as one source of self-motion information. Thus, at least in the whisker follicle, the Merkel afferent is a type of cutaneous proprioceptor. This sensitivity depends on the whisker's moment of inertia, which we decreased by a simple whisker cutting manipulation. Whisker moment of inertia can be increased by "loading" the whisker with a small mass at different radii (data not shown). If the mass is placed further from the base of the whisker, the moment of inertia increases exponentially. We expect phase tuning responses, especially at phases where the magnitude of acceleration and jerk are highest, to increases as a result of whisker loading. An advantage of whisker loading, as opposed to whisker cutting, is that it is reversible. Such a reversible manipulation could be used to assess the role of whisker afferent inputs for whisker proprioception. Characterization of primary afferent and cortical responses to addition of moment of inertia is currently ongoing.

Another significant finding was that internal stresses correlated with muscle actuation were sufficient to cause spiking in primary afferents. After cutting the whisker, spiking remained in many afferents at phases consistent with activation of protractor and retractor muscles. We believe this occurs due to torque produced by the whisking muscles on the whisker follicle (Hill et al., 2008). Resulting viscoelastic reaction forces in the surrounding tissues could also play a role. The intrinsic protractor muscle is shaped like a sling, as it wraps deep around the outside of the whisker follicle sinus capsule and attaches superficially on the skin. Contraction of this muscle could cause a bending moment at the base of the whisker with the same sign as protraction contact and positive acceleration. The extrinsic retractor muscles extend from from either side of the caudal snout and from the caudal upper lip to superficial attachments near the Rete ridge collar of each whisker follicle. Contraction of this muscle could also produce a bending moment at the base of the whisker follicle. This moment should be the same sign as retraction contact and negative acceleration. We did not find any effect consistent with actuation of the extrinsic protractor *m. nasolabialis profundus*, which has been measured in rat (Hill et al., 2008). We were also not able to record EMG responses in this muscle. This muscle is present in mice, but it is smaller and perhaps less active or weaker in mice compared to rats. The sufficiency of these internal stresses to cause spiking in primary afferents suggests that other cutaneous proprioceptors could be sensitive to muscle-related stresses and resulting skin strain.

Another limitation is that our mechanical models fitted for touch in Chapter 1 were not applied to predict responses during whisking in air. The results of the moment of inertia manipulation suggests that whisker afferents are sensitive to inertial moment, but we did not show that spiking correlates with inertial moment or that dynamics of inertial moment predict spiking during whisking in air. There are some technical considerations that prevented us from doing so. Our quasistatic bending moment computation depends on a single point force applied by the pole onto the whisker. Even though our curvature measurements from the high-speed video are sensitive enough to detect curvature changes during whisking, computation of bending moment cannot be applied during whisking, as inertial moment results from a distributed force. Whisker dynamics during noncontact whisking can be simulated by modeling the whisker as multiple discrete nodes (Quist et al., 2014). This type of model could be applied to our dataset to model moments during contact as well as whisking. We could then test whether the same dynamic model fitted during touch could predict responses during whisking in air. This approach would essentially unify the mechanical model to account for spiking across the physiological range of mechanical stresses experienced by afferents in the whisker follicle. This range includes small stresses resulting from inertial bending and muscle actuation relevant for self-motion coding, moderate stresses resulting from bending against objects and low frequency vibrations relevant for shape coding, and large stresses resulting from rapid vibrations such as slip events relevant for texture coding. For large stresses, dynamic whisker models must be applied. Future studies should aim to produce a unified mechanical model for each type of mechanoreceptor.

One limitation of the work is that whisker cutting manipulations were not performed on identified Merkel afferents. It is possible that we included data from other afferent types that are slowly adapting. Screening for identified Merkels sensitive to whisking in air would have been especially difficult. Yield from this method was low, due to the sparse expression of channelrhodopsin-positive cells and difficulty of tamoxifen dosing at embryonic timepoints. Compounding this low yield with the minority fraction of whisking-sensitive cells would have significantly extended the amount of time necessary to collect the number of units required to make a conclusion about the effect of whisker cutting on afferent self-motion responses. These experiments should be repeated in the future using TrkC-CreER labeling, more efficient genetic labeling, cell-filling, or another high-throughput technique to confirm that slowly adapting afferents sensitive to whisker inertia are indeed Merkel afferents.

In Chapter 3, we set out to compare information encoded by responses of all possible mechanoreceptor types in the face during whisking. We found that whisker afferents, along with some hairy skin and other vibrissa afferents, encoded the most information about whisking kinematics.

One significant result is that this study provides evidence that whisker afferents provide significant proprioceptive information to the brain. The functional relevance of these inputs to the system should be investigated further. The effect of whisker cutting and loading manipulations should be restricted to afferents in the whisker follicle; afferents on other whiskers and outside of whisker follicles should not be affected. These manipulations could be useful tools to assess the specific contribution of whisker afferents to cutaneous proprioception in downstream circuits. One next step is to characterize how whisking kinematics are encoded in primary (wS1) and secondary (wS2) somatosensory cortices. It is known that Layer 4, the main input layer, of wS1 receives self-motion information from ventral posterior medial (VPM) region of thalamus, which has both touch and self-motion responses (Moore et al., 2015). PV-interneurons encode whisking and largely cancel out whisking-related activity in excitatory cells in Layer 4 (Yu et al., 2016). Layer 5A and, to a lesser extent, Layer 5B, encode whisking (de Kock and Sakmann, 2009). Models suggest that these whisking-related responses in Layer 5 may be inherited directly from VPM and the posterior medial (POm) thalamus (Oberlaender et al., 2011). Self-motion responses have not been measured in wS2. We are currently measuring wS2 and wS1 responses during whisking and testing the effect of whisker cutting and loading manipulations at this level. If whisking responses change as a result of these manipulations, it suggests that whisker afferents are indeed a major source of self-motion information. If not, other sources, such as hairy skin afferents, could provide this information to the system.

It is plausible that other afferents could provide complimentary or sufficient information about whisking that are not “corrupted” by touch events. In my experience, hairy skin afferents innervating fur adjacent to whisker follicles were not sensitive to whisker touch. These afferents may be the “whisking-only” cells that Ahissar and colleagues described (Szwed et al., 2003). A touch-invariant self-motion signal would be useful for determining the phase of the whisk cycle in the midst of contact events that would otherwise mask the self-motion activity of whisker afferents during touch. This anecdotal observation should be confirmed by recording hairy skin afferents during self-motion and touch of nearby whiskers.

One limitation of this study is that facial movement was restricted to whisking behavior. We used a simple measure of displacement to estimate how correlated displacements of different areas of skin were with whisker position. Other methods, such as 3-D digital image correlation, are capable of measuring strain on a three-dimensional surface. This method is commonly used in materials science for stress tests. Digital image correlation has been applied to measure strain fields in human subjects (Hsu et al., 2014). This method could be used to study how mechanoreceptors encode other facial movements, as other facial movements would likely activate unique subsets of afferents. For example, blinking likely activates receptors near the eye, jaw movements activate cutaneous receptors around the jaw and lips, and nose movements would activate receptors around the snout. Future studies could work toward building a general model of facial mechanoreceptor activity by correlating responses with strains measured in facial skin. The identities of these cutaneous proprioceptors we recorded are unknown.

Another limitation is that we did not genetically or morphologically identify any cutaneous afferents in our study of mechanoreceptor activity during whisking. We assume that the slowly adapting afferents on whiskers and other vibrissa were Merkel afferents. The identity of the whisking-sensitive rapidly adapting afferents is unknown. Hairy skin afferents responsive during whisking were manually characterized as rapidly adapting, occupying large receptive fields, innervating downy fur, and sensitive to skin stretch. These properties are consistent with a known receptor type, the Field-LTMR (Bai et al., 2015). I hypothesize that Field-LTMRs on facial hairy skin may be specialized cutaneous proprioceptors. This hypothesis should be tested by recording responses of identified Field-LTMRs during facial movements such as whisking. It is also possible that these cutaneous proprioceptors belong to another identified or yet unidentified cell type in hairy skin. Once these cutaneous proprioceptors are genetically identified, future studies could use transient inactivation techniques or specific chronic lesion to assess the functional relevance of cutaneous proprioception during development and motor learning.

Despite these limitations, our findings have significantly advanced our understanding of the mechanics underlying mechanoreceptor encoding of active touch and self-motion using whisking as a model. Touch and proprioception signals already interact at the mechanical and primary afferent level. Our work provides support for a mechanical framework that will have far-reaching implications for our understanding of active touch and proprioception.

Appendix

Chapters 1 & 2 Glossary:

"Contact" periods: Frames with positive contact classification and d_{pole} < 1 mm.

"Whisking" periods: Frames with θ_{amp} > 2.5°.

"Whisking in air" periods: Whisking frames with negative contact classification and d_{pole} > 2 mm.

"Non-whisking" periods: Frames with θ_{amp} < 1° that are not contact frames.

"Touch-sensitive": Applies to a neuron with 95% confidence interval (CI) on mean spike rate during contact greater than and non-overlapping with both 95% CI for mean spike rate during non-whisking and 95% CI for mean spike rate during whisking in air.

"Whisking-sensitive": Applies to a neuron with 95% CI on mean spike rate during whisking in air greater than and non-overlapping with 95% CI for mean spike rate during non-whisking.

"T" neuron: Touch-sensitive but not whisking-sensitive.

"WT" neuron: Touch-sensitive and whisking-sensitive.

"WT*" neuron**:** WT neuron with mean spike rate > 1 Hz during whisking in air, and for which we collected at least 1,000 spikes (to calculate tuning surfaces, etc.).

"Outliers": For M_0, F_{ax}, F_{lat}, M_0', F_{ax}' and F_{lat}', observations not between the 0.5 and 99.5 percentiles (i.e. 1% total were excluded). For θ, ω, a, ζ, θ_{amp}, f_{whisk}, $\theta_{setpoint}$, observations not between 0.25 and 99.75 percentiles. No outlier removal was performed on Φ.

Chapter 3 Glossary:

“Whiskers”: macrovibrissae located on the mystacial pad.

“Non-mystacial vibrissae”: vibrissae that are not whiskers; includes supraorbital and genal macrovibrissae, and the microvibrissae.

“Whisking” periods: Frames with $\theta_{amp} > 2.5°$ and $f_{whisk} > 1$ Hz for the tracked whisker.

“Non-whisking” periods: Frames with $\theta_{amp} < 1°$ for the tracked whisker.

“Whisking-sensitive”: Applies to a unit with 95% confidence interval (CI) on mean spike rate during whisking in air non-overlapping with 95% CI for mean spike rate during non-whisking and with mean spike rate > 1 Hz during whisking.

“Whisker afferents” or “whisker mechanoreceptors”: LTMRs with single-whisker receptive fields, presumably which innervate the whisker follicle.

“Proprioceptors”: Mechanoreceptors presumed to associate with muscle spindle or Golgi tendon organ structures.

Recording ID	Mouse ID	Sex	Mouse line	Recording Date	Type	Identified Merkel afferent	Receptive field	Whisker length (mm)	Whisker base rad. (μm)	Whisking and touch sensitivity	Fitted by mech. model	Appearances - Chapter 1						Appearances - Chapter 2						
												Fig. 1.1	Fig. 1.2	Fig. 1.3	Fig. 1.4	Fig. 1.5	Fig. 1.6	Fig. 2.1	Fig. 2.2	Fig. 2.3	Fig. 2.4	Fig. 2.5	Fig. 2.6	Fig. 2.7
"Touch" recordings, with both whisker-pole contact and whisking in air																								
217F	KSt95	M	$TrKC^{CreER};Rosa^{Ai32}$	04/29/15	RA		γ	27.4	37.5	WT*	*N.A.*			C	C,D	A-E		C-E	A-D		B,G		A-F	B
227A	KSt107	F	$TrKC^{CreER};Rosa^{Ai32}$	05/15/15	RA		γ	19.4	41.0	WT	*N.A.*			C	C,D	A-E					B		A-F	
145B	KSt76	M	$TrKC^{CreER};Rosa^{Ai32}$	09/27/14	RA		C3	11.7	30.5	WT	*N.A.*			C	C,D	A-E					B		A-F	
194A	KSt88	M	$TrKC^{CreER};Rosa^{Ai32}$	03/20/15	RA		γ	30.0	43.0	WT	*N.A.*			C	C,D	A-E					B		A-F	
202A	KSt92	M	$TrKC^{CreER};Rosa^{Ai32}$	04/05/15	RA		C2	17.2	38.5	WT	*N.A.*			C	C,D	A-E					B		A-F	
163B	KSt77	M	$TrKC^{CreER};Rosa^{Ai32}$	11/10/14	RA		γ	25.6	45.0	T	*N.A.*			C	C,D	A-E					B		A-F	
125B	KSt66	M	$TrKC^{CreER};Rosa^{Ai32}$	07/11/14	RA		C1	24.8	41.5	T	*N.A.*			C	C,D	A-E					B		A-F	
221B	KSt106	F	$TrKC^{CreER};Rosa^{Ai32}$	05/14/15	SA		β	28.3	44.5	WT*	Y			C	C,D	A-E	C	C-E	A-D		B,G		A-F	B
225D	KSt107	F	$TrKC^{CreER};Rosa^{Ai32}$	05/14/15	SA		C2	16.4	39.0	WT*	Y	B		C	C,D,H	A-E	C	C-E	A-D		B,G		A-F	B
132A	KSt69	M	$TrKC^{CreER};Rosa^{Ai32}$	07/25/14	SA		β	27.7	46.5	WT*	Y			C	C,D	A-E	C	C-E	A-D		B,G		A-F	B
256B	KSt119	M	$TrKC^{CreER};Rosa^{Ai32}$	07/06/15	SA		C1	23.2	44.5	WT*	Y			C	C,D	A-E	C	C-E	A-D		B,G		A-F	B
223B	KSt101	F	$TrKC^{CreER};Rosa^{Ai32}$	05/11/15	SA		γ	25.2	44.0	WT	Y			C	C,D	A-E	C				B		A-F	
161A	KSt77	M	$TrKC^{CreER};Rosa^{Ai32}$	11/10/14	SA		D1	23.7	44.0	WT*	Y			C	C,D	A-E	C	C-E	A-D		B,G		A-F	B
167A	KSt82	M	$TrKC^{CreER};Rosa^{Ai33}$	12/08/14	SA		C1	25.0	42.0	WT*	Y			C	C,D	A-E	C	C-E	A-D		B,G		A-F	B
128D	KSt66	M	$TrKC^{CreER};Rosa^{Ai34}$	07/18/14	SA		γ	28.2	41.5	WT*	*N.A.*			C	C,D,I	A-E		C-E	A-D		B,G		A-F	B
221C	KSt106	F	$TrKC^{CreER};Rosa^{Ai35}$	05/14/15	SA		β	28.3	44.5	WT	Y			C	C,D	A-E	C				B		A-F	
198B	KSt89	F	$TrKC^{CreER};Rosa^{Ai36}$	03/31/15	SA		γ	24.4	42.0	WT	Y			C	C,D	A-E	C				B		A-F	
216D	KSt97	M	$TrKC^{CreER};Rosa^{Ai37}$	04/27/15	SA		C3	11.1	28.0	T	Y			C	C,D	A-E	C				B		A-F	
211A	KSt96	F	$TrKC^{CreER};Rosa^{Ai38}$	04/20/15	SA		B2	14.1	28.5	T	Y			C	C,D,I	A-E	C				B		A-F	
220B	KSt99	M	$TrKC^{CreER};Rosa^{Ai39}$	05/06/15	SA	Y	C1	23.1	43.0	WT*	Y		C,D	B,C	C,D	A-E	C	C-E	A-D		B,G		A-F	B
286A	KSt127	F	$TrKC^{CreER};Rosa^{Ai40}$	09/09/16	SA	Y	B2	15.0	37.0	WT*	Y		C,D	C	C,D	A-E	C	A-E	A-D		B,G		A-F	B
250A	KSt115	F	$TrKC^{CreER};Rosa^{Ai41}$	06/22/15	SA	Y	β	20.1	41.0	WT*	Y		C,D	C	A,C-E,	A-E	C	C-E	A-D		B,G		A-F	A-C
251B	KSt117	M	$TrKC^{CreER};Rosa^{Ai42}$	06/29/15	SA	Y	B2	17.6	36.5	WT*	Y		C,D	C	C,D,H	A-E	B-D	C-E	A-D		B,G		A-F	B
254C	KSt119	M	$TrKC^{CreER};Rosa^{Ai43}$	07/03/15	SA	Y	β	21.4	44.0	WT	Y		C,D	C	C,D	A-E	C				B		A-F	
207A	KSt91	M	$TrKC^{CreER};Rosa^{Ai44}$	04/13/15	SA	Y	C4	8.6	23.5	WT	Y		C,D	C	C,D	A-E	C				B		A-F	
154B	KSt80	F	$TrKC^{CreER};Rosa^{Ai45}$	10/25/14	SA	Y	δ	25.2	47.0	WT	Y		C,D	C	C,D	A-E	C				B		A-F	
265A	KSt122	M	$TrKC^{CreER};Rosa^{Ai46}$	07/19/15	SA	Y	D4	10.3	30.5	WT	Y		C,D	C	C,D	A-E	C				B		A-F	
234A	KSt111	M	$TrKC^{CreER};Rosa^{Ai47}$	05/29/15	SA	Y	C4	8.4	26.5	WT	Y		C,D	C	C,D	A-E	C				B		A-F	
231A	KSt109	F	$TrKC^{CreER};Rosa^{Ai48}$	05/21/15	SA	Y	C1	18.5	41.0	WT*	Y		C,D	C	C,D	A-E	C	C-E	A-D		B,G		A-F	B
243B	KSt112	M	$TrKC^{CreER};Rosa^{Ai49}$	06/10/15	SA	Y	D2	20.1	38.0	WT	Y		C,D	C	C,D	A-E	C				B		A-F	
266B	KSt124	F	$TrKC^{CreER};Rosa^{Ai50}$	07/21/15	SA	Y	B1	24.2	44.5	WT	Y		C,D	C	C,D,I	A-E	C				B		A-F	
220C	KSt99	M	$TrKC^{CreER};Rosa^{Ai51}$	05/06/15	SA	Y	B3	11.3	27.0	WT	Y	D-F	C,D	C	C,D	A-E	C				B		A-F	
282A	KSt126	M	$TrKC^{CreER};Rosa^{Ai52}$	08/31/16	SA	Y	B3	8.1	22.5	T	Y		C,D	C	C,D	A-E	C				B		A-F	
"Touch" recordings excluded from all analysis except to quantify tagging method (Figure S1)																								
227C	KSt107	F	$TrKC^{CreER};Rosa^{Ai32}$	05/15/15	SA	Y	δ	26.3	41.0	WT	*N.A.*		C,D											
214A	KSt94	F	$TrKC^{CreER};Rosa^{Ai32}$	04/24/15	SA	Y	B1	20.1	39.0	WT	*N.A.*		C,D											
271A	KSt123	F	$TrKC^{CreER};Rosa^{Ai32}$	07/29/15	SA	Y	D1	22.8	40.0	*N.A.*	*N.A.*		C,D											
"Cut whisker only" recordings obtained after the relevant whisker was cut (cf. Figure 7F)																								
199B	KSt89	F	$TrKC^{CreER};Rosa^{Ai32}$	04/01/15	SA	Y	D1 "	*N.A.*	*N.A.*	putative WT*	*N.A.*		C,D							G	B,F,G		A-F	
206A	KSt91	M	$TrKC^{CreER};Rosa^{Ai32}$	04/13/15	SA	Y	A1 "	*N.A.*	*N.A.*	putative WT*	*N.A.*		C,D							G	B,F,G		A-F	
209A	KSt93	M	$TrKC^{CreER};Rosa^{Ai32}$	04/16/15	SA	Y	A1 "	*N.A.*	*N.A.*	putative WT*	*N.A.*		C,D							G	B,F,G		A-F	
277A	KSm31	M	$Rosa^{Ai32}$	08/24/16	SA		E4 "	*N.A.*	*N.A.*	putative WT*	*N.A.*									G	B,F,G		A-F	
305A	KSt137	M	$Rosa^{Ai32}$	10/18/16	SA		α "	*N.A.*	*N.A.*	putative WT*	*N.A.*									G	B,F,G		A-F	
"Whisking in air without touch" recordings, whisker-pole contacts not analyzed due to too many whiskers in video																								
240A	KSt112	M	$TrKC^{CreER};Rosa^{Ai32}$	06/06/15	SA		B2	*N.A.*	*N.A.*	putative WT*	*N.A.*							C-E	A-D		B,G		A-F	B
253A	KSt119	M	$TrKC^{CreER};Rosa^{Ai32}$	07/02/15	SA		C2	*N.A.*	*N.A.*	putative WT*	*N.A.*							C-E	A-D		B,G		A-F	B
"Progressive whisker cutting" recordings, whisking in air without whisker-pole contact																								
278B	KSm30	M	$Rosa^{Ai32}$	08/31/16	SA		B2	12.2	24.0	putative WT*	*N.A.*									E-G	B-E,G		A-F	B
288C	KSt128	M	$TrKC^{CreER};Rosa^{Ai32}$	09/13/16	SA		B3	10.7	27.0	putative WT*	*N.A.*									E-G	B-E,G		A-F	B
295C	KSt131	M	$TrKC^{CreER};Rosa^{Ai32}$	09/23/16	SA		D1	21.1	30.0	putative WT*	*N.A.*									B,E-G	B-E,G		A-F	B
303A	KSt137	M	$Rosa^{Ai32}$	10/15/16	SA		D1	24.4	43.5	putative WT*	*N.A.*									E-G	B-E,G		A-F	B
304B	KSt137	M	$Rosa^{Ai32}$	10/17/16	SA		B2	17.1	35.0	putative WT*	*N.A.*									E-G	B-E,G		A-F	B
305B	KSt137	M	$Rosa^{Ai32}$	10/18/16	SA		B1	24.7	44.5	putative WT*	*N.A.*									E-G	B-E,G		A-F	B
309B	KSt135	M	$TrKC^{CreER};Rosa^{Ai32}$	10/24/16	SA		D2	17.6	38.0	putative WT*	*N.A.*									D-G	B-E,G		A-F	B
311C	KSt135	M	$TrKC^{CreER};Rosa^{Ai32}$	10/27/16	SA		C4	9.8	24.5	putative WT*	*N.A.*									C,E-G	B-E,G		A-F	B
313A	KSt138	M	$TrKC^{CreER};Rosa^{Ai32}$	11/20/16	SA		γ	21.5	46.5	putative WT*	*N.A.*									E-G	B-E,G		A-F	B
318A	KSt140	M	$TrKC^{CreER};Rosa^{Ai32}$	12/01/16	SA		C1	22.2	39.5	putative WT*	*N.A.*									E-G	B-E,G		A-F	B
321A	KSt140	M	$TrKC^{CreER};Rosa^{Ai32}$	12/05/16	SA		D1	22.3	45.0	putative WT*	*N.A.*									E-G	B-E,G		A-F	B
321B	KSt140	M	$TrKC^{CreER};Rosa^{Ai32}$	12/05/16	SA		C3	9.0	31.0	putative WT*	*N.A.*									E-G	B-E,G		A-F	B
295A	KSt130	M	$TrKC^{CreER};Rosa^{Ai32}$	09/23/16	RA		D1	18.6	28.5	putative WT*	*N.A.*									E-G	B-E,G		A-F	B
EMG recordings, during whisking in air																								
7A	KSm6	M	$Rosa^{Ai32}$	06/02/16	*N.A.*	*N.A.*	*N.A.*	*N.A.*	*N.A.*	*N.A.*	*N.A.*										A,D,F,G	D		
8A	KSm8	M	$Rosa^{Ai32}$	06/04/16	*N.A.*	*N.A.*	*N.A.*	*N.A.*	*N.A.*	*N.A.*	*N.A.*										A,D,F,G	D		
9A	KSm9	M	$CCK^{CreER};Rosa^{Ai32}$	06/10/16	*N.A.*	*N.A.*	*N.A.*	*N.A.*	*N.A.*	*N.A.*	*N.A.*										A,D,F,G	B,C,D		
11A	KSm11	F	$Rosa^{Ai9}$	06/16/16	*N.A.*	*N.A.*	*N.A.*	*N.A.*	*N.A.*	*N.A.*	*N.A.*										A,D,F,G	F,G,H		

Table 1. Meta-data for recordings and their assignment to analyses in Chapters 1 and 2.

Metadata for each afferent, including figure appearances. T: sensitive to touch, but not to whisking. WT: sensitive to both whisking and touch. WT*: sensitive to both whisking and touch, with mean whisking in air spike rate >1 Hz and >1000 spikes. *N.A.*: not applicable.

Mouse ID	Sex	Mouse line	Date of Birth	Recording Dates	Receptive Fields/ Regions of Interest	Unit IDs *prev. incl. in Severson, et al. 2017 ‡ whisking-sensitive	Appearances - Chapter 3								
							Fig. 3.1	Fig. 3.2	Fig. 3.3	Fig. 3.4	Fig. 3.5	Fig. 3.6	Fig. 3.7	Fig. 3.8	Fig. 3.9
Recordings of trigeminal ganglion neurons															
KSt66	M	$TrKC^{CreER};Rosa^{Ai32}$	05/09/14	07/11-07/18/14	whisker	125B*, 128D*‡		E						A-C	D-F
KSt69	M	$TrKC^{CreER};Rosa^{Ai32}$	05/09/14	07/28/14	whisker	132A*‡		E						A-C	D-F
KSt76	M	$TrKC^{CreER};Rosa^{Ai32}$	06/29/14	09/27/14	whisker	145B*‡		E						A-C	D-F
KSt80	F	$TrKC^{CreER};Rosa^{Ai32}$	06/29/14	10/25/14	whisker	154B*									
KSt77	M	$TrKC^{CreER};Rosa^{Ai32}$	06/29/14	11/10-11/12/14	whisker	161A*‡, 163B*		E						A-C	D-F
KSt82	M	$TrKC^{CreER};Rosa^{Ai32}$	07/20/14	12/08/14	whisker	167A*‡		E						A-C	D-F
KSt88	M	$TrKC^{CreER};Rosa^{Ai32}$	10/28/14	03/20-03/30/15	whisker; micro	194A*; 197C									
KSt89	F	$TrKC^{CreER};Rosa^{Ai32}$	10/25/14	03/31/15	whisker	198B*									
KSt92	M	$TrKC^{CreER};Rosa^{Ai32}$	10/28/14	04/01-04/05/15	whisker; cheek	202A*; 199A‡			A,D-F					A-B	
KSt91	M	$TrKC^{CreER};Rosa^{Ai32}$	10/28/14	04/13/15	whisker	207A*									
KSt96	F	$TrKC^{CreER};Rosa^{Ai32}$	01/28/15	04/20/15	whisker	211A*									
KSt94	F	$TrKC^{CreER};Rosa^{Ai32}$	10/28/14	04/23-04/24/15	whisker; eye	214A*; 213A‡			A,D-F					A-B	D,E
KSt95	M	$TrKC^{CreER};Rosa^{Ai32}$	10/25/14	04/29/15	whisker; SO	217F*‡; 217A,		E						A-C	D-F
KSt99	M	$TrKC^{CreER};Rosa^{Ai32}$	02/07/15	05/06/15	whisker	220B*‡, 220C*		E						A-C	D-F
KSt106	F	$TrKC^{CreER};Rosa^{Ai32}$	02/07/15	05/08/15	whisker	221B*‡, 221C*		E						A-C	D-F
KSt101	F	$TrKC^{CreER};Rosa^{Ai32}$	02/23/15	05/11/15	whisker	223B*									
KSt107	F	$TrKC^{CreER};Rosa^{Ai32}$	02/07/15	05/14-05/15/15	whisker	225D*‡, 227A*‡, 227C*		E						A-C	D-F
KSt100	M	$TrKC^{CreER};Rosa^{Ai32}$	10/25/14	05/18/15	cheek	228A‡			A,D-F					A-B	D,E
KSt109	F	$TrKC^{CreER};Rosa^{Ai32}$	02/07/15	05/21/15	whisker	231A*‡		E						A-C	D-F
KSt111	M	$TrKC^{CreER};Rosa^{Ai32}$	02/07/15	05/29/15	whisker	234A*									
KSt112	M	$TrKC^{CreER};Rosa^{Ai32}$	02/07/15	06/06-06/10/15	whisker; micro; G	240A*‡, 243B*; 242B; 242E		E						A-C	D-F
KSt115	F	$TrKC^{CreER};Rosa^{Ai32}$	02/07/15	06/19-06/22/15	whisker; SO	250A*‡; 247A		E						A-C	D-F
KSt117	M	CCK^{Cre}; $Rosa^{Ai32}$	01/03/15	06/29/15	whisker	251B*‡		E						A-C	D-F
KSt119	M	$TrKC^{CreER};Rosa^{Ai32}$	03/25/15	07/02-07/06/15	whisker; cheek; snout	253A*‡, 254C*, 256B*‡; 254A‡; 255B‡		E	A,D-F					A-C	D-F
KSt122	M	$TrKC^{CreER};Rosa^{Ai32}$	03/25/15	07/17-07/19/15	whisker; cheek	265A*; 263A‡			A,D-F					A-B	D,E
KSt124	F	$TrKC^{CreER};Rosa^{Ai32}$	03/25/15	07/21/15	whisker; cheek	266B*; 266A‡			A,D-F					A-B	D,E
KSt123	F	$TrKC^{CreER};Rosa^{Ai32}$	03/25/15	07/25-07/29/15	whisker; cheek; snout; eye	271A*; 268A‡; 270A‡; 270B‡			A,D-F					A-B	D,E
KSt125	F	$TrKC^{CreER};Rosa^{Ai32}$	03/25/15	08/04/15	eye	274A‡			A,D-F					A-B	D,E
KSm31	M	$TrKC^{CreER};Rosa^{Ai32}$	05/10/16	08/20-08/22/16	whisker; eye; pad	275A; 276A‡; 276B‡			A,D-F					A-C	D-F
KSm30	M	$Rosa^{Ai32}$	05/10/16	08/25-08/26/16	whisker; cheek	278B*‡; 279A‡		E	A,D-F					A-C	D-F
KSt126	M	$TrKC^{CreER};Rosa^{Ai32}$	05/10/16	08/29-08/31/16	whisker; SO	282A*; 280B									
KSt127	F	$TrKC^{CreER};Rosa^{Ai32}$	05/10/16	09/07-09/09/16	whisker	285A‡, 286A*‡		E						A-C	D-F
KSt128	M	$TrKC^{CreER};Rosa^{Ai32}$	01/20/16	09/13/16	whisker; pad	288C*‡; 288B‡		E	A,D-F					A-C	D-F
KSt130	M	$TrKC^{CreER};Rosa^{Ai32}$	09/27/15	09/23/16	whisker; cheek	295A*‡; 295B		E	A,D					A-C	D-F
KSt131	M	$TrKC^{CreER};Rosa^{Ai32}$	09/27/15	09/23/16	whisker	295C*‡		E						A-C	D-F
KSt137	M	$Rosa^{Ai32}$	05/10/16	10/15/16	whisker	303A*‡, 304B*‡, 305B*‡		E						A-C	D-F
KSt135	M	$TrKC^{CreER};Rosa^{Ai32}$	05/10/16	10/24-10/27/16	whisker; snout; pad	309B*‡, 311C*‡; 309A; 311A‡		E	A,D-F					A-C	D-F
KSt138	M	$TrKC^{CreER};Rosa^{Ai32}$	05/10/16	11/20/16	whisker	313A*‡		E						A-C	D-F
KSt140	M	$TrKC^{CreER};Rosa^{Ai32}$	05/10/16	12/01-12/05/16	whisker	318A*‡, 321A*‡, 321B*‡		E						A-C	D-F
KSt143	M	$TrKC^{CreER};Rosa^{Ai32}$	07/04/16	02/17-02/22/17	whisker; snout; eye; pad	332A; 329B, 333B‡; 331A; 332C‡			A,D-F					A-C	D-F
KSt145	M	CCK^{Cre}; $Rosa^{Ai32}$	07/04/16	02/24-02/28/17	eye; G; micro	335A‡, 338A; 336A‡; 338B‡			A,D-F	I,J				A-B	D,E
KSt148	F	$TrKC^{CreER};Rosa^{Ai32}$	10/24/16	03/02-03/05/17	cheek; eye; pad; micro	341A, 342A; 341B; 341C‡; 343A			A,D-F					A-C	D-F
KSt147	F	$TrKC^{CreER};Rosa^{Ai32}$	10/24/16	03/07-03/08/17	whisker; eye; micro	345B‡; 345A‡, 346A; 346B‡		E	A,D-F	I,J				A-C	D-F
KSt150	M	$TrKC^{CreER};Rosa^{Ai32}$	10/24/16	03/16-03/27/17	whisker; micro; SO; eye; cheek; lip; pad; snout	350C‡; 349A‡, 350D‡; 349B‡; 350A; 350B‡, 352C, 356A‡; 351C‡, 352A‡; 351E‡, 352B‡, 354C‡, 355A‡; 353B‡, 354A, 354B		E	A,D-F	I,J				A-C	D-F
KSt149	F	$TrKC^{CreER};Rosa^{Ai32}$	10/24/16	03/30/17	SO	358A‡				I,J				A-C	D-F
KSt151	M	$TrKC^{CreER};Rosa^{Ai32}$	10/24/16	04/17-04/18/17	micro; jaw; cheek	359A‡; 360A, 363A; 361A, 361E‡, 363B‡			A-F	I,J				A-B	D,E
KSt152	M	$TrKC^{CreER};Rosa^{Ai32}$	10/24/16	04/25-04/28/17	lip; cheek; snout	364A‡, 365A‡; 364B; 367A			A,D-F					A-B	D,E
KSt155	M	$TrKC^{CreER};Rosa^{Ai32}$	12/07/16	07/10-07/17/17	whisker; cheek; jaw; micro; SO; pad	375B‡, 377A‡; 372A; 373A, 373B; 374B; 375C, 376B‡; 376A		E	A,D	I,J				A-C	D-F
KSt154	M	$TrKC^{CreER};Rosa^{Ai32}$	12/07/16	07/20-07/26/17	whisker; jaw	379C, 380A‡; 383A‡		E	A,D-F					A-C	D-F
KSt157	F	$TrKC^{CreER};Rosa^{Ai32}$	12/07/16	08/07-08/12/17	whisker; eye; cheek; jaw	387A, 387C‡; 386A‡; 387B‡, 390B; 390A		B-E	A,D-F					A-C	A-F
KSt158	F	$TrKC^{CreER};Rosa^{Ai32}$	12/07/16	08/16-08/29/17	whisker; jaw; cheek	402A‡; 394A‡, 401A, 401B‡; 394B‡, 395A‡, 397A‡		E	A-F					A-C	D-F
KSt161	M	CCK^{Cre}; $Rosa^{Ai32}$	07/04/16	09/22-09/25/17	whisker; eye	405A‡,406C‡; 406B‡		E	A,D-F					A-C	D-F
KSt163	M	$TrKC^{CreER};Rosa^{Ai32}$	08/08/17	01/12-01/16/18	SO; snout; pad; lip	408A, 409A, 410B‡, 409B‡, 410A, 411C; 406A‡, 409C‡, 411B‡; 411A‡			A,D-F	I,J				A-C	D-F
KSt164	M	$Rosa^{Ai32}$	08/08/17	01/29-02/07/18	eye; snout; SO; cheek, pad	415A‡, 420A‡; 416A‡, 420B‡; 416B; 417B‡; 418A‡			A-F					A-C	D-F
KSt166	M	$TrKC^{CreER};Rosa^{Ai32}$	08/09/17	02/08-02/16/18	whisker; cheek; snout; SO; G	422C‡, 422D‡; 421B‡, 424A‡; 421C‡, 421D‡; 422A, 422B‡, 424B, 425A‡, 425D; 425C	C,D	B-E	A,D-F	I,J				A-C	D-F
KSt165	F	$TrKC^{CreER};Rosa^{Ai32}$	08/09/17	02/20-02/21/18	G	427A, 428B									
KSt167	F	$TrKC^{CreER};Rosa^{Ai32}$	08/09/17	02/24/18	G	430A‡, 430B, 430C				I,J				A-B	D,E
Recordings of trigeminal mesencephalic nucleus neurons															
HYLC44	M	$TH^{Cre};Rosa^{Ai32}$	12/07/15	05/24-05/30/16	MeV	44B-2‡,3‡,4‡; 44C-15‡,16‡						B-F		A-C	D-F
HYLC46	M	$DBH^{Cre};Rosa^{Ai32}$	12/30/15	06/08/16	MeV	46A-6‡,7‡						F		A-C	D-F
HYLC48	M	$DBH^{Cre};Rosa^{Ai32}$	01/10/16	08/17/16	MeV	48D-5‡,6‡,7‡,8‡						F		A-C	D-F
HYLC52	M	$DBH^{Cre};Rosa^{Ai32}$	05/12/16	08/31/16	MeV	52A-16‡,17,18‡						F		A-C	D-F
HYLC53	M	$DBH^{Cre};Rosa^{Ai32}$	05/12/16	09/02/16	MeV	53A-9‡,22‡,23‡,24,25‡,26						F		A-C	D-F
HYLC55	M	$DBH^{Cre};Rosa^{Ai32}$	06/06/16	09/16/16	MeV	55A-3‡,4‡,5‡,6,7,8‡,9‡, 10‡,11‡,12‡,13,14‡,19‡,20						F		A-C	D-F
HYLC56	M	$DBH^{Cre};Rosa^{Ai32}$	06/06/16	09/26/16	MeV	56A-5‡,6,7‡,8‡,12‡,13‡,14,15‡,16						F		A-C	D-F
Recordings of facial and whisker movement															
KSt159	F	$TrKC^{CreER};Rosa^{Ai32}$	12/07/16	10/20/17	SO; face; whisker	*N.A.*				E,F	D,E				
KSt160	M	$TrKC^{CreER};Rosa^{Ai32}$	12/07/16	10/14, 10/20/17	SO; whisker	*N.A.*				E,F					
KSt164	M	$TrKC^{CreER};Rosa^{Ai32}$	08/08/17	11/08/17	G; SO; face; whisker	*N.A.*				B-F	B-E				
KSt165	F	$TrKC^{CreER};Rosa^{Ai32}$	08/09/17	02/20/18	G; whisker	*N.A.*				B-F			D-F		
KSt166	M	$TrKC^{CreER};Rosa^{Ai32}$	08/09/17	02/09/18	G; whisker	*N.A.*				E,F					
KSt167	F	$TrKC^{CreER};Rosa^{Ai32}$	08/09/17	02/24/18	G; whisker	*N.A.*				E,F					
KSt168	F	$TrKC^{CreER};Rosa^{Ai32}$	08/09/17	05/04, 05/06/18	SO; micro; whisker	*N.A.*				E,F					
KSt169	F	$TrKC^{CreER};Rosa^{Ai32}$	08/09/17	05/05, 05/06/18	SO; micro; whisker	*N.A.*				B-F			A-C		
KSt170	M	$Ret^{CreER};Rosa^{Ai32}$	12/05/17	05/05, 05/06/18	SO; micro; whisker	*N.A.*				E,F					

Table 2. Meta-data for mice and their assignment to analyses in Chapter 3.

References

Abbs, J.H., and Gracco, V.L. (1984). Control of complex motor gestures: orofacial muscle responses to load perturbations of lip during speech. Journal of neurophysiology *51*, 705-723.

Abraira, V.E., and Ginty, D.D. (2013). The sensory neurons of touch. Neuron *79*, 618-639.

Aimonetti, J.M., Hospod, V., Roll, J.P., and Ribot-Ciscar, E. (2007). Cutaneous afferents provide a neuronal population vector that encodes the orientation of human ankle movements. The Journal of physiology *580*, 649-658.

Appenteng, K., Lund, J.P., and Seguin, J.J. (1982). Behavior of cutaneous mechanoreceptors recorded in mandibular division of Gasserian ganglion of the rabbit during movements of lower jaw. Journal of neurophysiology *47*, 151-166.

Arvidsson, J., and Rice, F.L. (1991). Central projections of primary sensory neurons innervating different parts of the vibrissae follicles and intervibrissal skin on the mystacial pad of the rat. The Journal of comparative neurology *309*, 1-16.

Bagdasarian, K., Szwed, M., Knutsen, P.M., Deutsch, D., Derdikman, D., Pietr, M., Simony, E., and Ahissar, E. (2013). Pre-neuronal morphological processing of object location by individual whiskers. Nature neuroscience *16*, 622-631.

Bai, L., Lehnert, B.P., Liu, J., Neubarth, N.L., Dickendesher, T.L., Nwe, P.H., Cassidy, C., Woodbury, C.J., and Ginty, D.D. (2015). Genetic Identification of an Expansive Mechanoreceptor Sensitive to Skin Stroking. Cell *163*, 1783-1795.

Bale, M.R., Campagner, D., Erskine, A., and Petersen, R.S. (2015). Microsecond-scale timing precision in rodent trigeminal primary afferents. The Journal of neuroscience : the official journal of the Society for Neuroscience *35*, 5935-5940.

Bergenheim, M., Ribot-Ciscar, E., and Roll, J.P. (2000). Proprioceptive population coding of two-dimensional limb movements in humans: I. Muscle spindle feedback during spatially oriented movements. Experimental brain research *134*, 301-310.

Bermejo, R., Szwed, M., Friedman, W., Ahissar, E., and Zeigler, H.P. (2004). One whisker whisking: unit recording during conditioned whisking in rats. Somatosensory & motor research *21*, 183-187.

Birdwell, J.A., Solomon, J.H., Thajchayapong, M., Taylor, M.A., Cheely, M., Towal, R.B., Conradt, J., and Hartmann, M.J. (2007). Biomechanical models for radial distance determination by the rat vibrissal system. Journal of neurophysiology *98*, 2439-2455.

Bosman, L.W., Houweling, A.R., Owens, C.B., Tanke, N., Shevchouk, O.T., Rahmati, N., Teunissen, W.H., Ju, C., Gong, W., Koekkoek, S.K*., et al.* (2011). Anatomical pathways involved in generating and sensing rhythmic whisker movements. Frontiers in integrative neuroscience *5*, 53.

Brecht, M., Preilowski, B., and Merzenich, M.M. (1997). Functional architecture of the mystacial vibrissae. Behavioural brain research *84*, 81-97.

Bush, N.E., Schroeder, C.L., Hobbs, J.A., Yang, A.E., Huet, L.A., Solla, S.A., and Hartmann, M.J. (2016). Decoupling kinematics and mechanics reveals coding properties of trigeminal ganglion neurons in the rat vibrissal system. eLife *5*.

Campagner, D., Evans, M.H., Bale, M.R., Erskine, A., and Petersen, R.S. (2016). Prediction of primary somatosensory neuron activity during active tactile exploration. eLife *5*.

Carvell, G.E., and Simons, D.J. (1990). Biometric analyses of vibrissal tactile discrimination in the rat. The Journal of neuroscience : the official journal of the Society for Neuroscience *10*, 2638-2648.

Chang, W., Kanda, H., Ikeda, R., Ling, J., DeBerry, J.J., and Gu, J.G. (2016). Merkel disc is a serotonergic synapse in the epidermis for transmitting tactile signals in mammals. Proceedings of the National Academy of Sciences of the United States of America *113*, E5491-5500.

Clack, N.G., O'Connor, D.H., Huber, D., Petreanu, L., Hires, A., Peron, S., Svoboda, K., and Myers, E.W. (2012). Automated tracking of whiskers in videos of head fixed rodents. PLoS computational biology *8*, e1002591.

Cohen, J.Y., Haesler, S., Vong, L., Lowell, B.B., and Uchida, N. (2012). Neuron-type-specific signals for reward and punishment in the ventral tegmental area. Nature *482*, 85-88.

Collins, D.F., Refshauge, K.M., Todd, G., and Gandevia, S.C. (2005). Cutaneous receptors contribute to kinesthesia at the index finger, elbow, and knee. Journal of neurophysiology *94*, 1699-1706.

Coste, B., Mathur, J., Schmidt, M., Earley, T.J., Ranade, S., Petrus, M.J., Dubin, A.E., and Patapoutian, A. (2010). Piezo1 and Piezo2 are essential components of distinct mechanically activated cation channels. Science *330*, 55-60.

Cover, T.M., and Thomas, J.A. (2006). Elements of information theory, 2nd edn (Hoboken, NJ: Wiley-Interscience).

Crapse, T.B., and Sommer, M.A. (2008). Corollary discharge across the animal kingdom. Nature reviews Neuroscience *9*, 587-600.

Crawley, M.J. (2002). Statistical computing : an introduction to data analysis using S-Plus (Chichester, West Sussex, England: Wiley).

Crochet, S., and Petersen, C.C. (2006). Correlating whisker behavior with membrane potential in barrel cortex of awake mice. Nature neuroscience *9*, 608-610.

Curtis, J.C., and Kleinfeld, D. (2009). Phase-to-rate transformations encode touch in cortical neurons of a scanning sensorimotor system. Nature neuroscience *12*, 492-501.

Danforth, C.H. (1925). Hair in its relation to questions of homology and phylogeny. Am J Anat *36*, 47-68.

Deschenes, M., Takatoh, J., Kurnikova, A., Moore, J.D., Demers, M., Elbaz, M., Furuta, T., Wang, F., and Kleinfeld, D. (2016). Inhibition, Not Excitation, Drives Rhythmic Whisking. Neuron *90*, 374-387.

Diamond, M.E., and Arabzadeh, E. (2013). Whisker sensory system - from receptor to decision. Progress in neurobiology *103*, 28-40.

Diamond, M.E., von Heimendahl, M., Knutsen, P.M., Kleinfeld, D., and Ahissar, E. (2008). 'Where' and 'what' in the whisker sensorimotor system. Nature reviews Neuroscience *9*, 601-612.

Dorfl, J. (1982). The musculature of the mystacial vibrissae of the white mouse. Journal of anatomy *135*, 147-154.

Dorfl, J. (1985). The innervation of the mystacial region of the white mouse: A topographical study. Journal of anatomy *142*, 173-184.

Dun, R.B., and Fraser, A.S. (1958). Selection for an invariant character; vibrissa number in the house mouse. Nature *181*, 1018-1019.

Ebara, S., Kumamoto, K., Matsuura, T., Mazurkiewicz, J.E., and Rice, F.L. (2002). Similarities and differences in the innervation of mystacial vibrissal follicle-sinus complexes in the rat and cat: a confocal microscopic study. The Journal of comparative neurology *449*, 103-119.

Edin, B. (2001). Cutaneous afferents provide information about knee joint movements in humans. The Journal of physiology *531*, 289-297.

Edin, B.B., and Abbs, J.H. (1991). Finger movement responses of cutaneous mechanoreceptors in the dorsal skin of the human hand. Journal of neurophysiology *65*, 657-670.

Fee, M.S., Mitra, P.P., and Kleinfeld, D. (1997). Central versus peripheral determinants of patterned spike activity in rat vibrissa cortex during whisking. Journal of neurophysiology *78*, 1144-1149.

Feldmeyer, D., Brecht, M., Helmchen, F., Petersen, C.C., Poulet, J.F., Staiger, J.F., Luhmann, H.J., and Schwarz, C. (2013). Barrel cortex function. Progress in neurobiology *103*, 3-27.

Fleming, M.S., and Luo, W. (2013). The anatomy, function, and development of mammalian Abeta low-threshold mechanoreceptors. Frontiers in biology *8*.

Fraser, G., Hartings, J.A., and Simons, D.J. (2006). Adaptation of trigeminal ganglion cells to periodic whisker deflections. Somatosensory & motor research *23*, 111-118.

Fundin, B.T., Arvidsson, J., and Rice, F.L. (1995). Innervation of nonmystacial vibrissae in the adult rat. The Journal of comparative neurology *357*, 501-512.

Fundin, B.T., Rice, F.L., Pfaller, K., and Arvidsson, J. (1994). The innervation of the mystacial pad in the adult rat studied by anterograde transport of HRP conjugates. Experimental brain research *99*, 233-246.

Goodmurphy, C.W., and Ovalle, W.K. (1999). Morphological study of two human facial muscles: orbicularis oculi and corrugator supercilii. Clin Anat *12*, 1-11.

Goodwin, G.M., and Luschei, E.S. (1975). Discharge of spindle afferents from jaw-closing muscles during chewing in alert monkeys. Journal of neurophysiology *38*, 560-571.

Goodwin, G.M., McCloskey, D.I., and Matthews, P.B. (1972). The contribution of muscle afferents to kinaesthesia shown by vibration induced illusions of movement and by the effects of paralysing joint afferents. Brain : a journal of neurology *95*, 705-748.

Haidarliu, S., Kleinfeld, D., Deschenes, M., and Ahissar, E. (2015). The Musculature That Drives Active Touch by Vibrissae and Nose in Mice. Anat Rec (Hoboken) *298*, 1347-1358.

Haidarliu, S., Simony, E., Golomb, D., and Ahissar, E. (2010). Muscle architecture in the mystacial pad of the rat. Anat Rec (Hoboken) *293*, 1192-1206.

Harrington, A.W., St Hillaire, C., Zweifel, L.S., Glebova, N.O., Philippidou, P., Halegoua, S., and Ginty, D.D. (2011). Recruitment of actin modifiers to TrkA endosomes governs retrograde NGF signaling and survival. Cell *146*, 421-434.

Hastie, T., Tibshirani, R., and Friedman, J.H. (2009). The elements of statistical learning : data mining, inference, and prediction, 2nd edn, 2nd edn (New York, NY: Springer).

Hill, D.N., Bermejo, R., Zeigler, H.P., and Kleinfeld, D. (2008). Biomechanics of the vibrissa motor plant in rat: rhythmic whisking consists of triphasic neuromuscular activity. The Journal of neuroscience : the official journal of the Society for Neuroscience *28*, 3438-3455.

Hill, D.N., Curtis, J.C., Moore, J.D., and Kleinfeld, D. (2011). Primary motor cortex reports efferent control of vibrissa motion on multiple timescales. Neuron *72*, 344-356.

Hires, S.A., Gutnisky, D.A., Yu, J., O'Connor, D.H., and Svoboda, K. (2015). Low-noise encoding of active touch by layer 4 in the somatosensory cortex. eLife *4*.

Hires, S.A., Schuyler, A., Sy, J., Huang, V., Wyche, I., Wang, X., and Golomb, D. (2016). Beyond cones: an improved model of whisker bending based on measured mechanics and tapering. Journal of neurophysiology *116*, 812-824.

Huber, D., Gutnisky, D.A., Peron, S., O'Connor, D.H., Wiegert, J.S., Tian, L., Oertner, T.G., Looger, L.L., and Svoboda, K. (2012). Multiple dynamic representations in the motor cortex during sensorimotor learning. Nature *484*, 473-478.

Hulliger, M., Nordh, E., Thelin, A.E., and Vallbo, A.B. (1979). The responses of afferent fibres from the glabrous skin of the hand during voluntary finger movements in man. The Journal of physiology *291*, 233-249.

Iggo, A., and Muir, A.R. (1969). The structure and function of a slowly adapting touch corpuscle in hairy skin. The Journal of physiology *200*, 763-796.

Ikeda, R., Cha, M., Ling, J., Jia, Z., Coyle, D., and Gu, J.G. (2014). Merkel cells transduce and encode tactile stimuli to drive Abeta-afferent impulses. Cell *157*, 664-675.

Ito, T., and Ostry, D.J. (2010). Somatosensory contribution to motor learning due to facial skin deformation. Journal of neurophysiology *104*, 1230-1238.

Jamali, M., Chacron, M.J., and Cullen, K.E. (2016). Self-motion evokes precise spike timing in the primate vestibular system. Nature communications *7*, 13229.

Johansson, R.S., Trulsson, M., Olsson, K.A., and Abbs, J.H. (1988). Mechanoreceptive afferent activity in the infraorbital nerve in man during speech and chewing movements. Experimental brain research *72*, 209-214.

Johnson, K.O., and Hsiao, S.S. (1992). Neural mechanisms of tactual form and texture perception. Annual review of neuroscience *15*, 227-250.

Johnson, K.O., Yoshioka, T., and Vega-Bermudez, F. (2000). Tactile functions of mechanoreceptive afferents innervating the hand. Journal of clinical neurophysiology : official publication of the American Electroencephalographic Society *17*, 539-558.

Jones, L.M., Lee, S., Trageser, J.C., Simons, D.J., and Keller, A. (2004). Precise temporal responses in whisker trigeminal neurons. Journal of neurophysiology *92*, 665-668.

Khatri, V., Bermejo, R., Brumberg, J.C., Keller, A., and Zeigler, H.P. (2009). Whisking in air: encoding of kinematics by trigeminal ganglion neurons in awake rats. Journal of neurophysiology *101*, 1836-1846.

Kleinfeld, D., and Deschenes, M. (2011). Neuronal basis for object location in the vibrissa scanning sensorimotor system. Neuron *72*, 455-468.

Kleinfeld, D., Moore, J.D., Wang, F., and Deschenes, M. (2014). The Brainstem Oscillator for Whisking and the Case for Breathing as the Master Clock for Orofacial Motor Actions. Cold Spring Harbor symposia on quantitative biology *79*, 29-39.

Knutsen, P.M., Biess, A., and Ahissar, E. (2008). Vibrissal kinematics in 3D: tight coupling of azimuth, elevation, and torsion across different whisking modes. Neuron *59*, 35-42.

Knutsen, P.M., Pietr, M., and Ahissar, E. (2006). Haptic object localization in the vibrissal system: behavior and performance. The Journal of neuroscience : the official journal of the Society for Neuroscience *26*, 8451-8464.

Kurnikova, A., Moore, J.D., Liao, S.M., Deschenes, M., and Kleinfeld, D. (2017). Coordination of Orofacial Motor Actions into Exploratory Behavior by Rat. Current biology : CB *27*, 688-696.

Lai, H.C., Seal, R.P., and Johnson, J.E. (2016). Making sense out of spinal cord somatosensory development. Development *143*, 3434-3448.

Leiser, S.C., and Moxon, K.A. (2007). Responses of trigeminal ganglion neurons during natural whisking behaviors in the awake rat. Neuron *53*, 117-133.

Lottem, E., and Azouz, R. (2011). A unifying framework underlying mechanotransduction in the somatosensory system. The Journal of neuroscience : the official journal of the Society for Neuroscience *31*, 8520-8532.

Luo, W., Enomoto, H., Rice, F.L., Milbrandt, J., and Ginty, D.D. (2009). Molecular identification of rapidly adapting mechanoreceptors and their developmental dependence on ret signaling. Neuron *64*, 841-856.

Madisen, L., Mao, T., Koch, H., Zhuo, J.M., Berenyi, A., Fujisawa, S., Hsu, Y.W., Garcia, A.J., 3rd, Gu, X., Zanella, S.*, et al.* (2012). A toolbox of Cre-dependent optogenetic transgenic mice for light-induced activation and silencing. Nature neuroscience *15*, 793-802.

Madisen, L., Zwingman, T.A., Sunkin, S.M., Oh, S.W., Zariwala, H.A., Gu, H., Ng, L.L., Palmiter, R.D., Hawrylycz, M.J., Jones, A.R.*, et al.* (2010). A robust and high-throughput Cre reporting and characterization system for the whole mouse brain. Nature neuroscience *13*, 133-140.

Maksimovic, S., Nakatani, M., Baba, Y., Nelson, A.M., Marshall, K.L., Wellnitz, S.A., Firozi, P., Woo, S.H., Ranade, S., Patapoutian, A., *et al.* (2014). Epidermal Merkel cells are mechanosensory cells that tune mammalian touch receptors. Nature *509*, 617-621.

Mameli, O., Caria, M.A., Biagi, F., Zedda, M., and Farina, V. (2017). Neurons within the trigeminal mesencephalic nucleus encode for the kinematic parameters of the whisker pad macrovibrissae. Physiological reports *5*.

Mameli, O., Stanzani, S., Mulliri, G., Pellitteri, R., Caria, M.A., Russo, A., and De Riu, P. (2010). Role of the trigeminal mesencephalic nucleus in rat whisker pad proprioception. Behavioral and brain functions : BBF *6*, 69.

Mameli, O., Stanzani, S., Russo, A., Pellitteri, R., Manca, P., De Riu, P.L., and Caria, M.A. (2014). Involvement of trigeminal mesencephalic nucleus in kinetic encoding of whisker movements. Brain research bulletin *102*, 37-45.

Maravall, M., and Diamond, M.E. (2014). Algorithms of whisker-mediated touch perception. Current opinion in neurobiology *25*, 176-186.

Masuda, Y., Morimoto, T., Hidaka, O., Kato, T., Matsuo, R., Inoue, T., Kobayashi, M., and Taylor, A. (1997). Modulation of jaw muscle spindle discharge during mastication in the rabbit. Journal of neurophysiology *77*, 2227-2231.

McElvain, L.E., Friedman, B., Karten, H.J., Svoboda, K., Wang, F., Deschênes, M., and Kleinfeld, D. (2018). Circuits in the Rodent Brainstem that Control Whisking in Concert with Other Orofacial Motor Actions. Neuroscience *368*, 152-170.

Mehta, S.B., Whitmer, D., Figueroa, R., Williams, B.A., and Kleinfeld, D. (2007). Active spatial perception in the vibrissa scanning sensorimotor system. PLoS biology *5*, e15.

Mitchinson, B., Gurney, K.N., Redgrave, P., Melhuish, C., Pipe, A.G., Pearson, M., Gilhespy, I., and Prescott, T.J. (2004). Empirically inspired simulated electro-mechanical model of the rat mystacial follicle-sinus complex. Proceedings Biological sciences *271*, 2509-2516.

Moore, J.D., Deschenes, M., Furuta, T., Huber, D., Smear, M.C., Demers, M., and Kleinfeld, D. (2013). Hierarchy of orofacial rhythms revealed through whisking and breathing. Nature *497*, 205-210.

Moore, J.D., Mercer Lindsay, N., Deschenes, M., and Kleinfeld, D. (2015). Vibrissa Self-Motion and Touch Are Reliably Encoded along the Same Somatosensory Pathway from Brainstem through Thalamus. PLoS biology *13*, e1002253.

Morimoto, T., Inoue, T., Masuda, Y., and Nagashima, T. (1989). Sensory components facilitating jaw-closing muscle activities in the rabbit. Experimental brain research *76*, 424-440.

O'Connor, D.H., Clack, N.G., Huber, D., Komiyama, T., Myers, E.W., and Svoboda, K. (2010). Vibrissa-based object localization in head-fixed mice. The Journal of neuroscience : the official journal of the Society for Neuroscience *30*, 1947-1967.

O'Connor, D.H., Hires, S.A., Guo, Z.V., Li, N., Yu, J., Sun, Q.Q., Huber, D., and Svoboda, K. (2013). Neural coding during active somatosensation revealed using illusory touch. Nature neuroscience *16*, 958-965.

Pais-Vieira, M., Lebedev, M.A., Wiest, M.C., and Nicolelis, M.A. (2013). Simultaneous top-down modulation of the primary somatosensory cortex and thalamic nuclei during active tactile discrimination. The Journal of neuroscience : the official journal of the Society for Neuroscience *33*, 4076-4093.

Pammer, L., O'Connor, D.H., Hires, S.A., Clack, N.G., Huber, D., Myers, E.W., and Svoboda, K. (2013). The mechanical variables underlying object localization along the axis of the whisker. The Journal of neuroscience : the official journal of the Society for Neuroscience *33*, 6726-6741.

Petreanu, L., Gutnisky, D.A., Huber, D., Xu, N.L., O'Connor, D.H., Tian, L., Looger, L., and Svoboda, K. (2012). Activity in motor-sensory projections reveals distributed coding in somatosensation. Nature *489*, 299-303.

Poulet, J.F., and Petersen, C.C. (2008). Internal brain state regulates membrane potential synchrony in barrel cortex of behaving mice. Nature *454*, 881-885.

Preibisch, S., Saalfeld, S., and Tomancak, P. (2009). Globally optimal stitching of tiled 3D microscopic image acquisitions. Bioinformatics *25*, 1463-1465.

Quist, B.W., Faruqi, R.A., and Hartmann, M.J. (2011). Variation in Young's modulus along the length of a rat vibrissa. Journal of biomechanics *44*, 2775-2781.

Quist, B.W., Seghete, V., Huet, L.A., Murphey, T.D., and Hartmann, M.J. (2014). Modeling forces and moments at the base of a rat vibrissa during noncontact whisking and whisking against an object. The Journal of neuroscience : the official journal of the Society for Neuroscience *34*, 9828-9844.

Ranade, S.S., Woo, S.H., Dubin, A.E., Moshourab, R.A., Wetzel, C., Petrus, M., Mathur, J., Begay, V., Coste, B., Mainquist, J*., et al.* (2014). Piezo2 is the major transducer of mechanical forces for touch sensation in mice. Nature *516*, 121-125.

Rice, F.L., Mance, A., and Munger, B.L. (1986). A comparative light microscopic analysis of the sensory innervation of the mystacial pad. I. Innervation of vibrissal follicle-sinus complexes. The Journal of comparative neurology *252*, 154-174.

Sakurai, K., Akiyama, M., Cai, B., Scott, A., Han, B.X., Takatoh, J., Sigrist, M., Arber, S., and Wang, F. (2013). The organization of submodality-specific touch afferent inputs in the vibrissa column. Cell reports *5*, 87-98.

Severson, K.S., Xu, D., Van de Loo, M., Bai, L., Ginty, D.D., and O'Connor, D.H. (2017). Active Touch and Self-Motion Encoding by Merkel Cell-Associated Afferents. Neuron *94*, 666-676 e669.

Severson, K.S., Xu, D., Yang, H., and O'Connor, D. (2018). What Can Facial Mechanoreceptors Tell the Mouse Brain About Whisking? BioRxiv.

Shoykhet, M., Doherty, D., and Simons, D.J. (2000). Coding of deflection velocity and amplitude by whisker primary afferent neurons: implications for higher level processing. Somatosensory & motor research *17*, 171-180.

Sofroniew, N.J., Cohen, J.D., Lee, A.K., and Svoboda, K. (2014). Natural whisker-guided behavior by head-fixed mice in tactile virtual reality. The Journal of neuroscience : the official journal of the Society for Neuroscience *34*, 9537-9550.

Solomon, J.H., and Hartmann, M.J. (2011). Radial distance determination in the rat vibrissal system and the effects of Weber's law. Philosophical transactions of the Royal Society of London Series B, Biological sciences *366*, 3049-3057.

Stal, P., Eriksson, P.O., Eriksson, A., and Thornell, L.E. (1987). Enzyme-histochemical differences in fibre-type between the human major and minor zygomatic and the first dorsal interosseus muscles. Archives of oral biology *32*, 833-841.

Stal, P., Eriksson, P.O., Eriksson, A., and Thornell, L.E. (1990). Enzyme-histochemical and morphological characteristics of muscle fibre types in the human buccinator and orbicularis oris. Archives of oral biology *35*, 449-458.

Stuttgen, M.C., Kullmann, S., and Schwarz, C. (2008). Responses of rat trigeminal ganglion neurons to longitudinal whisker stimulation. Journal of neurophysiology *100*, 1879-1884.

Suter, B.A., O'Connor, T., Iyer, V., Petreanu, L.T., Hooks, B.M., Kiritani, T., Svoboda, K., and Shepherd, G.M. (2010). Ephus: multipurpose data acquisition software for neuroscience experiments. Frontiers in neural circuits *4*, 100.

Szczot, M., Pogorzala, L.A., Solinski, H.J., Young, L., Yee, P., Le Pichon, C.E., Chesler, A.T., and Hoon, M.A. (2017). Cell-Type-Specific Splicing of Piezo2 Regulates Mechanotransduction. Cell reports *21*, 2760-2771.

Szwed, M., Bagdasarian, K., and Ahissar, E. (2003). Encoding of vibrissal active touch. Neuron *40*, 621-630.

Szwed, M., Bagdasarian, K., Blumenfeld, B., Barak, O., Derdikman, D., and Ahissar, E. (2006). Responses of trigeminal ganglion neurons to the radial distance of contact during active vibrissal touch. Journal of neurophysiology *95*, 791-802.

Takatoh, J., Prevosto, V., and Wang, F. (2018). Vibrissa sensory neurons: Linking distinct morphology to specific physiology and function. Neuroscience *368*, 109-114.

Taniguchi, H., He, M., Wu, P., Kim, S., Paik, R., Sugino, K., Kvitsiani, D., Fu, Y., Lu, J., Lin, Y.*, et al.* (2011). A resource of Cre driver lines for genetic targeting of GABAergic neurons in cerebral cortex. Neuron *71*, 995-1013.

Taylor, J.R. (1997). An introduction to error analysis : the study of uncertainties in physical measurements, 2nd edn (Sausalito, Calif.: University Science Books).

Tonomura, S., Ebara, S., Bagdasarian, K., Uta, D., Ahissar, E., Meir, I., Lampl, I., Kuroda, D., Furuta, T., Furue, H.*, et al.* (2015). Structure-function correlations of rat trigeminal primary neurons: Emphasis on club-like endings, a vibrissal mechanoreceptor. Proceedings of the Japan Academy Series B, Physical and biological sciences *91*, 560-576.

Trulsson, M., and Johansson, R.S. (2002). Orofacial mechanoreceptors in humans: encoding characteristics and responses during natural orofacial behaviors. Behavioural brain research *135*, 27-33.

Wallach, A., Bagdasarian, K., and Ahissar, E. (2016). On-going computation of whisking phase by mechanoreceptors. Nature neuroscience *19*, 487-493.

Welker, W.I., Johnson, J.I., Jr., and Pubols, B.H., Jr. (1964a). Some Morphological and Physiological Characteristics of the Somatic Sensory System in Raccoons. Am Zool *4*, 75-94.

Welker, W.I., Johnson, J.I., and Pubols, B.H. (1964b). Some Morphological and Physiological Characteristics of the Somatic Sensory System in Raccoons. Am Zool *4*, 75-94.

Whiteley, S.J., Knutsen, P.M., Matthews, D.W., and Kleinfeld, D. (2015). Deflection of a vibrissa leads to a gradient of strain across mechanoreceptors in a mystacial follicle. Journal of neurophysiology *114*, 138-145.

Williams, A.L., Gerling, G.J., Wellnitz, S.A., Bourdon, S.M., and Lumpkin, E.A. (2010). Skin relaxation predicts neural firing rate adaptation in SAI touch receptors. Conference proceedings : Annual International Conference of the IEEE Engineering in Medicine and Biology Society IEEE Engineering in Medicine and Biology Society Annual Conference *2010*, 6678-6681.

Wineski, L.E. (1983). Movements of the cranial vibrissae in the Golden hamster (Mesocricetus auratus). J Zool *200*, 261-280.

Wineski, L.E. (1985). Facial morphology and vibrissal movement in the golden hamster. Journal of morphology *183*, 199-217.

Woo, S.H., Lukacs, V., de Nooij, J.C., Zaytseva, D., Criddle, C.R., Francisco, A., Jessell, T.M., Wilkinson, K.A., and Patapoutian, A. (2015). Piezo2 is the principal mechanotransduction channel for proprioception. Nature neuroscience *18*, 1756-1762.

Woo, S.H., Ranade, S., Weyer, A.D., Dubin, A.E., Baba, Y., Qiu, Z., Petrus, M., Miyamoto, T., Reddy, K., Lumpkin, E.A.*, et al.* (2014). Piezo2 is required for Merkel-cell mechanotransduction. Nature *509*, 622-626.

Wood, S.N. (2006). Generalized additive models : an introduction with R (Boca Raton, FL: Chapman & Hall/CRC).

Woodbury, C.J., and Koerber, H.R. (2007). Central and peripheral anatomy of slowly adapting type I low-threshold mechanoreceptors innervating trunk skin of neonatal mice. The Journal of comparative neurology *505*, 547-561.

Yang, H., Kwon, S.E., Severson, K.S., and O'Connor, D.H. (2016). Origins of choice-related activity in mouse somatosensory cortex. Nature neuroscience *19*, 127-134.

Yu, C., Derdikman, D., Haidarliu, S., and Ahissar, E. (2006). Parallel thalamic pathways for whisking and touch signals in the rat. PLoS biology *4*, e124.

Yu, J., Gutnisky, D.A., Hires, S.A., and Svoboda, K. (2016). Layer 4 fast-spiking interneurons filter thalamocortical signals during active somatosensation. Nature neuroscience *19*, 1647-1657.

Zucker, E., and Welker, W.I. (1969). Coding of somatic sensory input by vibrissae neurons in the rat's trigeminal ganglion. Brain Res *12*, 138-156.

Curriculum Vitae

Kyle Scott Severson, B.S.

Born in Madison, Wisconsin, USA in 1989.

The Johns Hopkins University School of Medicine
The Solomon H. Snyder Department of Neuroscience
725 N Wolfe St, Room 1003
Baltimore, Maryland 21205

EDUCATION

2012-2018	**Ph.D., Neuroscience** **The Johns Hopkins University**, Baltimore, MD Advisor: Prof. Daniel H. O'Connor Committee members: Profs. Xinzhong Dong, Jeremy Nathans, and Jeremiah Cohen
2008-2012	**B.S., Biochemistry, Biology** **University of Wisconsin**, Madison, WI

PUBLICATIONS

2018	**Severson KS**, Xu D, Yang H, O'Connor DH. What can facial mechanoreceptors tell the mouse brain about whisking? *BioRxiv.* doi: https://doi.org/10.1101/402883.
2017	**Severson KS***, Xu D*, Van de Loo M, Bai L, Ginty DD, O'Connor DH. Active touch and self-motion encoding by Merkel cell-associated afferents. *Neuron* 94, 666–676.
2016	Yang H*, Kwon SE*, **Severson KS**, O'Connor DH. Origins of choice-related activity in mouse somatosensory cortex. *Nat Neurosci.* 19(1): 127-34.

2015 Wang Y, Marling SJ, Beaver EF, **Severson KS**, Deluca HF. UV light selectively inhibits spinal cord inflammation and demyelination in experimental autoimmune encephalo-myelitis. *Arch Biochem Biophys*. 567: 75-82.

2013 Wang Y, Marling SJ, McKnight SM, Danielson AL, **Severson KS**, Deluca HF. Suppression of experimental autoimmune encephalomyelitis by 300-315nm ultraviolet light. *Arch Biochem Biophys*. 536(1): 81-6.

2012 Wang Y, Marling SJ, Zhu JG, **Severson KS**, DeLuca HF. Development of experimental autoimmune encephalomyelitis (EAE) in mice requires vitamin D and the vitamin D receptor. *Proc Natl Acad Sci U S A*. 109(22): 8501-4.

2010 Becklund BR, **Severson KS**, Vang SV, DeLuca HF. Ultraviolet radiation suppresses experimental autoimmune encephalomyelitis independent of vitamin D production. *Proc Natl Acad of Sci USA*. 107(14): 6418-23.

*Co-first authors

OTHER PUBLICATIONS

2017 **Severson KS**, O'Connor DH. Active Sensing: The rat's nose dances in step with whiskers, head, and breath. *Curr Biol.* 27(5): R183-R185.

PRESENTATIONS

2017 **Severson KS**. Primary afferent encoding of whisker self-motion. Oral presentation at: Department of Neuroscience Annual Retreat. Cambridge, MD.

2016 **Severson KS**, Xu D, Bai L, Ginty DD, O'Connor DH. Touch and self-motion encoding by Merkel-cell associated primary afferents. Poster presented at: Neuroscience 2016. San Diego, CA.

2015	**Severson KS**, Xu D, O'Connor DH. Stimulus feature coding by trigeminal ganglion neurons during natural whisking against an object. Poster presented at: Neuroscience 2015. Chicago, IL.

TEACHING EXPERIENCE

2014-2016	**Undergraduate mentor**, Johns Hopkins University
2013	**Teaching assistant**, Neuroscience and Cognition course

HONORS AND AWARDS

2018	**Bae Gyo Jung Young Investigators' Day Award**, Johns Hopkins University

OTHER TRAINING

2011-2012	**Undergraduate researcher**, Center for Sleep and Consciousness, University of Wisconsin, Madison, WI Research advisor: Prof. Chiara Cirelli
2008-2011	**Undergraduate researcher**, Department of Biochemistry, University of Wisconsin, Madison, WI Research advisor: Prof. Hector F. DeLuca

PROFESSIONAL MEMBERSHIPS

2015-present	**Society for Neuroscience**